

**Novel Reactor and System Design/Simulation for  
Carbon-based Energy Conversions**

**Zhongkai Zhao**

**A Dissertation Submitted in Partial Fulfillment of the Requirements  
for the Degree of Doctor of Philosophy in Engineering**

**GRADUATE SCHOOL OF SCIENCE AND TECHNOLOGY  
HIROSAKI UNIVERSITY**

**2021**

## ABSTRACT

Energy is an important foundation of human survival and society development, and the world's energy demand is still increasing year by year. Nowadays, carbon-based energies are still the major section in the world's energy consumption. For a long time in the future, carbon-based energies cannot be replaced completely. Thermochemical conversion is considered as the best way to convert carbon-based energies into various convenient energies since it realizes the possibility of removal of harmful impurities such as tar, sulfur and so on. In general, the products are usually cooled down before purification because the purification technologies at high temperature condition are not yet mature. However, a large amount of exergy is always lost during cooling and purification processes. Therefore, the process design with complete tar conversion and highly efficient exergy recuperation is the key issue in the carbon-based energy utilization system. This dissertation, on the one hand, considers novel design and optimization of gasifier to give a guidance in application of the multi-stage gasification system. On the other hand, advanced small-scale biomass power generation system and highly efficient dry reforming of methane system were designed and analyzed. It includes 7 chapters.

Firstly, a Eulerian-Eulerian model incorporating the kinetic theory of granular flow is adopted to simulate the gas-solids flow behaviors in a dense downer below a conventional downer, which could be used for the further pyrolysis of coal and/or decomposition of tar on the generated char before the char and tar are completely separated in a triple-bed combined circulating fluidized bed (TBCFB) system. The high solids holdup in the dense downer can enhance the heat transfer to completely pyrolyze

coal as well as decompose the heavy tar, avoiding the negative impact of pyrolysis products on the char gasification. In order to obtain the optimal structural parameters and operating conditions and evaluate the performance of this dense downer, the influences of downer diameter, cone angle and solids mass flux on the hydrodynamic behaviors are investigated in details. The results demonstrate that the solids holdup in the dense downer can be increased, however, the maximum solids holdup is limited to approximately 0.4 owing to the ultimate carrying capacity. Moreover, it is found that there is a peak solids holdup in the annular region near the wall whereas many particles concentrate at the center in the high-density operation states. Meanwhile, the unique solids radial distribution could be caused by the radial movement of particles. Moreover, the intense collisions and turbulence caused by high velocity could inhibit agglomerates, which should be benefit for the heat transfer. It is expected that these results could offer a guidance for the design of such a dense downer for effective improvement of the efficiency of the pyrolyzer.

Secondly, a small-scale highly-efficient combined heat and power generation system with a separated-type biomass gasification process combining the energy/exergy recuperation is proposed for the first time. The spatial subdivision of the processes for the biomass pyrolysis, char combustion, tar reforming and catalyst regeneration is adopted by using a separated-type biomass gasifier design to realize the optimization of each conversion step and improve the whole system performance. To obtain the maximum power generation efficiency, the energy flow and exergy flow in the system are analyzed in details and the operating condition of the gasification system is optimized. The results demonstrate that the relatively low temperature as well as low steam/carbon ratio in the tar reformer should be conducive to the improvement of

energy and exergy efficiencies. In the optimum operation condition, the biomass input of 548.86 kW (higher heating value) could generate 263.65 kW of electrical power with the total energy and exergy efficiencies of 37.9% and 43.2%, respectively, in which 153.44 kW of energy could be recuperated back to the gasification process by air and steam with 136.56 kW of energy obtained from gas turbine exhaust to enhance the whole power generation efficiency. It is expected to provide a new design concept for the development of high-efficient small-scale biomass gasification system for the combined heat and power generation.

Thirdly, the hydrodynamics of a small-scale separated-type biomass gasification system are investigated by the simulation based on cold model to assess two kind of gas seal structures between BFB and riser. In the case of only siphon structure, due to the low solids mass flux, the intended pressure balance between BFB and riser cannot be maintained, causing that air of riser breaks through the moving bed layer and flows into BFB sometimes. The flow behavior of BFB and riser presents a special periodicity. Compared with only a siphon structure, the combination of siphon configuration and seal tank shows better gas seal performance. Because of the resistance of configuration of partition and sand particles accumulated at the left side of seal tank, the injected air can be well directed to the riser.

Finally, a novel separated-type autothermal dry reforming of methane (S-ATDRM) system is proposed and simulated, in which the methane dry reforming combined with methane partial oxidation is performed in a circulating fluidized bed with exergy recuperation to eliminate the negative effect of the products of CH<sub>4</sub> partial oxidation on the DRM reaction and further improve the CO<sub>2</sub> conversion efficiency. The results demonstrate that this S-ATDRM system can achieve an exergy efficiency of 87.2%, and

about 1055.7 kW of exergy can be recuperated from the crude syngas cooling process and reused for the pre-heating of feedstocks of CO<sub>2</sub>, O<sub>2</sub> and CH<sub>4</sub>. It is found that the largest exergy destruction in this system occurs in the partial oxidation reactor, which accounts for about 63.1% of the total exergy loss. Comparing with the conventional ATDRM system, although the exergy of S-ATDRM system is decreased by approximately 0.1%, the CO<sub>2</sub> conversion is substantially increased by about 11.3%.

## ACKNOWLEDGEMENTS

First of all, I would like to express my sincere gratitude and appreciation to Professor Guoqing Guan, Professor Abuliti Abudula and Associate Professor Akihiro Yoshida, for giving me an opportunity to work towards PhD in their laboratory and for their invaluable comments, suggestions and precious advices to solve all complicated problems occurred during my research. Moreover, they also took care of my living in Japan and gave me a great experience in many things during my staying in Japan.

My special thanks go to all members in our research group and Institute of Regional Institute and Graduate School of Science and Technology at Hirosaki University for their helps and supports for my research and everything. In addition, I would like to thank everybody, my friends for their care and friendship.

I also would like to acknowledge the scholarship from China Scholarship Council (CSC) and research assistant fund for PhD course student from Hirosaki University.

Finally, I would like to thank my dear parents, all my family and my friends in China, for their love, support, encouragement, and understanding during my PhD study.

Thank you all,

Zhongkai Zhao

# TABLE OF CONTENTS

ABSTRACT .....	i
ACKNOWLEDGEMENTS .....	v
TABLE OF CONTENTS.....	vi
LIST of TABLES.....	x
LIST of FIGURES.....	xii
CHAPTER 1: Introduction.....	1
1.1 Prospective carbon-based energies.....	1
1.2 Coal/biomass gasification.....	6
1.2.1 Mechanism of coal/biomass gasification.....	6
1.2.2 Gasifying agents .....	8
1.2.3 Types of gasifier .....	10
1.2.4 Exergy recuperation in gasification system.....	13
1.2.5 Purification of gasification products .....	15
1.3 Advanced gasification applications in power generation .....	25
1.3.1 Industrial-scale gasification power generation systems .....	25
1.3.2 Small-scale biomass gasification power generation systems .....	31
1.4 Dry reforming of methane .....	33
1.4.1 Description of dry reforming of methane.....	33
1.4.2 Catalysts of dry reforming of methane.....	34
1.4.3 Reactors of dry reforming of methane.....	35
1.4.4 Autothermal dry reforming of methane.....	38
1.5 Motivation and objectives .....	38

1.6 Organization and outline of this dissertation .....	40
References .....	41
CHAPTER 2: Simulation Software and Models .....	53
2.1 Computational fluid dynamics simulation.....	53
2.2 Process simulation .....	54
CHAPTER 3: Numerical Simulation of Hydrodynamic Behaviors in A Gas-Solids Dense Downer Reactor.....	57
3.1 Introduction .....	57
3.2 Simulation methods .....	60
3.2.1 Mathematical model .....	60
3.2.2 Verification of model correctness .....	63
3.2.3 Simulation conditions .....	65
3.3 Results and discussion .....	68
3.3.1 Effect of the diameter of dense downer.....	68
3.3.2 Effect of the cone angle .....	74
3.3.3 Effect of solids mass flux .....	77
3.4. Conclusions .....	81
Nomenclature.....	82
References .....	85
CHAPTER 4: A Biomass-Based Small-Scale Power Generation System with Energy/Exergy Recuperation.....	90
4.1 Introduction .....	90
4.2 System process and simulation methods .....	95
4.2.1 The proposed separated-type biomass gasification process .....	96



4.2.2	Solid oxide fuel cells .....	100
4.2.3	Gas turbine.....	102
4.2.4	Simulation methods .....	102
4.3	Energy and Exergy Analyses .....	103
4.3.1	Energy analysis.....	104
4.3.2	Exergy analysis.....	106
4.4	Results and discussion .....	108
4.4.1	Sensitivity analysis of the gasification process. ....	108
4.4.2	Energy and Exergy analyses for the total power generation system ..	114
4.4.3	Exergy analysis of total power generation system .....	117
4.5	Conclusions .....	135
	Nomenclature.....	136
	References .....	138
CHAPTER 5: Flow Behaviors in A Small-Scale Biomass Gasifier.....		145
5.1	Introduction .....	145
5.2	Simulation methods .....	149
5.2.1	Mathematical model .....	149
5.2.2	Simulation conditions .....	152
5.2.3	Grid independence analysis.....	154
5.3	Results and discussion.....	155
5.4	Conclusions .....	158
	Nomenclature.....	159
	References .....	161
CHAPTER 6: A Separated-Type Autothermal CH <sub>4</sub> Dry Reforming System with Exergy		

Recuperation.....	165
6.1 Introduction .....	165
6.2 System description and simulation method.....	168
6.3 Exergy analysis.....	173
6.4 Results and discussion.....	176
6.4.1 Sensitivity analysis of S-ATDRM system. ....	176
6.4.2 Comparison of this S-ATDRM system with the conventional ATDRM system.....	180
6.5 Conclusions .....	185
Nomenclature.....	186
References .....	187
CHAPTER 7: Conclusions and Future Perspectives.....	192
7.1 Conclusions .....	192
7.2 Future perspectives.....	195
LIST of PUBLICATIONS .....	197
CURRICULUM VITAE.....	202

## LIST of TABLES

Table 1-1 Advantages and disadvantages of various gasifying agents.....	9
Table 1-2 Comparison of the mostly used absorption methods for sulfur removal [60].....	21
Table 1-3 Advantages and disadvantages of various catalysts of tar reforming.....	24
Table 2-1 Block icons of Aspen Plus used in this study.....	55
Table 3-1 Simulation parameters.....	65
Table 4-1 Main characteristics of feedstock and pyrolysis products (based on the literatures [25]).....	98
Table 4-2 Reactions in the separated-type biomass gasification process.....	99
Table 4-3 Essential simulation assumptions and models in the proposed small-scale high-efficient power generation process.....	102
Table 4-4 Empirical coefficients of specific heat capacity at the constant pressure [35].....	105
Table 4-5 Specific chemical exergies of the components at the dead state [40].....	107
Table 4-6 Detail energy results of every stream.....	120
Table 4-7 Mass flows, temperatures and pressures of every stream.....	125
Table 4-8 Detail exergy results of every stream.....	127
Table 4-9 The calculated exergy efficiencies and exergy destructions of different units.....	131
Table 4-10 Comparison of the performance of the present novel small-scale CHP system with other reported biomass gasification CHP systems.....	133

Table 5-1 Simulation parameters.....	153
Table 6-1 Reactions in the separated-type ATDRM system process.....	171
Table 6-2 Essential simulation assumptions and models in the proposed separated-type ATDRM system process.....	172
Table 6-3 Empirical coefficients of specific heat capacity at the constant pressure [33].....	175
Table 6-4 Specific chemical exergies of the components at the dead state [30, 34].....	175

## LIST of FIGURES

Fig. 1-1 Schematic of coal/biomass gasification process and syngas applications.....	3
Fig. 1-2 Configuration diagrams of downdraft (left) and updraft gasifiers (right) (modified from Ref. [40]).....	11
Fig. 1-3 Diagrams of fluidized bed (left) and circulating fluidized bed (right).....	12
Fig. 1-4 Diagram of typical entrained flow gasifier (left) and two-stage entrained flow gasifier (right).....	13
Fig. 1-5 Schematics of various syngas cooling designs.....	15
Fig. 1-6 Typical CO <sub>2</sub> absorption and capture process (modified from Ref. [51]).....	17
Fig. 1-7 Schematic of CaO-looping gasifier (modified from Ref. [52]).....	18
Fig. 1-8 Schematic of chemical looping gasifier with Fe-based oxygen carrier (modified from Ref. [54]).....	19
Fig. 1-9 Conventional IGCC system.....	26
Fig. 1-10 Simplified diagrams for IGCC systems with CO <sub>2</sub> capture.....	28
Fig. 1-11 Basic structures of A-IGCC and A-IGFC systems.....	30
Fig. 1-12 The high-density triple-bed combined circulating fluidized bed gasifier (reprinted with permission from Ref. [12]).....	30
Fig. 1-13 The small-scale separated-type biomass gasification system proposed by Guan et al. [75].....	32
Fig. 1-14 Schematic diagrams of (a) fixed bed reformer, (b) fluidized bed reformer, (c) plasma reformer, and (d) membrane reformer (modified from Ref. [81]).....	36
Fig. 3-1 Schematic diagram of apparatus.....	60
Fig. 3-2 Comparisons between model predictions and available data from Guan <i>et al.</i>	

[38].....	64
Fig. 3-3 Geometry and dimensions of dense downer in the simulation.....	66
Fig. 3-4 Grid sensitivity analysis.....	67
Fig. 3-5 Average solids holdup and residence time with different $D$ .....	68
Fig. 3-6 Radial distributions with different $D$ at the outlet of dense downer: (a) solids velocity and (b) gas velocity.....	70
Fig. 3-7 Radial distributions of solids holdups at the outlets of dense downers with different $D$ .....	71
Fig. 3-8 Solids radial velocity distributions at the inlets of dense downers with different $D$ .....	71
Fig. 3-9 Axial distributions of solids radial velocity along the dense downers with different $D$ .....	72
Fig. 3-10 Contours of solids holdup distributions of dense downer.....	73
Fig. 3-11 Effect of cone angle on: (a) average solids holdup, (b) average solids velocity and (c) average gas velocity.....	75
Fig. 3-12 Radial distributions of solids holdups at outlets of dense downers with different cone angles.....	76
Fig. 3-13 Axial distributions of solids radial velocities at outlets of dense downers with different cone angles.....	77
Fig. 3-14 Effects of $G_s$ on average solids holdup.....	78
Fig. 3-15 Radial distribution of solids holdup with different $G_s$ at outlet of dense downer.....	79
Fig. 3-16 Axial distribution with different $G_s$ : (a) slip velocity, and (b) solids holdup.....	80

Fig. 4-1 Schematic of the proposed biomass-based power generation system with energy/exergy recuperation.....	94
Fig. 4-2 Detailed flowsheet of the system in Aspen Plus software.....	96
Fig. 4-3 Schematic diagram of the proposed separated-type biomass gasification system.....	97
Fig. 4-4 Effect of operating condition of steam reforming on the produced syngas composition: a) $T_{SR}$ , b) S/C.....	110
Fig. 4-5 Effect of operating condition on $H_2/CO$ molar ratio of produced syngas.....	111
Fig. 4-6 Effect of operating condition on LHV of the produced syngas.....	112
Fig. 4-7 Effect of operating condition on energy efficiency of the gasification process.....	113
Fig. 4-8 Effect of operating condition on exergy efficiency of the gasification system.....	114
Fig. 4-9 Sankey diagram of the total power generation system. (Energy flows are expressed in kW.).....	116
Fig. 4-10 Grassmann diagram of the total power generation system. (Exergy flows are expressed in kW.).....	119
Fig. 5-1 Schematic diagram of apparatus.....	147
Fig. 5-2 Geometry and dimensions of gasification system with different gas seal types in the simulation.....	149
Fig. 5-3 Grid independence analysis.....	154
Fig. 5-4 Solids holdup distribution and airflow velocity vector of BFB with only siphon structure (case <sub>1</sub> ) .....	156
Fig. 5-5 The visual representations of periodic flow behaviors of BFB.....	157

Fig. 5-6 Solids holdup distribution and airflow velocity vector of BFB with only siphon structure (case <sub>2</sub> ).....	158
Fig. 6-1 Schematic of the proposed separated-type ATDRM system with circulating fluidized bed and exergy recuperation.....	169
Fig. 6-2 Schematic of the conventional ATDRM system.....	170
Fig. 6-3 Effect of operating condition in dry reforming: a) CO <sub>2</sub> conversion, b) CH <sub>4</sub> conversion.....	178
Fig. 6-4 Effect of operating condition in dry reforming on the exergy efficiency of total system.....	179
Fig. 6-5 Detailed flowsheet of the system in Aspen Plus software: a) the separated-type ATDRM system, b) the conventional ATDRM system.....	181
Fig. 6-6 Products of the separated-type ATDRM system and the conventional ATDRM system.....	182
Fig. 6-7 Grassmann diagram: a) the separated-type ATDRM system, b) the conventional ATDRM system. (Exergy flows are expressed in kW.).....	183



# CHAPTER 1: Introduction

## 1.1 Prospective carbon-based energies

Energy is an important foundation of human survival and society development. Nowadays, carbon-based energies account for about 85% of the world's energy supplement according to the report of International Energy Agency (IEA) [1]. The carbon-based energies play a crucial role in power generation plant, chemical industry, community heating and so on. Although governments and organizations around the world are trying to develop new energy to replace the carbon-based energies, for a long time in the future, carbon-based energies are still the major fuel in global energy consumption due to the limitation of economic and technological development and energy resource distribution.

In the past several hundred years, a large number of high-quality carbon-based energies have been exploited and utilized. With the large consumption and reduction of high-quality carbon-based energies, the low-quality carbon-based energies, such as low-rank coals, have gotten widespread attention from various fields of research and engineering [2]. Low-rank coals accounts for approximately half of all global coal deposits and are widely distributed in the world [2-4]. Since the low-rank coals characterized by low heating value and high moisture and ash contents, they are not suitable to be directly used as fuel in industrial process [4]. Moreover, the combustion of low-rank coals without pretreatment can result in serious emissions of nitrogen species ( $\text{NH}_3$ ,  $\text{HCN}$ ,  $\text{NO}_x$ , etc.), sulfur species ( $\text{H}_2\text{S}$ ,  $\text{SO}_x$ , etc.) and particulate matters

(PM), which have severely damaged the health of humanity. Consequently, development and application of clean coal technology (CCT), which is designed to reduce emission of pollutants associated with coal combustion and gasification, have turned to be the key issue of utilization of low-rank coals in the future.

As one of clean low-rank coals utilization technologies, gasification is a well-established way to convert coal into syngas (mainly consists of hydrogen ( $H_2$ ), carbon monoxide (CO), methane ( $CH_4$ ) and carbon dioxide ( $CO_2$ )). As shown in Fig. 1-1, coal gasification can bypass the conventional coal combustion process and provide a good chance of removing sulfur, nitrogen compounds and particulates [5]. Due to the advantages of gasification, the low-rank coals can be widely used for electrical power generation or for chemical processes such as synthesis of liquid fuels (Fischer-Tropsch synthesis), ammonia and methanol production [6-9]. In power generation, compared to the Rankine cycle based steam turbine, the Brayton cycle based gas turbine with rapid response shows a better performance [10]. Moreover, the high temperature exhaust produced from gas turbine can be fed into a heat recovery steam generator (HRSG) to generate steam that will work in steam turbine for additional power generation [11]. Therefore, considering environmental protection and high-efficiency power generation, integrated coal gasification combined cycle (IGCC) technique has been a very popular alternative to conventional fossil-fuel power plants. In recent years, many novel designs such as integrated coal gasification fuel cell combined cycle power generating technology (IGFC), advanced IGCC system (A-IGCC), advanced IGFC system (A-IGFC), and super IGFC system have been proposed to further increase power generation efficiency [12].

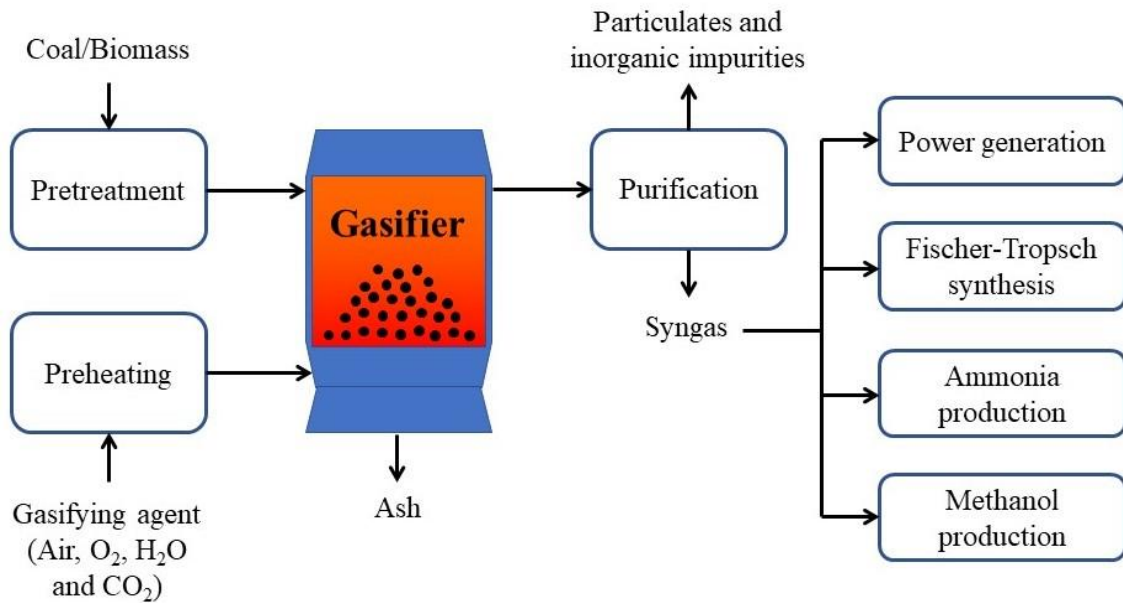


**Fig. 1-1** Schematic of coal/biomass gasification process and syngas applications.

With the development of coal gasification, the gasification technology in biomass utilization has also attracted increasingly extensive attention and shows a booming prospect [13]. Biomass can be defined as one of the renewable and sustainable carbon-based energy resources which can provide stable electricity and heat [14]. Especially, the carbon dioxide produced from the utilization of biomass can be captured by afforestation, preventing the carbon dioxide from exacerbating global warming [15]. Therefore, as environmentally friendly natural energy, the biomass is becoming more and more important and generally considered to replace the traditional fossil fuels to generate electricity in the future [16]. Nevertheless, the net biomass to electricity efficiencies of conventional combustion-type power plants are still low, which only range from 20% to 30% (based on lower heating value (LHV)) [17]. In addition, the high specific investment cost and emissions of acid gases such as nitrogen oxides (NO<sub>x</sub>) and sulfur oxides (SO<sub>x</sub>) are also essential to be solved [18]. Thus, the biomass

gasification based combined heat and power (CHP) systems with high thermal efficiency and excellent pollutants removing capability have become the main stream in the application of biomass energy [19]. Same as coal gasification, the syngas produced from biomass gasification also consists of  $H_2$ ,  $CO$ ,  $CH_4$   $CO_2$ , indicating that the biomass gasification also can be used to provide raw materials for Fischer-Tropsch synthesis, ammonia and methanol production.

Among the carbon-based energy resources, in addition to low-rank coals and biomass, methane also shows a booming prospect. From 1990 to 2018, the consumption of natural gas increases by about 70.6% [1]. In recent years, due to the discovery of abundant shale gas reserves and the development of fracturing technology, methane has been one of preferred energy resources [20]. Generally, methane can also be considered as renewable energy resources. Under anaerobic conditions, methane can be generated by fermentation of various substrates, such as biomass, food waste, living stock manure, and wastewater [20, 21]. Moreover, the abundant methane resources can be used not only as a fuel, but also to deal with the climate change caused by  $CO_2$  [22].

As we all know, the utilization of carbon-based energies results in the global warming, which deteriorates climate now. According to the report of Intergovernmental Panel on Climate Change (IPCC), average temperature of earth has already reached  $1^\circ C$  above the pre-industrial level, resulting in warmer ocean, more acidic and less productive [23].  $CO_2$  is the second greenhouse gases (GHG) after water vapor and contributes to about 26% of greenhouse effect [24]. From International Energy Agency (IEA), the total global  $CO_2$  emission from energy source was approximately 33.5 Gt per year [25]. Due to the unstable and uneven temporal and spatial distribution of water

vapor, water vapor is generally not taken into consideration when planning measures to refrain the greenhouse effect. Therefore, the application of CO<sub>2</sub> capture and storage (CCS) becomes key to mitigate the global warming. Nowadays, about 40 Mt of CO<sub>2</sub> is captured from power and industrial facilities each year [26]. However, the conventional technology of CO<sub>2</sub> capture and storage in subsurface formations greatly increases industrial costs, causing it to lose economic competitiveness [27]. National Energy Technology Laboratory (NETL) has reported that integrating of CO<sub>2</sub> capture unit (monoethanolamine as the solvent of absorption) into coal combustion power plant would cost approximately 80 US dollar per ton CO<sub>2</sub> and decrease about 10.6% of total efficiency [28]. In order to release some of the pressure on the CCS cost, it is urgent to develop effective technology of CO<sub>2</sub> utilization.

Currently, dry reforming of methane (DRM) has been researched and applied extensively, since much CO<sub>2</sub> can be consumed and converted to high value-added syngas during DRM process. And the produced syngas has a ratio of H<sub>2</sub> to CO close to 1, which is suitable for Fischer-Tropsch (F-T) synthesis of long chain hydrocarbons or can be directly used as a fuel for solid oxide fuel cells [29-31]. Moreover, compared with other CH<sub>4</sub> reforming processes, DRM technology can decrease about 20% of operating cost [29].

As indicated above, the abundant and cheap low-rank coals, biomass and methane have great advantages to alleviate the energy shortage in the future. How to improve the efficiency and avoid the emission of pollutions becomes the key for utilization of the carbon-based energies. In this chapter, coal/biomass gasification technologies and applications and methane dry reforming technologies are introduced and discussed.

## 1.2 Coal/biomass gasification

### 1.2.1 Mechanism of coal/biomass gasification

Coal/biomass gasification is a thermochemical conversion process, in which carbonaceous substances are converted into syngas in the presence of a gasifying agent (air, steam, oxygen, CO<sub>2</sub> or a mixture of them) at high temperatures. The coal/biomass gasification processes usually undergo 4 steps, i.e., drying, pyrolysis, oxidation and reduction as follow:

**Drying** Generally, the coal/biomass is dried before entering into gasifier since moisture has a great negative effect on the overall gasification thermodynamics [32]. Especially, some low rank coal or fresh biomass has a high inherent moisture content ranging from 45 to 66 wt% (wet basis) [33].

**Pyrolysis** This step usually occurs at the temperatures greater than about 320 °C [34]. In the pyrolysis, some chemical bonds in coal/biomass are broken and the coal/biomass will be decomposed into volatiles with various molecular weights and char. After cooling to ambient temperature, some volatiles composed of heavy organic and inorganic molecules will become a black, viscous and corrosive liquid, which is called as tar. While, the solid residue mainly containing carbon is called char.

**Oxidation** At this step, volatiles and some chars are oxidized or partial oxidized with oxygen (O<sub>2</sub>) to CO, CO<sub>2</sub> and water vapor (H<sub>2</sub>O). The oxidation reactions are exothermic and can provide heat for the endothermic reduction reactions.

**Reduction** This step occurs at temperatures in the range 800-1200 °C, in which the

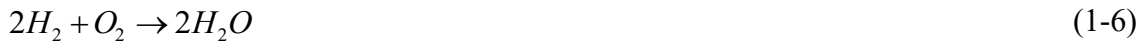
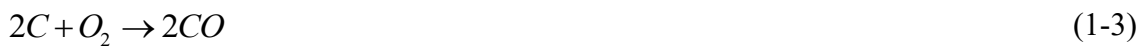
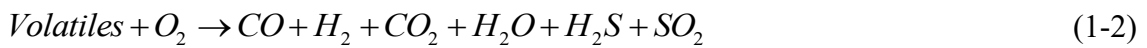
char reacts with gasifying agents to produce the syngas. Moreover, the steam reforming and water-gas shift (WGS) reaction also occur at this step.

The main reactions occurring during coal/biomass gasification are summarized as follows [13, 34, 35]:

Pyrolysis reaction:



Oxidation reactions:



Char gasification reactions:



Water-gas shift reaction:



Methane reforming reaction:



Ash slagging:



### 1.2.2 Gasifying agents

From these gasification reactions (Eqs. (1-1)-(1-15)), it should be noted that the gasifying agent has a significant effect on the compositions of produced syngas. The usually used gasifying agents include air, O<sub>2</sub>, steam (H<sub>2</sub>O), CO<sub>2</sub> and their mixtures. **Table 1-1** shows a summary of the advantages and disadvantages of various gasifying agents.

The coal/biomass gasification with air is a mature technology and has been widely used. The abundance of air greatly reduces the cost of coal gasification. In the case of using air as the gasifying agent, partial oxidation occurs to provide heat for the endothermic reactions. Moreover, air gasification has been proved to give a higher net thermal efficiency than oxygen gasification [36]. However, a serious dilution of the produced syngas by the nitrogen in the air is inevitable, resulting in a relatively lower heating value. Meanwhile, the large air-blown volume can lower the temperature in the gasifier, which causes negative effect on the gasification rate [37].

Similar as air gasification, the oxygen gasification is also an autothermal process. Due to no dilution effect of nitrogen, the produced syngas has a higher heating value. After the syngas is combusted as a fuel, the main components of the exhaust are CO<sub>2</sub>



and H<sub>2</sub>O, which can reduce the difficulty of CO<sub>2</sub> capture and storage (CCS) (Prabu and Jayanti 2012). On the other hand, in the case of using pure oxygen, the generation of oxygen from air needs an air separation unit (ASU), which will significantly increase the cost due to the high electrical consumption [38].

**Table 1-1** Advantages and disadvantages of various gasifying agents.

<b>Gasifying agent</b>	<b>Advantages</b>	<b>Disadvantages</b>
Air	Abundant and low-cost	Nitrogen dilution of syngas
	Autothermal process	Decreasing temperature in the
	High net thermal efficiency	gasifier
Oxygen	Autothermal process	High-cost
	Favor of CO <sub>2</sub> capture and storage	
	High heating value	
Steam	Low operating temperature	Heating demand
	High heating value	
	High H <sub>2</sub> content	
Carbon dioxide	Reducing the cost of CO <sub>2</sub> capture and storage	Low reaction rate
		Heating demand
	High heating value	

Steam gasification of coal/biomass can produce gaseous fuel with relatively higher heat value and hydrogen content, which is suitable for high-efficient fuel cells and hydrogen engines. Compared to the oxygen-blown gasification process at high

temperatures (1100-1500 °C), the steam gasification is usually carried out at lower temperatures (700-900 °C) [18]. However, since the steam gasification is an endothermic process, how to realize a stable heat supplement has to be considered. To solve the problem of heat input, the steam is often used as a gasification agent together with oxygen or air. Furthermore, the steam gasification also can get heat from combustion via heat carrier particles in a circulating fluidized bed (CFB).

The carbon dioxide gasification can partly reuse the captured CO<sub>2</sub> and reduce the cost of CCS to some extent. Similar as the steam gasification, the CO<sub>2</sub> gasification is also an endothermic process. However, the operating temperature of CO<sub>2</sub> gasification is usually higher than 900 °C due to slower reaction rate than gasification with other gasifying agents [39].

### **1.2.3 Types of gasifier**

In the coal/biomass gasification industry, the gasifiers commonly used include the fixed bed reactor/moving bed reactor, the fluidized bed reactor and the entrained flow reactor. The main difference between them is the distribution and interaction of gas-solid phases in the gasifier.

#### **1.2.3.1 Fixed bed gasifier**

The fixed bed gasifier is also named as the moving bed gasifier because of the slow motion of the solid phase in the continuous operation. According to the flow configuration of solid-gas phases, the fixed bed gasifier is divided into two types: co-current downdraft gasifier and counter-current updraft gasifier (Fig. 1-2). The biggest advantage of the fixed bed gasifier is its simple structure and easy operation. Herein, the

counter-current updraft configuration is more flexible than downdraft gasifier [40]. However, their temperature distributions are always nonuniform and tar is easily generated, which increases the difficult of syngas purification. Especially, compared with the downdraft gasifier, more tar in the syngas could be produced from the updraft gasifier [41].

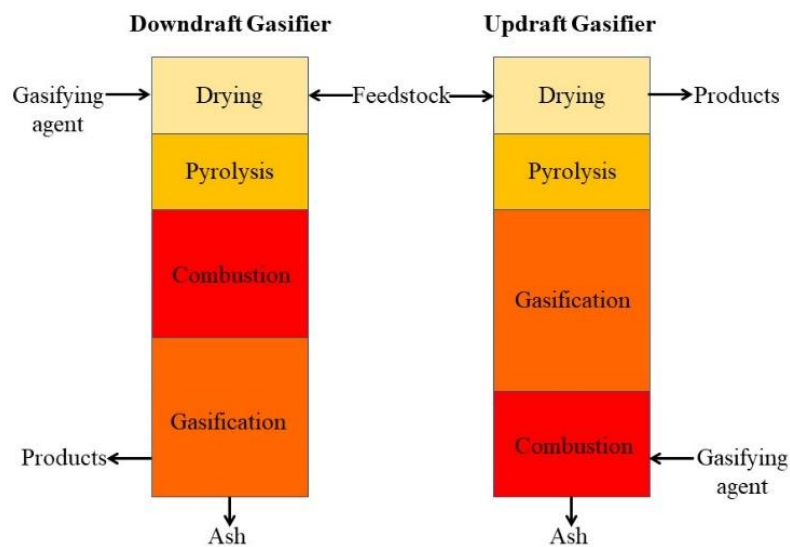


**Fig. 1-2** Configuration diagrams of downdraft (left) and updraft gasifiers (right)  
(modified from Ref. [40])

### 1.2.3.2 Fluidized bed gasifier

The fluidized bed gasifier (illustrated in Fig. 1-3) has been extensively applied in the industrial process of coal gasification [42]. In the fluidized bed reactor, the coal/biomass or catalyst particles can show a flow state like liquid under the action of gas, which can enhance the interaction between solids and gas and refrain the formation of hot spots [43]. However, many fly-ashes and tar could enter the purification units

along with the generated syngas, leading to the increase of purification cost and risk of tube blockage [44]. Moreover, in the recent years, circulating fluidized bed systems have been received much interest as the high-efficiency coal/biomass gasification processes for the production of syngas [18]. The circulating fluidized bed (CFB) system usually consists of two or three fluidized beds and other auxiliary equipment. In the CFB system, the endothermic gasification process can be separated from combustion process by the circulation of heat carrier particles. In addition, the spatial subdivision prevents the produced syngas from mixing with combustion exhaust to avoid the syngas being diluted.

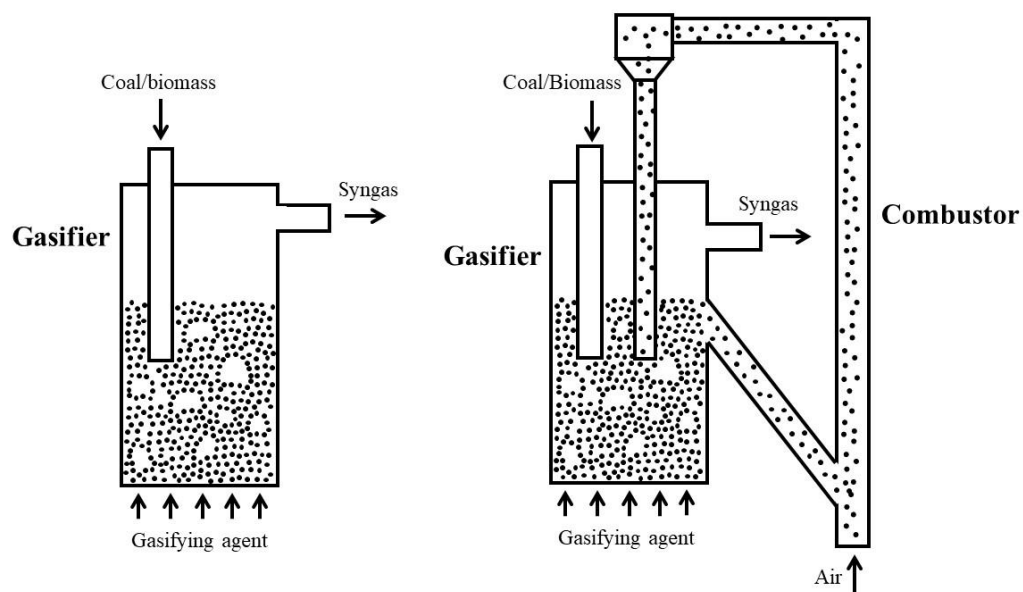


**Fig. 1-3** Diagrams of fluidized bed (left) and circulating fluidized bed (right)

### 1.2.3.3 Entrained flow gasifier

The entrained flow gasifiers (illustrated in Fig. 1-4) are the most extensively used industrial-scale gasifiers due to their flexibility and low tar content in the products [40].

Generally, the coal/biomass particles are injected with gasifying agents at a high speed, and then the coal/biomass particles in entrained flow gasifiers show a suspension mode. The unique gas-solid flow can achieve a rapid gasification process, however, coal/biomass is required to be pulverized [45]. The entrained flow gasifiers usually operate at a temperature range of 1200-1600 °C and a pressure range of 2-8 MPa, resulting in a high carbon conversion [40]. However, the corrosion and erosion of high temperature molten slag on the refractory linings are serious, which limits the choice of refractory materials [46].

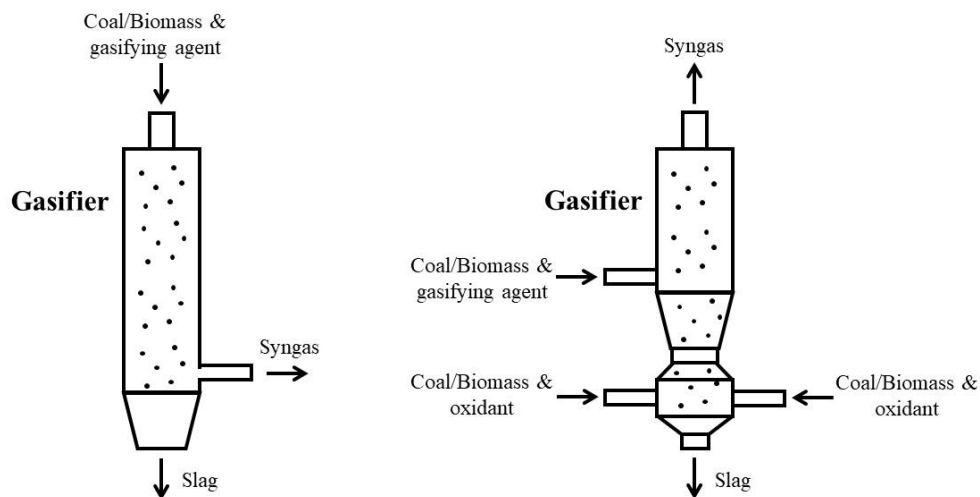


**Fig. 1-4** Diagram of typical entrained flow gasifier (left) and two-stage entrained flow gasifier (right)

#### 1.2.4 Exergy recuperation in gasification system

The exergy is usually used to express the maximum useful work from a thermal system. In other words, the exergy based on the second law of thermodynamics can be

used for the effective evaluation the energy conversion quality in a system. Generally, the high-temperature crude syngas produced from the gasifier cannot be used as a gas fuel directly due to the existence of many impurities and toxic substances such as sulfur oxides, nitrogen oxides and particulate matters in it. It is noted that the syngas purification unit is indispensable in a plant. Since the technologies of the high-temperature purification are still immature, conventional commercial gasification plants typically employ high temperature heat exchangers to cool down the hot syn-gas before the purification [47]. However, during the process of cooling, a large amount of heat (physical exergy) is released, leading to a great exergy loss and an obvious decrease of whole thermal efficiency in the gasification system [48]. Therefore, avoiding the exergy loss as much as possible and reusing them are very critical to a thermal system.

In order to recuperate the physical exergy, some heat-exchange equipment has to be set. However, the conventional heat exchangers cannot be used to cool down the crude syngas directly, since the entrained particles in the crude syngas are molten or sticky. In addition, the temperatures are too high for the heat exchangers [49]. Thus, a quench unit has to be added between the gasifier and the convective syngas cooler (heat exchanger) to rapidly cool down the syngas temperature to 700-900 °C. In the design of Fig. 1-5(a), partial cold syngas is recycled to mix with the high-temperature crude syngas for realizing the cooling-down to approximately 900 °C after the particle filter [50]. Then the syngas can be cooled by heat exchangers, and much high and/or intermediate pressure steams are produced simultaneously. The second design is the use of a radiant syngas quench (Fig. 1-5(b)). In the radiant quench, the crude syngas is firstly cooled to about 700 °C, thereby producing a high-pressure steam based on the

radiation heat transfer. The crude syngas is further cooled down in convective syngas coolers after removing the solidified slag [49]. Generally, the exergy in produced steam can be converted to electricity energy, or recycled to gasifier for the steam gasification process to achieve the maximum of thermal efficiency.

Another design (Fig. 1-5(c)) is named as the direct water quench or partial water quench, whereby the hot raw syngas is cooled down to about 200 °C by a direct water injection. Although the generated steam cannot be recovered due to mixing with syngas, additional steam is not required prior to the water-gas shift reaction, which can save much exergy and is beneficial to the H<sub>2</sub> generation as well as the CO<sub>2</sub> capture [47]. Furthermore, the water quench can remove out the solidified slag as well as water soluble components such as NH<sub>3</sub> and HCl [49].

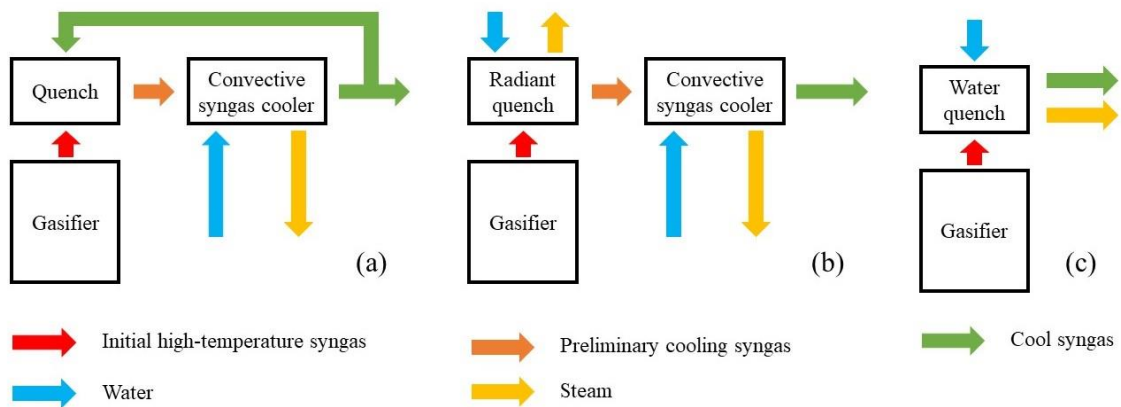


**Fig. 1-5** Schematics of various syngas cooling designs.

## 1.2.5 Purification of gasification products

### 1.2.5.1 Carbon dioxide removal

CO<sub>2</sub> emission from coal/biomass is larger than other fossil fuels due to its high

carbon content. The serious greenhouse effect has forced modern coal/biomass chemical industry to develop CCS technologies for the realization of zero-CO<sub>2</sub>-emission. Simultaneously, the high cost of CCS makes commercial industries have to consider the recovery and utilization of CO<sub>2</sub>.

Various processes have been tried to separate the CO<sub>2</sub> from syngas: physical absorption, chemical absorption, solids adsorption, membranes separation, and cryo-genic separation. However, membranes separation and cryogenic separation are not yet suitable for large coal/biomass gasification plants due to high cost and high electricity consumption [28]. In addition, the industrial scale membranes for the CO<sub>2</sub> separation do not yet exist and are being developed [51]. Therefore, the physical or chemical absorption is still the best choice in a coal/biomass gasification plant.

A typical CO<sub>2</sub> absorption process is shown in Fig. 1-6. Firstly, the crude syngas to be treated is injected into the bottom of the absorption column after cooled down and compressed. In the absorption column, the crude syngas is washed to obtain pure syngas by solvents such as methanol (MeOH), Dimethyl Ether of Polyethylene Glycol (DEPG), N-Methyl-2-Pyrrolidone (NMP), Propylene Carbonate (PC) and so on. Then, the rich solvent enters desorption column to release CO<sub>2</sub> and regenerates to the lean solvent, which can be reused in the absorption column. Although the conventional physical and chemical absorptions of CO<sub>2</sub> have been well-established and widely utilized in coal/biomass gasification plants, there are also some disadvantages: (1) large energy penalty for regeneration; (2) high equipment corrosion rate; (3) negative environmental impact of solvent emission.



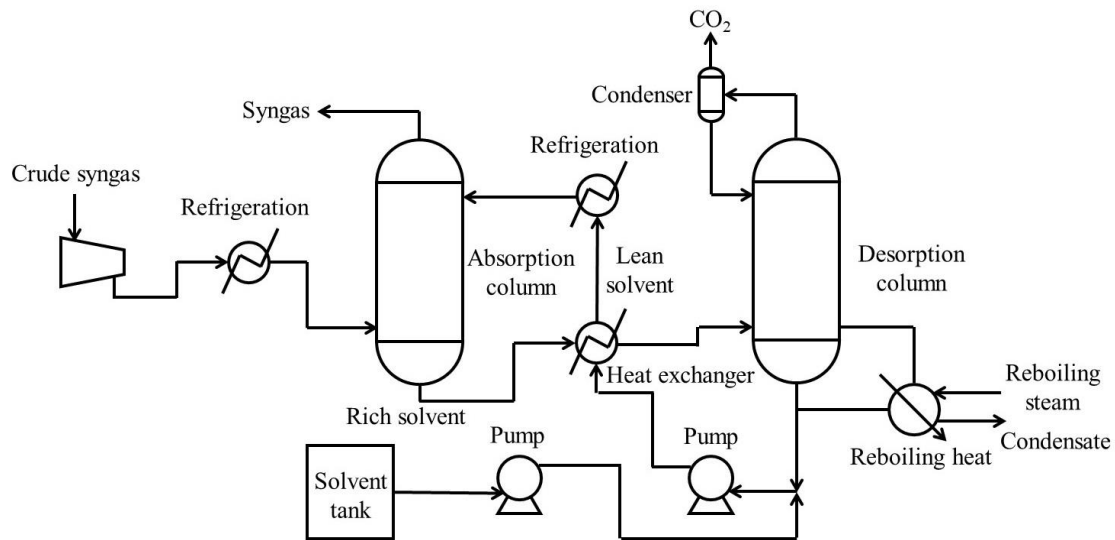


**Fig. 1-6** Typical CO<sub>2</sub> absorption and capture process (modified from Ref. [51]).

Recently, a CO<sub>2</sub> capture method by in situ chemical looping coal/biomass gasification named HyPr-RING (Hydrogen Production by Reaction-Integrated Novel Gasification) attracts much attention. Chemical looping technology is highly flexible since it allows the spatial subdivision of different processes. Fig. 1-7 illustrates a chemical looping coal/biomass gasification system based on CaO-CaCO<sub>3</sub> (CaO-looping gasifier) [52, 53]. In the underlying concept of the HyPr-RING process, a dual-bed circulating fluidized bed (DFCFB) reactor including a gasifier and a regenerator is applied. For the whole process, the feedstocks supplied are the coal/biomass, steam and CaO, and a syngas with high H<sub>2</sub> content and pure CO<sub>2</sub> can be obtained. At first, coal/biomass and steam are converted to H<sub>2</sub> and CO<sub>2</sub> in the gasifier. The generated CO<sub>2</sub> is absorbed by CaO or Ca(OH)<sub>2</sub> in the form CaCO<sub>3</sub>, and an amount of heat is released for the coal/biomass steam gasification at the same time. Then, the CaCO<sub>3</sub> enters into regenerator to be calcined to CaO with release of the CO<sub>2</sub>. In the gasifier, the water-gas shift reaction is shifted toward H<sub>2</sub> due to CO<sub>2</sub> absorption, resulting in an 80-90% H<sub>2</sub>

content in syn-gas. Moreover, CaO can be used for sulfur removal in this unique process. It is expected that the cold gas efficiency reaches more than 75% with a near zero emission of the sulfur content in the produced syngas, and a pure CO<sub>2</sub> capture.

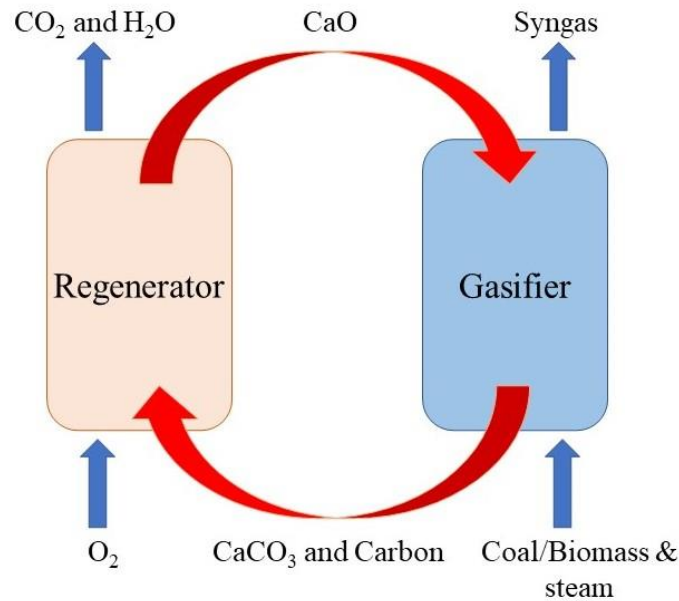


**Fig. 1-7** Schematic of CaO-looping gasifier (modified from Ref. [52]).

There is another chemical looping technology based on iron and its oxides. As shown in Fig. 1-8, the chemical looping gasifier (CLG) system with Fe-based oxygen carrier has three major coupling parts, i.e., air reactor, fuel reactor and steam reactor. At first, the Fe-based oxygen carriers are reduced by the coal/biomass with the generation of CO<sub>2</sub> and H<sub>2</sub>O in the fuel reactor. Then, the reduced Fe and FeO enter the steam reactor and are partially oxidized by steam to produce H<sub>2</sub>. Thereafter, the partially oxidized oxygen carriers (Fe<sub>3</sub>O<sub>4</sub>) flow into the air reactor and completely oxidized by air. Finally, the completely oxidized oxygen carriers (Fe<sub>2</sub>O<sub>3</sub>) are circulated back to the fuel reactor for the next gasification cycle. Obviously, compared with CaO-looping

gasifier, the CLG with Fe-based oxygen carrier can not only separate CO<sub>2</sub>, but also use air directly, avoiding the high electricity consumption of air separation unit.

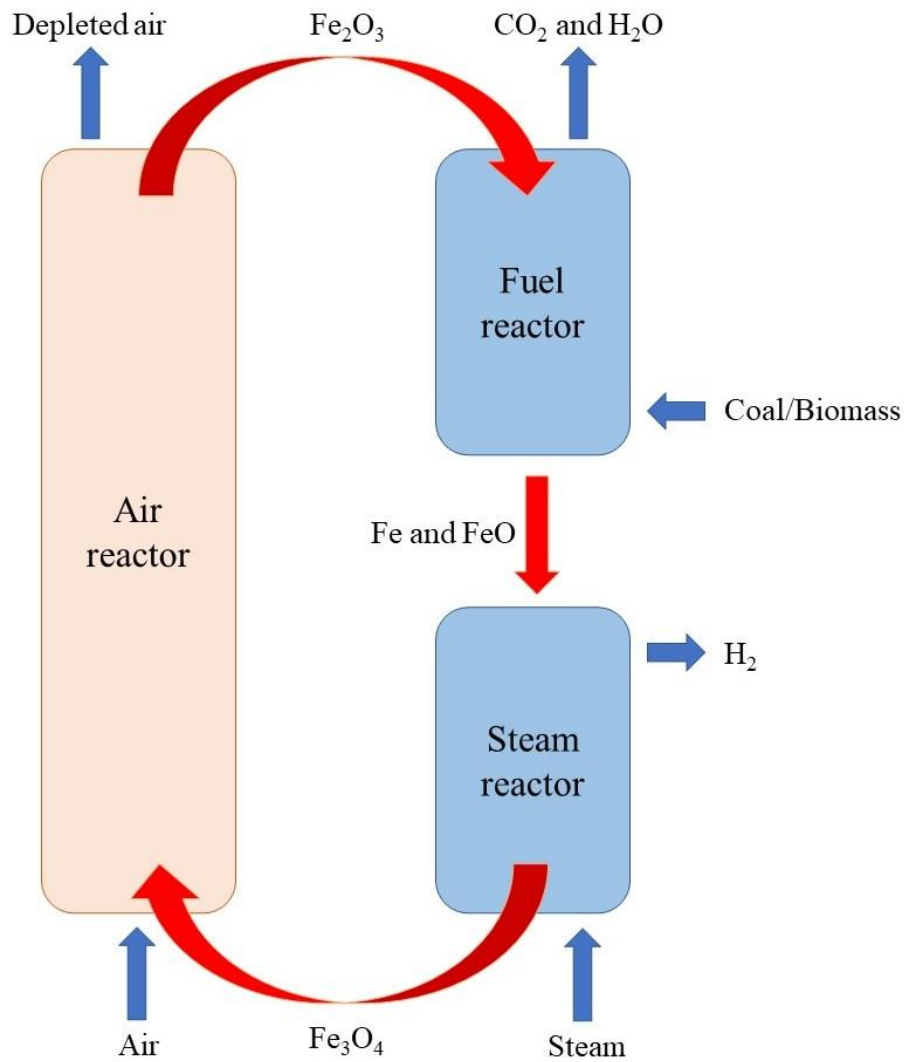


**Fig. 1-8** Schematic of chemical looping gasifier with Fe-based oxygen carrier (modified from Ref. [54]).

### 1.2.5.2 Sulfur removal

Sulfur is one of the most abundant impurities of coal and the sulfurous gases normally ranges from 0.1 to 1.6% (vol.%) in the produced syngas [55]. In biomass

gasification, the organic sulfur is considered to be the main source of H<sub>2</sub>S released [56]. As the sulfurous gases can cause acidification of soil and freshwater by forming acid rain, many countries and regions have issued environmental legislations to limit sulfur emissions [56]. Therefore, desulfurization is one of the most important cleaning processes in coal/biomass gasification. In addition, desulfurization must meet the requirements of downstream processes to avoid deactivating catalysts or corroding equipment [55].

During gasification processes, sulfur in the coal/biomass is usually converted to hydrogen sulfide (H<sub>2</sub>S), carbonyl sulfide (COS), carbon disulfide (CS<sub>2</sub>) and so on. Among these sulfurous gases, H<sub>2</sub>S is the most dominant compound [57]. The sulfurous gases in syngas can be removed by two modes: wet and dry cleaning processes. Since 1970s, wet cleaning technology has been successfully commercialized and is widely regarded as a conventional approach for desulfurization from syngas [58]. In these technologies, alkanolamines, alkaline salts or aqueous ammonia and organic solvents with high affinity for sulfurous gases are generally used as chemical or physical solvents, respectively [59]. **Table 1-2** shows a comparison of the mostly used absorption methods for sulfur removal [60]. It can be seen that these solvents can not only almost completely remove sulfur in syngas, but also absorb COS and CO<sub>2</sub>. Moreover, they are not disposable and can be regenerated by heating and depressurizing. In addition to wet cleaning processes, activated carbon or metal impregnated activated carbon are also widely used as absorbents to remove sulfurous gases due to their high specific surface area and porous structure [60]. This method is called dry cleaning technology of sulfurous gases. However, the H<sub>2</sub>S adsorption capacity commonly decreases after the

regeneration of spent activated carbon since some sulfur species are strongly bound with activated sites [61].

**Table 1-2 Comparison of the mostly used absorption methods for sulfur removal [60].**

<b>Solvent</b>	<b>Mechanism</b>	<b>Removal efficiency (%)</b>	<b>Typical process conditions</b>	<b>Exit gas quality</b>	<b>Remarks</b>
MDEA <sup>a</sup>	Chemical	H <sub>2</sub> S: 98-99 CO <sub>2</sub> : ≤30	T: 30-35 °C P: ≤2.94 MPa	H <sub>2</sub> S: 10-20 ppmv	Lowest capital cost Moderate operating temperature
Selexol <sup>b</sup>	Physical	H <sub>2</sub> S: 99 CO <sub>2</sub> : variable	T: -7--4 °C P: 6.87 MPa	H <sub>2</sub> S: <30 ppmv	Limited physical COS absorption Higher cost than MDEA High-efficiency for systems with sulfur recovery and tail gas treating
Rectisol <sup>c</sup>	Physical	H <sub>2</sub> S: 99.5-99.9 CO <sub>2</sub> : 98.5	T: 35-60 °C P: 8.04 MPa	H <sub>2</sub> S: <0.1 ppmv CO <sub>2</sub> : down to few	Highest cost Highest removal of H <sub>2</sub> S Ability to remove COS High selectivity for H <sub>2</sub> S over CO <sub>2</sub>

<sup>a</sup>MDEA: Methyl-diethanol amine    <sup>b</sup>Selexol: Selexol process (dimethyl ether of polyethylene glycol)

<sup>c</sup>Rectisol: Rectisol process (refrigerated methanol)

In addition to the conventional technologies of sulfur removal described previously, desulfurization approaches under high operating temperature ( $>300\text{ }^{\circ}\text{C}$ ) are being popular since the amount exergy lost in process of syngas cooling down could be avoided. The most common sorbents employed in desulfurization are metal oxides since metal oxide can be converted to its corresponding metal sulfide [58]. The desulfurization reactions of the general form can be written as:



Herein, the M refers to a divalent metal. Considering both thermodynamic feasibility and melting point, oxides of 11 metals (Fe, Zn, Mo, Mn, V, Ca, Sr, Ba, Co, Cu, W) have been proven as sulfur sorbents, which can achieve 95% or greater desulfurization at a temperature range of 400-1200  $^{\circ}\text{C}$  [55].

### 1.2.5.3 Nitrogen removal

Nitrogen mainly exists in the forms of ammonia ( $\text{NH}_3$ ) and small amount of hydrogen cyanide (HCN) in the crude syngas. Due to the high solubility of  $\text{NH}_3$  and HCN in water, the conventional approach of scrubbing based on water is widely applied in the removal of nitrogenous gases [58]. In a spray column, the conventional approach can significantly reduce the  $\text{NH}_3$  concentration with a removal efficiency more than 99% [62]. Moreover, water scrubbing is usually used to remove nitrogen species and tar simultaneously, but the wastewater treatment becomes more complicated [63].

In addition to water, various dilute acid solutions also can be used as wet scrubbing absorbents since they make  $\text{NH}_3$  protonate to ammonium ( $\text{NH}_4^+$ ). Generally, the acid absorbents for nitrogen contaminant removal can absorb acid gases such as  $\text{H}_2\text{S}$ ,

resulting in the increase of absorbent acidity over time. The released hydrogen ions ( $H^+$ ) further enhance the ability of  $NH_3$  removal. However, the corrosiveness of acid absorbents can cause irreversible damage to metal equipment, limiting its utilization in chemical processing of coal/biomass [58]. Moreover, for the syngas with high  $NH_3$  content (more than 500 vppm), the efficiency of nitrogen contaminant removal is lower than 50% [64].

#### **1.2.5.4 Tar removal**

Similar as carbon dioxide, sulfur, nitrogen removals, the conventional approach of tar removal is also carried out by wet scrubbing with water-based or oil-based absorbents. Water is one of the common absorbents for scrubbing tars from syngas due to its low cost [65]. Water scrubbing can remove the light and oxygenated compounds in tar easily due to their inherent polarity, but the removal efficiency of heavy compounds is low [66]. Moreover, treatment of wastewater is always inefficient and difficult [58]. Compared with water scrubbing, the oil scrubbing shows a more excellent performance and the tar removal efficiency can reach as high as 99% [66]. The oil-based absorbents can be regenerated by hot gas stripping and generate a concentrated tar stream to release partial cost pressure [66]. However, based on the economical consideration, an oil scrubbing system makes the process more complex and simultaneously, the oil-based absorbents are commonly not cheap, resulting in that such a method is only attractive for the large-scale plants [58].

In addition to wet scrubbing approach, the tar removal by catalytic reforming have been concerned recently. The major reforming agents are steam and  $CO_2$ , and the reactions can be described as follows [67, 68]:



The tar reforming needs a high temperature operating condition due to the endothermic nature and high activation energy. If the reforming reaction is carried out in the presence of a suitable catalyst, a highly efficient conversion can be achieved at a relatively low temperature (650-900 °C). However, the catalyst deactivation caused by coking on the active sites make catalysts be not well adopted in the industrial-scale equipment [69]. Therefore, the researches of tar reforming mainly focus on development of highly active and stable catalysts. **Table 1-3** summaries the advantages and disadvantages of various catalysts.

**Table 1-3.** Advantages and disadvantages of various catalysts of tar reforming.

<b>Catalyst</b>	<b>Advantages</b>	<b>Disadvantages</b>
Natural catalysts	Abundant and low-cost Ability to use directly	Low catalytic activity Low carbon deposition resistance
Zeolite catalysts	High porosity High specific surface area High tar conversion under high acidity	Easy to deactivate under high acidity
Alkali catalysts	Good catalytic activity	Evaporation and difficult recovery
Transition metal-	High catalytic activity	Low carbon deposition



based catalysts	Ability to enhance WGS reaction	resistance Low sintering resistance
Noble metal-based catalysts	High catalytic activity Stable in long time	Expensive

### 1.3 Advanced gasification applications in power generation

As described above, coal/biomass gasification is a technology to convert raw coal/biomass into a syngas with higher chemical heating value. The clean syngas can be efficiently used for electricity generation. Nowadays, coal/biomass gasification is regarded as the heart of the clean coal/biomass utilization technology and integrated in various advanced power generation systems such as IGCC, IGFC.

#### 1.3.1 Industrial-scale gasification power generation systems

##### 1.3.1.1 IGCC/IGFC system

As illustrated in Fig. 1-9, a conventional IGCC system mainly includes a gasifier, a syngas quench, a syngas purification process, a heat recovery steam generator (HRSG) and an electrical power generation process with a gas turbine and a steam turbine. In this IGCC system, the coal/biomass is converted into syngas at first, and then the impurities are removed from the syngas before using in a gas turbine to produce electricity. The high-temperature exhaust from the gas turbine is used to heat the water for HRSG, and the steam from the HRSG and quench produces additional electricity in a steam turbine. This design results in a higher power generation efficiency and lower

emissions of  $\text{SO}_x$ ,  $\text{NO}_x$  and particulate matters. Based on the design of IGCC, the fuel cells such as solid oxide fuel cells (SOFCs) can be also introduced into the electrical power generation process, named as IGFC, in which the purified syngas is utilized in fuel cell at first, and then, the depleted fuel gas from fuel cell is combusted to promote gas turbine. According to the report of Siefert and Lister [70], the exergy destruction of combination of fuel cell and gas turbine is much lower than that of single gas turbine, resulting in a higher thermal efficiency in IGFC system. On the other hand, the fuel cells can convert the chemical energy in the fuel directly into electricity, and the efficiency is not subjected to the limitation of Carnot efficiency [71].

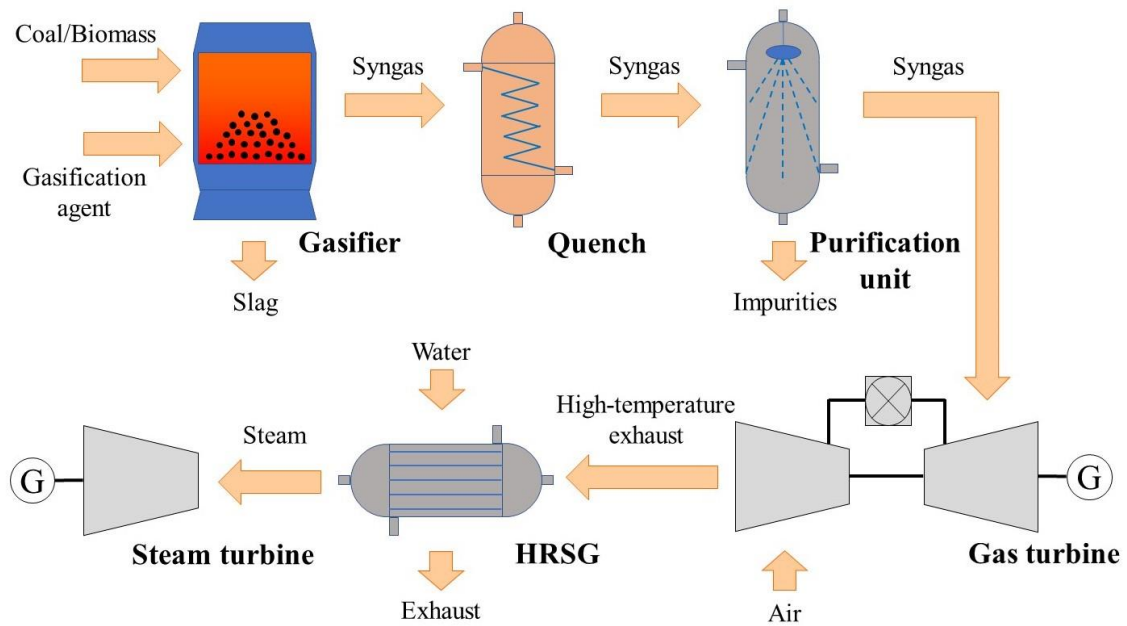


**Fig. 1-9** Conventional IGCC system.

Under the pressure of environment deterioration, the  $\text{CO}_2$  capture or recovery unit is widely coupled in IGCC/IGFC system. Fig. 1-10 illustrates common IGCC systems with  $\text{CO}_2$  capture. In Fig. 1-10(a), the IGCC system achieves  $\text{CO}_2$  capture though using

a water-gas shift reactor along with a CO<sub>2</sub> absorption unit. The purified syngas and steam are injected into the water-gas shift reactor together, which promotes the generation of H<sub>2</sub> and CO<sub>2</sub>. Then, the CO<sub>2</sub> in syngas is removed by absorption solvent. Although most of CO<sub>2</sub> is captured, some is still released into the atmosphere by chimney. The IGCC system shown in Fig. 1-10(b) can use O<sub>2</sub> produced from the air separation unit as the gasifying agent or one of gasifying agents and oxidant for electrical power generation process. Since most of N<sub>2</sub> is excluded from the IGCC system, the exhaust after condensation is almost CO<sub>2</sub>, which can be directly compressed and stored. Another IGCC system is composed of a chemical looping gasifier and an electrical power generation process (Fig. 1-10(c)). Tong et al. [72] reported that the chemical looping gasifier based on Fe-based oxygen carrier can capture nearly 100% CO<sub>2</sub> and provide a H<sub>2</sub> with purity of higher than 99.99% for electrical power generation process. However, the problem that direct reduction of iron oxides by solid fuels needs a long reaction time is still not solved, limiting the utilization in industry [73]. Recently, a CO<sub>2</sub> recovery type IGCC system was proposed in Japan, in which a part of captured CO<sub>2</sub> is recycled and used as the gasifying agent with pure O<sub>2</sub> [12]. In this IGCC system, the gasification can be enhanced by recycled CO<sub>2</sub> via Boudouard reaction ( $C + CO_2 \rightarrow 2CO$ ), resulting in a 2% improvement of cold gas efficiency [74].

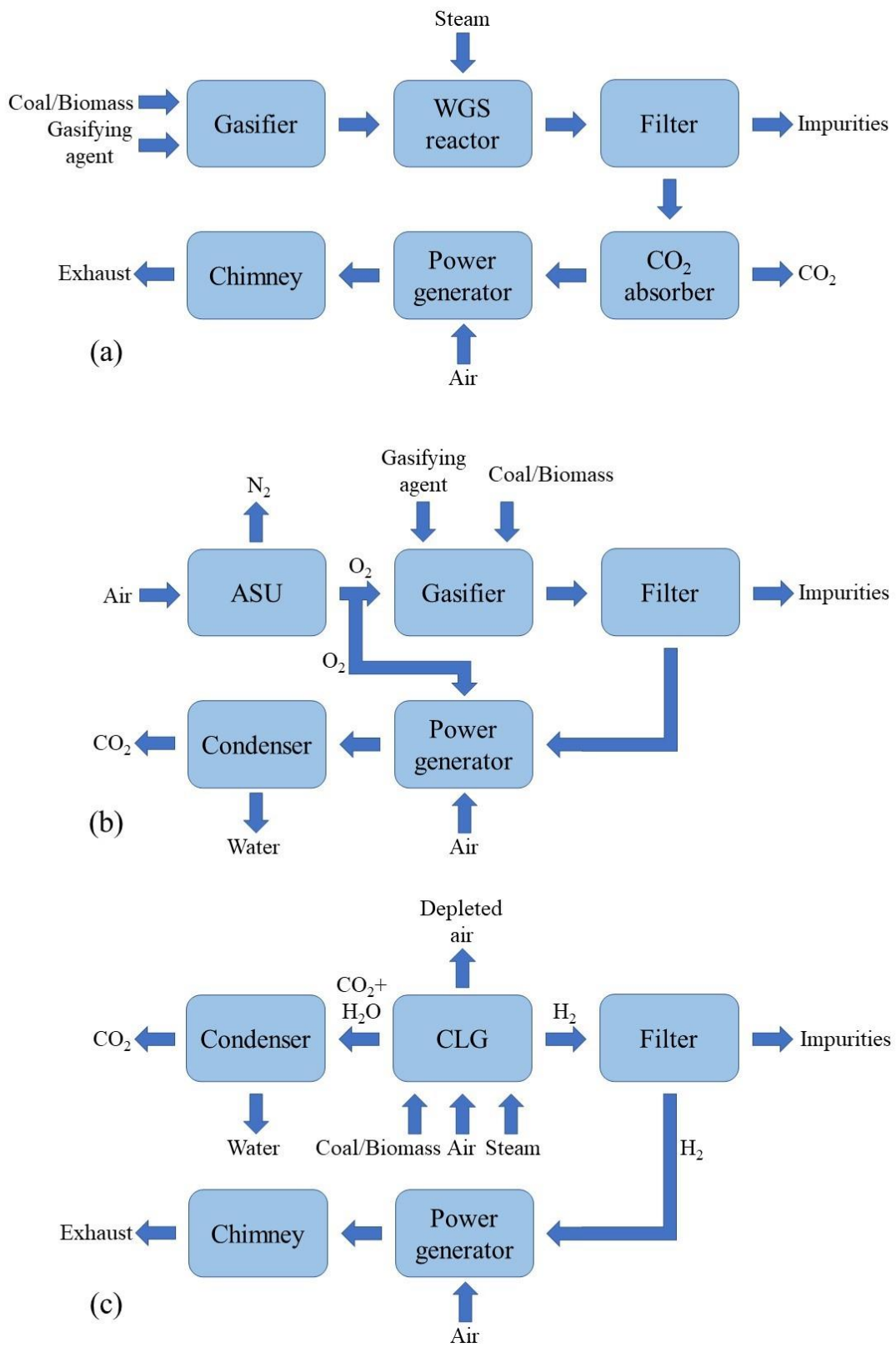


**Fig. 1-10** Simplified diagrams for IGCC systems with CO<sub>2</sub> capture.

### 1.3.1.2 Advanced IGCC/IGFC systems with exergy recovery

In order to maximize the fuel utilization and power generation, the exergy recuperation units can be considered in IGCC/IGFC system designs. The ideal gross thermal efficiencies (GTEs) of conventional IGCC and IGFC are 48%-52% and 55%-60% (based on Higher Heating Value, HHV), respectively [12]. However, there is also much exergy that is lost from the gasifier, SOFC, gas turbine and other auxiliary equipment. How to recuperate and reuse the exhausting exergy is also very important. As shown in Fig. 1-11, the advanced IGCC (A-IGCC) and advanced IGFC (A-IGFC) systems were proposed in Japan, in which a unique triple-bed combined circulating fluidized bed (TBCFB) gasifier is used to replace conventional high-temperature gasifiers, and the exhausted exergy from gas turbine (GT) or solid oxide fuel cells (SOFCs) is recycled to support the gasification process. According to some published reports, when the pyrolysis and gasification were carried out in the same reactor, the products of initial pyrolysis stage such as tar, light hydrocarbon gases and inorganic gases have severely negative effect on the gasification of the char [18]. To solve this problem, the high-density TBCFB (Fig. 1-12) composed of a downer pyrolyzer, a bubbling fluidized bed (BFB) char gasifier and a riser combustor is designed, which can realize the spatial subdivision of pyrolysis, gasification and combustion. The coal/biomass is pyrolyzed rapidly in the pyrolyzer at first, and then, the tar and gas produced from pyrolysis are separated from char using a fast gas-solid separator. The char enters the BFB gasifier and is gasified by the steam and the unreacted char flows into the riser combustor to be partial or completely oxidized. A large number of heat carriers such as sands circulate with a high mass flux to carry the heat produced from

combustor to pyrolyzer and char gasifier. As a result of simulation by HYSYS®.Plant (Aspen technology Inc.), the gross thermal efficiencies of A-IGCC and A-IGFC systems exergy-recuperative can reach as high as 57-59% and 70-76% (HHV) [18].

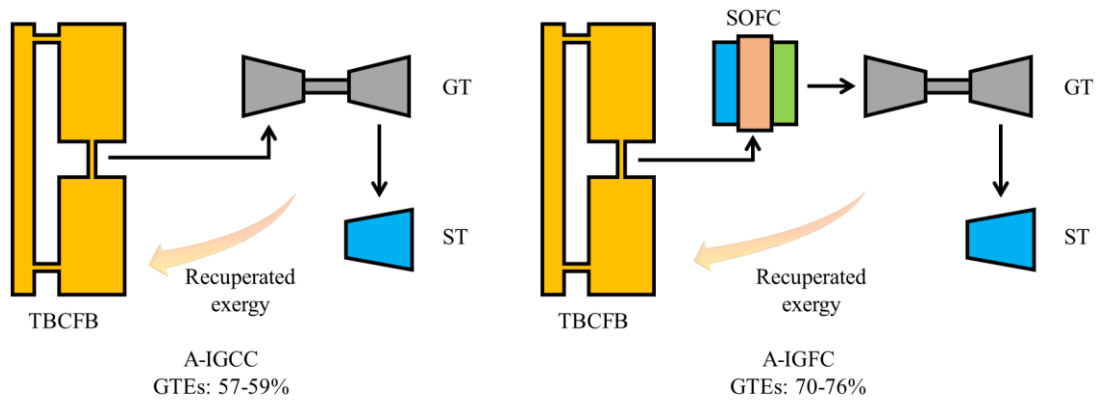


**Fig. 1-11** Basic structures of A-IGCC and A-IGFC systems.

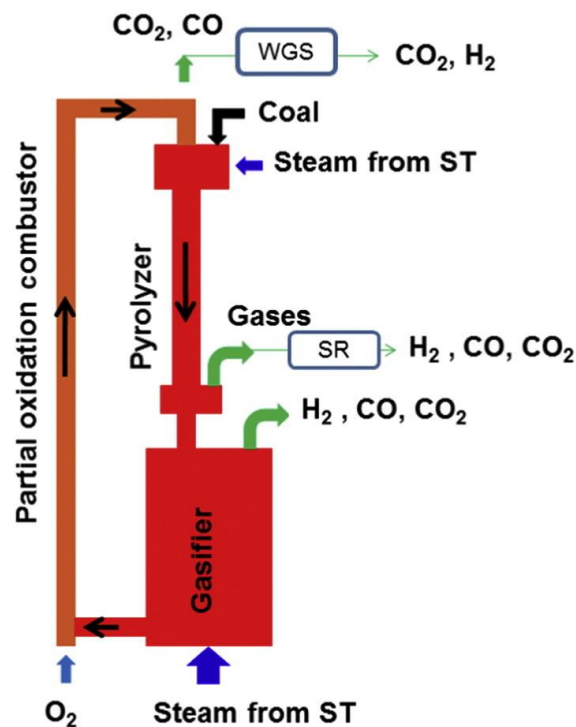


**Fig. 1-12** The high-density triple-bed combined circulating fluidized bed gasifier

(reprinted with permission from Ref. [12]).

### 1.3.2 Small-scale biomass gasification power generation systems

Different from coal, the biomass shows a scattered geographical distribution, which results in costs of collection and transportation [75]. In order to fully use the locally available biomass, the small-scale biomass power generation system should be more suitable for the biomass energy applications. To date, the small-scale biomass gasification-based power generation system has been made to commercialize and achieved a large market share [76]. On the other hand, the development of small-scale biomass gasifiers is being limited by the tar, which can cause the fouling of downstream process equipment, such as engine. Generally, the syngas produced from biomass gasification is known to contain tar in the range of 0.01-160 g/nm<sup>3</sup> [77]. As stated above, the approaches of wet scrubbing with water-based or oil-based absorbents have been widely used for large-scale gasification systems to eliminate tar. However, these approaches are not suitable for the small-scale and low-cost systems, due to the difficulties of wastewater treatment or oil-based absorbents regeneration [77]. Therefore, a simple and highly efficient approach of tar removal is considered as the key issue in design of small-scale biomass gasification power generation system.

In addition to the tar removal, the different occurrence temperature ranges with different reaction rates of biomass pyrolysis, volatiles reforming and bio-char gasification in biomass gasification also should be considered. For example, biomass pyrolysis and tar reforming are relatively fast reaction processes whereas it has to take a long time for the complete steam gasification of bio-char at a high temperature (800-1000 °C) [78]. Thus, the spatial subdivision of every processes in biomass gasification can be adopted to realize the optimization of each conversion step and improve the

whole performance [16].

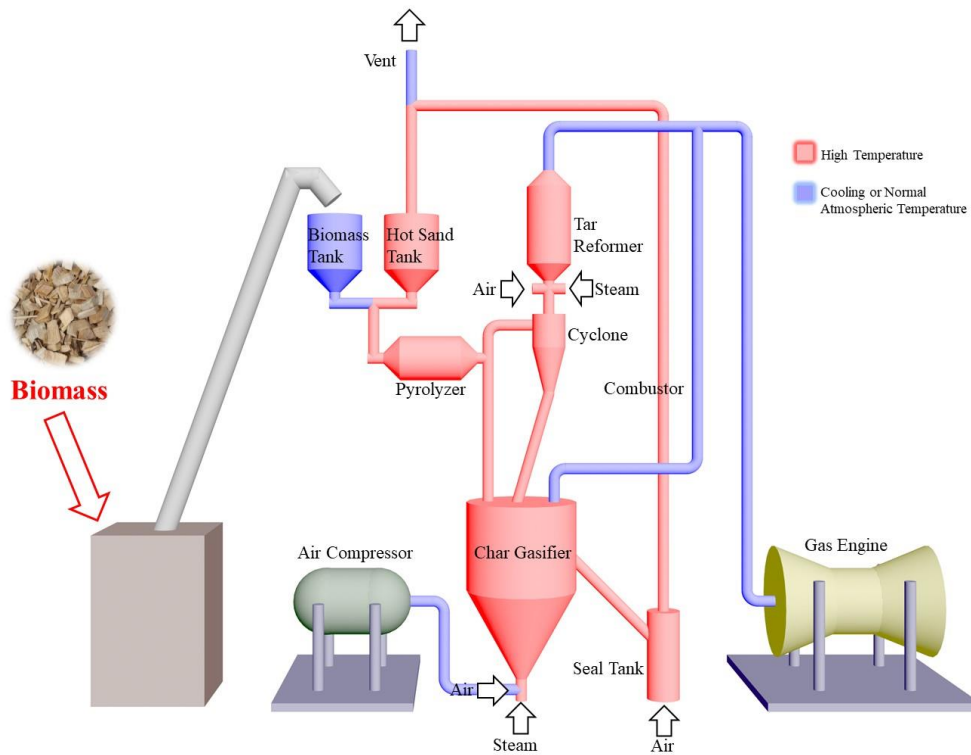


**Fig. 1-13** The small-scale separated-type biomass gasification system proposed by Guan et al. [75]

Recently, Guan et al. [75] proposed and assessed a small-scale separated-type biomass gasification system for biomass power generation (Fig. 1-13). In this system, the biomass and the circulated hot silica sands are introduced into the auger pyrolyzer firstly. As the biomass is mixed with the hot silica sands along the auger reactor, it will be decomposed to volatiles and char. The volatiles go upwards to the reformer where the volatiles can be catalytically converted to syngas. Meanwhile, the char flows downwards to a BFB char gasifier and is self-heatedly gasified with air/oxygen and steam to syngas. And then, the unreacted char overflows into a riser combustor and is burned completely. The generated heat from char combustion is carried by the silica



sands and recycled to the sand tank, and provided the heat for the biomass pyrolysis. The gas produced in the pyrolyzer, reformer, and char gasifier will be collected together and used as the fuel for the engine to generate electricity.

## 1.4 Dry reforming of methane

### 1.4.1 Description of dry reforming of methane

Dry reforming of methane is a thermochemical conversion process that consists of converting CO<sub>2</sub> and CH<sub>4</sub> into syngas with a ratio of H<sub>2</sub> to CO close to 1. This process can favor mitigation of the environmental challenges caused by CO<sub>2</sub> emissions. The main reactions occurring during DRM process are summarized as follows:

Methane CO<sub>2</sub> reforming:



Boudouard reaction:



Methane decomposition:



Water-gas shift reaction:



Methane steam reforming:



Methanation reaction:



Although the DRM is considered to have well environmental potentials, it has not yet reached full industrial maturity. As the oxidant, the CO<sub>2</sub> shows strong chemical stability, resulting in a large amount of energy requirement for the endothermic DRM reaction [22, 79]. A high operating temperature is essential to DRM, and the DRM process will be thermodynamically impeded when operating temperature is lower than 642 °C [80]. Another main technical challenge is the unavoidable deactivation of conventional catalysts resulting from rapid carbon deposition [22, 79]. In general, the CH<sub>4</sub> can be absorbed on the active sites of catalysts and dehydrogenated, producing hydrogen and a hydrocarbon species CH<sub>x</sub> (x = 0-4) [81]. When x = 0, the carbon deposition occurs on the active sites of catalysts. As indicated above, the key of DRM is how to achieve a system design, which considers enough heat input and avoid catalysts deactivation or realize catalysts regeneration simultaneously.

#### 1.4.2 Catalysts of dry reforming of methane

The reported man-made catalysts for DRM process generally consist of transition metals, such as Ni, Co, Cu, Fe or noble metals, such as Ru, Rh, Pd, Ir, Pt, and oxide supports, such as SiO<sub>2</sub>, Al<sub>2</sub>O<sub>3</sub>, MgO, TiO<sub>2</sub>, CaO, CeO<sub>2</sub>, ZrO<sub>2</sub>, or La<sub>2</sub>O<sub>3</sub> [22, 81]. Among the catalysts, noble metal catalysts are considered to be the best due to their high stability, superior carbon deposition resistance and highly catalytic activity [22]. However, the high cost of noble metal catalysts greatly reduces the profits of enterprises, leading to their unavailability in the industrial scale [82]. In this scenario, the low-cost transition metal catalysts with highly catalytic activity have become a suitable alternative for DRM process [83]. Although these transition metal catalysts perform

convenience for industrial applications, the problem of deactivation resulted from carbon deposition or sintering still is not solved [20]. Recently, some researchers have tried to add small amount of noble metals to transition metals to produce alloy-catalysts, which can consider both economy and stability [22].

In the man-made catalysts, support is important for the performance, and the synergistic effects could be caused by combining with the catalytically active metallic phase. Some textural and physicochemical properties, such as pore characteristics, specific surface area, thermal stability, redox properties, surface basicity and oxygen storage capacity, should be considered simultaneously to enhance the interaction between catalyst metals and supports [22]. The structure with many pores can increase the specific surface area to promote the dispersion of metal species and increase the amount of activity sites [69]. Moreover, the support can also resist the carbon deposition and prevent the catalyst active species from sintering [20].

### **1.4.3 Reactors of dry reforming of methane**

In the DRM industry, the reactors commonly used include the conventional fixed bed reactor and fluidized bed reactor and the novel plasma reactor and membrane reactor (Fig. 1-14).

The fixed bed reactors are always used as dry reformer of methane due to their relatively simple structure, easy operation and low cost [84]. According to the report of Dixon [85], in the case of highly endothermic DRM reactions, the fixed bed type dry reformer of methane should be designed as small tube-to-particle diameter ratio ( $D/d < 10$ ). Obviously, the catalyst particles can not be uniformly distributed in the fixed bed,

resulting in significant wall effects, local backflows and nonuniform temperature distribution [86].

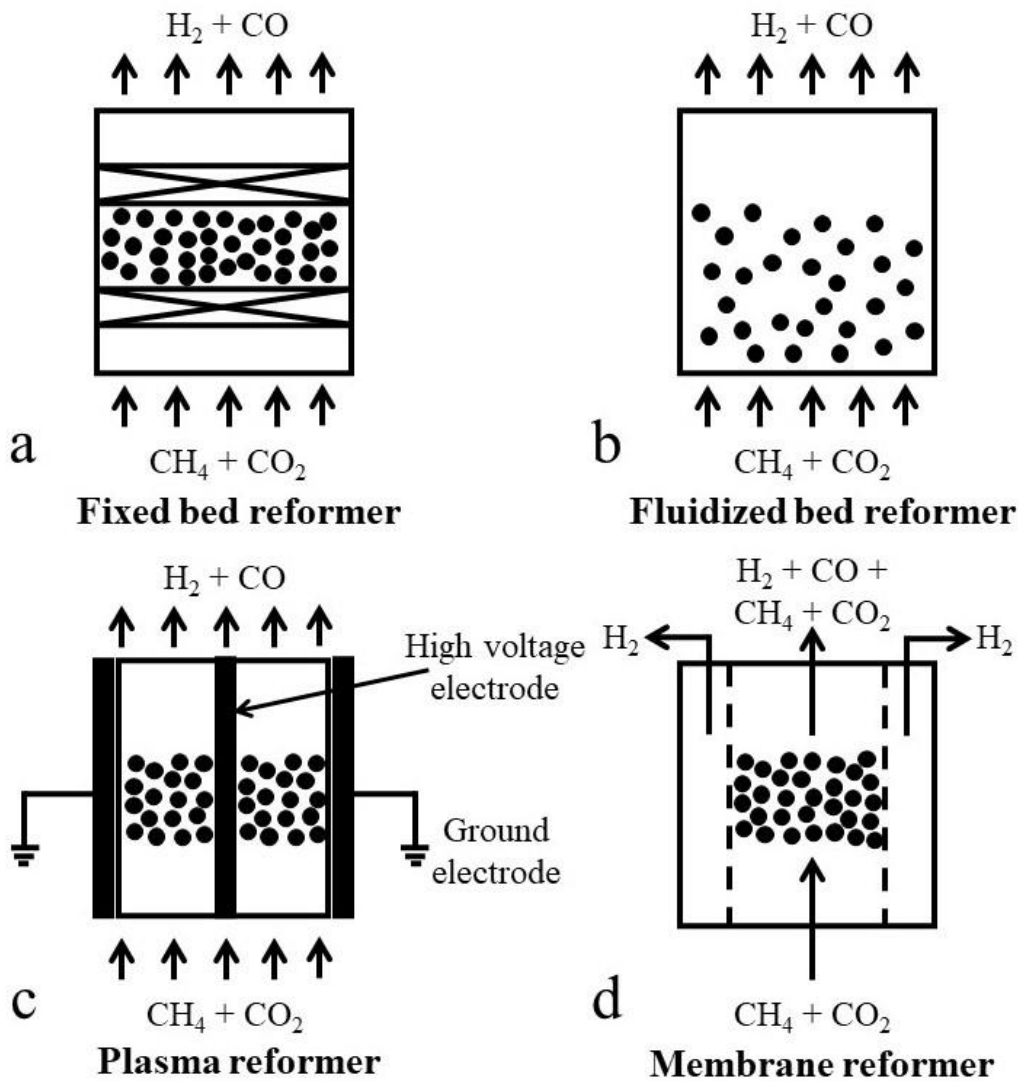


**Fig. 1-14** Schematic diagrams of (a) fixed bed reformer, (b) fluidized bed reformer, (c) plasma reformer, and (d) membrane reformer (modified from Ref. [81])

In contrast to fixed bed reactors, by using the fluidized bed, heat transfer capability is improved to refrain the formation of hot spots, and simultaneously the interaction between solids and gas can be enhanced [87]. Moreover, the circulating fluidized bed

design coupling a dry reformer with a catalyst regenerator can solve the rapid deactivation of catalysts resulted from carbon deposition [88]. However, in this case, the mechanical strength of catalyst to endure the collisions should be considered [69].

Both fixed bed reformer and fluidized bed reformer have to work under extreme condition with very high temperature, and usually suffer from the carbon deposition. In recent years, the non-thermal plasma DRM technology has been widely studied and tested [89]. The nonthermal plasma reactors can generate enough effective high-velocity electrons to collide with bulk gas molecules, causing fragmentation of gas molecules to form highly reactive ions and radicals [81]. In a non-thermal plasma DRM system, the physicochemical properties of the catalyst and plasma can be modified by the interaction between the plasma and catalyst. This interaction can not only improve the selectivity of the reaction significantly, but also have positive effects on the energy efficiency of the system [89].

According to Eqs. 1-14, the reversible nature of DRM forces fixed bed reformer and fluidized bed reformer to work at a condition of very high temperature to shift the reaction equilibrium towards the direction of  $H_2$  and  $CO$ . Some researchers tried to remove part of dry reforming products by membranes to achieve a high conversion of  $CO_2$  and  $CH_4$  to overcome the thermodynamical limitation [81]. There are two kinds of membrane reformers: inert membrane reactors and catalytic membrane reactors. The membrane of inert membrane reactors is only used to separate  $H_2$  from produced syngas, whereas the membrane of catalytic membrane reactors is used not only for  $H_2$  separation, but also as a catalyst or support to participate in the actual reactions. Although the membrane reformers can work at relatively low temperature and reduce

the usage of catalysts, the high expense of membrane materials prevents their application in the industrial scale [83].

#### **1.4.4 Autothermal dry reforming of methane**

As above stated, dry reforming process is endothermic and will be thermodynamically impeded when operating temperature is lower than 642 °C [80]. Although the catalysts developed in the laboratory can achieve the chemical conversion actively at relatively low temperature, they cannot be well adopted in the industrial scale. Therefore, for a DRM system, maintaining high temperature condition is the basis of high efficiency production. Generally, researchers adopt autothermal dry reforming of methane (ATDRM) which combines partial oxidation of methane (POM) and DRM to realize a stable energy supply [90-94]. In the ATDRM system, the mixture of CH<sub>4</sub>, CO<sub>2</sub> and O<sub>2</sub> is injected to a same reactor directly. Herein, the thermal energy produced by partial oxidation is used to promote the endothermic DRM reaction. Moreover, compared with single DRM process, the deposited carbon reformation becomes more difficult under the action of O<sub>2</sub> [95]. However, the introduce of O<sub>2</sub> to DRM will cause lower CO<sub>2</sub> conversion, because the CO<sub>2</sub> is produced from CH<sub>4</sub> oxidation inevitably [95, 96]. In addition, the produced H<sub>2</sub>O from CH<sub>4</sub> oxidation will shift the equilibrium of water-gas shift reaction (WGSR) towards the direction of CO<sub>2</sub> production.

### **1.5 Motivation and objectives**

Application of renewable carbon-based energies is an important direction to ensure energy supplement and to mitigate the negative impact of carbon dioxide emissions on

the environment in the future.

The major problems of low-rank coals are low heating value and high moisture and ash contents, determining that they are not suitable to be directly used as fuel in industrial process. Moreover, the combustion of low-rank coals without pretreatment can result in serious emissions of nitrogen species, sulfur species and particulate matters, which have severely damaged the health of humanity. The coal gasification has more advantages than the conventional coal combustion process and especially, it can provide a good choice of removing sulfur, nitrogen compounds and particulates. However, in the conventional gasifier, tar, light hydrocarbon gases and inorganic gases generated during the coal pyrolysis can hinder the gasification of char, and part of tar cannot be decomposed completely. Therefore, it is essential to develop a novel gasifier to solve these problems.

In addition to coals, the gasification technology can also be applied to improve the energy efficiency of biomass. Recently, the small-scale biomass power generation systems coupled with biomass gasification, which can fully use the locally available biomass, have been popular, since the increase of costs of collection and transportation caused by scattered geographical distribution of biomass limits the biomass energy application in the large scale. Due to the presence of operating temperature and reaction time difference of pyrolysis, gasification and oxidation, how to achieve the spatial subdivision and optimization of each conversion step has been the key issue to improve the whole performance in the small-scale biomass power generation systems.

Nowadays, the carbon capture and storage (CCS) technology has been applied extensively because of global warming. Since the conventional CCS technology greatly increases industrial costs, CO<sub>2</sub> is tried to be converted to high value-added syngas by

DRM to increase economic competitiveness. Many DRM systems tend to experience the problem of high energy requirement. Although ATDRM technology can overcome this problem, the CO<sub>2</sub> conversion efficiency decreases significantly due to coupling with methane oxidation. Therefore, how to increase CO<sub>2</sub> conversion and keep high exergy efficiency simultaneously must be considered in a ATDRM system design.

The main objectives of this study are focusing on the following points:

- (1) To investigate novel low-rank coal gasifier for advanced IGCC/IGFC systems;
- (2) To develop novel small-scale biomass-based combined heat and power (CHP) systems with high thermal efficiency for power generation;
- (3) To develop novel separated-type biomass gasifier for small-scale CHP systems;
- (4) To develop novel DRM system to reuse the CO<sub>2</sub> and decrease the CCS cost.

## **1.6 Organization and outline of this dissertation**

In this dissertation, a novel dense downer reactor for pyrolysis of separated-type large-scale coal gasifier was proposed firstly, Later, advanced small-scale biomass power generation system and methane dry reforming system were designed and analyzed. It includes the following 6 chapters:

**Chapter 1** introduces the current coal/biomass gasification technologies, dry reforming of methane technologies and their applications. The recent researches, development and existing problems are summarized and discussed. Finally, the motivation, objectives and outline of this research are given.

**Chapter 2** introduces the Computational Fluid Dynamics commercial software FLUENT 19.0 and Process Simulation commercial software Aspen Plus 10.0 used in



this study.

**Chapter 3** provides a design of dense downer for complete pyrolysis of low-rank coals. The influences of downer diameter, cone angle and solids mass flux on the hydrodynamic behaviors are investigated in details to obtain the optimal structural parameters and operating conditions and evaluate the performance of this dense downer.

**Chapter 4** reports the results of a biomass-based small-scale power generation system with energy/exergy recuperation. The spatial subdivision of the processes for the biomass pyrolysis, char combustion, tar reforming and catalyst regeneration is adopted by using a separated-type biomass gasifier design to realize the optimization of each conversion step and improve the whole system performance.

**Chapter 5** investigates and assesses a design of a small-scale separated-type biomass gasification system. By the simulation based on cold model, the hydrodynamics of this system are characterized and possibilities of achieving a good gas seal between BFB and riser are explored.

**Chapter 6** assesses the possibility of increasing CO<sub>2</sub> conversion by a separated-type autothermal CH<sub>4</sub> dry reforming system with exergy recuperation. The overall system efficiency is investigated by comparing conventional and separated-type CH<sub>4</sub> dry reforming systems.

**Chapter 7** summarizes the highlights of all results in this dissertation and provides the perspectives of the possible future work related with these researches.

## References

- [1] IEA, World Energy Outlook 2020, <https://www.iea.org/reports/world-energy->

[outlook-2020#](#); 2020 [accessed in 12 Jun 2020]

- [2] Xia Y, Zhang R, Cao Y, Xing Y, Gui X. Role of molecular simulation in understanding the mechanism of low-rank coal flotation: A review. *Fuel* 2020;262:116535.
- [3] Sivrikaya O. Cleaning study of a low-rank lignite with DMS, Reichert spiral and flotation. *Fuel* 2014;119:252-8.
- [4] Sakaguchi M, Laursen K, Nakagawa H, Miura K. Hydrothermal upgrading of Loy Yang Brown coal — Effect of upgrading conditions on the characteristics of the products. *Fuel Process Technol* 2008;89:391-6.
- [5] Bhutto AW, Bazmi AA, Zahedi G. Underground coal gasification: From fundamentals to applications. *Prog Energy Combust Sci* 2013;39:189-214.
- [6] Fan Y, Yi Q, Li F, Yi L, Li W. Tech-economic assessment of a coproduction system integrated with lignite pyrolysis and Fischer–Tropsch synthesis to produce liquid fuels and electricity. *Fuel Process Technol* 2015;135:180-6.
- [7] Aziz M, Juangsa FB, Kurniawan W, Budiman BA. Clean Co-production of H<sub>2</sub> and power from low rank coal. *Energy* 2016;116:489-97.
- [8] Habgood DCC, Hoadley AFA, Zhang L. Techno-economic analysis of gasification routes for ammonia production from Victorian brown coal. *Chem Eng Res Des* 2015;102:57-68.
- [9] Xie J, Xin L, Hu X, Cheng W, Liu W, Wang Z. Technical application of safety and cleaner production technology by underground coal gasification in China. *J Cleaner Prod* 2020;250:119487.
- [10] Maheshwari M, Singh O. Comparative evaluation of different combined cycle configurations having simple gas turbine, steam turbine and ammonia water turbine.

Energy 2019;168:1217-36.

[11] Chen S, Lior N, Xiang W. Coal gasification integration with solid oxide fuel cell and chemical looping combustion for high-efficiency power generation with inherent CO<sub>2</sub> capture. Appl Energy 2015;146:298-312.

[12] Guan G. Clean coal technologies in Japan: A review. Chin J Chem Eng 2017;25:689-97.

[13] Guan G, Kaewpanha M, Hao X, Abudula A. Catalytic steam reforming of biomass tar: Prospects and challenges. Renew Sustain Energy Rev 2016;58:450-61.

[14] Detchusananard T, Sharma S, Maréchal F, Arpornwichanop A. Multi-objective optimization of sorption enhanced steam biomass gasification with solid oxide fuel cell. Energy Convers Manage 2019;182:412-29.

[15] Sher F, Iqbal SZ, Liu H, Imran M, Snape CE. Thermal and kinetic analysis of diverse biomass fuels under different reaction environment: A way forward to renewable energy sources. Energy Convers Manage 2020;203:112266.

[16] Zhao Z, Andre Situmorang Y, An P, Yang J, Hao X, Rizkiana J, et al. A biomass-based small-scale power generation system with energy/exergy recuperation. Energy Convers Manage 2021;227.

[17] Caputo AC, Palumbo M, Pelagagge PM, Scacchia F. Economics of biomass energy utilization in combustion and gasification plants: effects of logistic variables. Biomass Bioenergy 2005;28:35-51.

[18] Guan G, Fushimi C, Tsutsumi A, Ishizuka M, Matsuda S, Hatano H, et al. High-density circulating fluidized bed gasifier for advanced IGCC/IGFC—Advantages and challenges. Particuology 2010;8:602-6.

[19] Mertzis D, Koufodimos G, Kavvadas I, Samaras Z. Applying modern automotive

technology on small scale gasification systems for CHP production: A compact hot gas filtration system. *Biomass Bioenergy* 2017;101:9-20.

[20] Jang WJ, Shim JO, Kim HM, Yoo SY, Roh HS. A review on dry reforming of methane in aspect of catalytic properties. *Catal Today* 2019;324:15-26.

[21] Li Y, Chen Y, Wu J. Enhancement of methane production in anaerobic digestion process: A review. *Appl Energy* 2019;240:120-37.

[22] Aramouni NAK, Touma JG, Tarboush BA, Zeaiter J, Ahmad MN. Catalyst design for dry reforming of methane: Analysis review. *Renew Sustain Energy Rev* 2018;82:2570-85.

[23] IPCC, Choices made now are critical for the future of our ocean and cryosphere, <https://www.ipcc.ch/2019/09/25/srocc-press-release/>; 2019 [accessed in 12 Jun 2020]

[24] Kiehl JT, Trenberth KE. Earth's Annual Global Mean Energy Budget. *Bull Am Meteorol Soc* 1997;78:197-208.

[25] IEA, Data and statistics: CO<sub>2</sub> emissions, <https://www.iea.org/data-and-statistics/?country=WORLD&fuel=CO2%20emissions&indicator=CO2BySource>; 2020 [accessed in 12 Jun 2020]

[26] IEA, Carbon capture, utilisation and storage, <https://www.iea.org/fuels-and-technologies/carbon-capture-utilisation-and-storage>; 2020 [accessed in 12 Jun 2020]

[27] Farajzadeh R, Eftekhari AA, Dafnomilis G, Lake LW, Bruining J. On the sustainability of CO<sub>2</sub> storage through CO<sub>2</sub> – Enhanced oil recovery. *Appl Energy* 2020;261:114467.

[28] Song C, Liu Q, Ji N, Deng S, Zhao J, Li Y, et al. Alternative pathways for efficient CO<sub>2</sub> capture by hybrid processes—A review. *Renew Sustain Energy Rev* 2018;82:215-31.

- [29] Wei T, Jia L, Luo J-L, Chi B, Pu J, Li J. CO<sub>2</sub> dry reforming of CH<sub>4</sub> with Sr and Ni co-doped LaCrO<sub>3</sub> perovskite catalysts. *Appl Surf Sci* 2020;506.
- [30] Li K, Chang X, Pei C, Li X, Chen S, Zhang X, et al. Ordered mesoporous Ni/La<sub>2</sub>O<sub>3</sub> catalysts with interfacial synergism towards CO<sub>2</sub> activation in dry reforming of methane. *Appl Catal, B* 2019;259.
- [31] Lino AVP, Calderon YNC, Mastelaro VR, Assaf EM, Assaf JM. Syngas for Fischer-Tropsch synthesis by methane tri-reforming using nickel supported on MgAl<sub>2</sub>O<sub>4</sub> promoted with Zr, Ce and Ce-Zr. *Appl Surf Sci* 2019;481:747-60.
- [32] Dai B, Zhang L, Cui J-f, Hoadley A, Zhang L. Integration of pyrolysis and entrained-bed gasification for the production of chemicals from Victorian brown coal — Process simulation and exergy analysis. *Fuel Process Technol* 2017;155:21-31.
- [33] Aziz M, Kansha Y, Tsutsumi A. Self-heat recuperative fluidized bed drying of brown coal. *Chemical Engineering and Processing: Process Intensification* 2011;50:944-51.
- [34] Bell DA, Towler BF, Fan M. *Coal gasification and its applications: William Andrew*; 2010.
- [35] Liu K, Song C, Subramani V. *Hydrogen and syngas production and purification technologies: John Wiley & Sons*; 2010.
- [36] Prabu V, Jayanti S. Underground coal-air gasification based solid oxide fuel cell system. *Appl Energy* 2012;94:406-14.
- [37] Chen C, Horio M, Kojima T. Numerical simulation of entrained flow coal gasifiers. Part II: effects of operating conditions on gasifier performance. *Chem Eng Sci* 2000;55:3875-83.
- [38] Giuffrida A, Romano MC, Lozza G. Thermodynamic analysis of air-blown

gasification for IGCC applications. *Appl Energy* 2011;88:3949-58.

[39] Irfan MF, Usman MR, Kusakabe K. Coal gasification in CO<sub>2</sub> atmosphere and its kinetics since 1948: A brief review. *Energy* 2011;36:12-40.

[40] Mahinpey N, Gomez A. Review of gasification fundamentals and new findings: Reactors, feedstock, and kinetic studies. *Chem Eng Sci* 2016;148:14-31.

[41] Ruiz JA, Juárez MC, Morales MP, Muñoz P, Mendivil MA. Biomass gasification for electricity generation: Review of current technology barriers. *Renew Sustain Energy Rev* 2013;18:174-83.

[42] Fushimi C, Ishizuka M, Guan G, Suzuki Y, Norinaga K, Hayashi J-i, et al. Hydrodynamic behavior of binary mixture of solids in a triple-bed combined circulating fluidized bed with high mass flux. *Adv Powder Technol* 2014;25:379-88.

[43] Hamel S, Hasselbach H, Weil S, Krumm W. Autothermal two-stage gasification of low-density waste-derived fuels. *Energy* 2007;32:95-107.

[44] Wang L, Weller CL, Jones DD, Hanna MA. Contemporary issues in thermal gasification of biomass and its application to electricity and fuel production. *Biomass Bioenergy* 2008;32:573-81.

[45] Collot A-G. Matching gasification technologies to coal properties. *International Journal of Coal Geology* 2006;65:191-212.

[46] Gong Y, Zhang Q, Zhu H, Guo Q, Yu G. Refractory failure in entrained-flow gasifier: Vision-based macrostructure investigation in a bench-scale OMB gasifier. *Appl Energy* 2017;205:1091-9.

[47] Martelli E, Kreutz T, Carbo M, Consonni S, Jansen D. Shell coal IGCCS with carbon capture: Conventional gas quench vs. innovative configurations. *Appl Energy* 2011;88:3978-89.

- [48] Omosun AO, Bauen A, Brandon NP, Adjiman CS, Hart D. Modelling system efficiencies and costs of two biomass-fuelled SOFC systems. *J Power Sources* 2004;131:96-106.
- [49] Kunze C, Spliethoff H. Modelling, comparison and operation experiences of entrained flow gasifier. *Energy Convers Manage* 2011;52:2135-41.
- [50] Gräbner M, Meyer B. Performance and exergy analysis of the current developments in coal gasification technology. *Fuel* 2014;116:910-20.
- [51] Kanniche M, Bouallou C. CO<sub>2</sub> capture study in advanced integrated gasification combined cycle. *Appl Therm Eng* 2007;27:2693-702.
- [52] Lin S, Harada M, Suzuki Y, Hatano H. Process analysis for hydrogen production by reaction integrated novel gasification (HyPr-RING). *Energy Convers Manage* 2005;46:869-80.
- [53] Lin S. Development of in-situ CO<sub>2</sub> capture coal utilization technologies. *Energy Procedia* 2013;37:99-106.
- [54] Zeng L, He F, Li F, Fan L-S. Coal-direct chemical looping gasification for hydrogen production: reactor modeling and process simulation. *Energy Fuels* 2012;26:3680-90.
- [55] Dolan MD, Ilyushechkin AY, McLennan KG, Sharma SD. Sulfur removal from coal-derived syngas: thermodynamic considerations and review. *Asia-Pac J Chem Eng* 2012;7:1-13.
- [56] Zetterdahl M, Moldanová J, Pei X, Pathak RK, Demirdjian B. Impact of the 0.1% fuel sulfur content limit in SECA on particle and gaseous emissions from marine vessels. *Atmos Environ* 2016;145:338-45.
- [57] Yrjas P, Iisa K, Hupa M. Limestone and dolomite as sulfur absorbents under

pressurized gasification conditions. *Fuel* 1996;75:89-95.

[58] Abdoulmoumine N, Adhikari S, Kulkarni A, Chattanathan S. A review on biomass gasification syngas cleanup. *Appl Energy* 2015;155:294-307.

[59] Descamps C, Bouallou C, Kanniche M. Efficiency of an Integrated Gasification Combined Cycle (IGCC) power plant including CO<sub>2</sub> removal. *Energy* 2008;33:874-81.

[60] Mondal P, Dang GS, Garg MO. Syngas production through gasification and cleanup for downstream applications — Recent developments. *Fuel Process Technol* 2011;92:1395-410.

[61] Huang CC, Chen CH, Chu SM. Effect of moisture on H<sub>2</sub>S adsorption by copper impregnated activated carbon. *J Hazard Mater* 2006;136:866-73.

[62] Resnik KP, Pennline HW. Study of an ammonia-based wet scrubbing process in a continuous flow system. *Fuel* 2013;105:184-91.

[63] Kim YM, Park D, Lee DS, Park JM. Inhibitory effects of toxic compounds on nitrification process for cokes wastewater treatment. *J Hazard Mater* 2008;152:915-21.

[64] Pröll T, Siefert IG, Friedl A, Hofbauer H. Removal of NH<sub>3</sub> from biomass gasification producer gas by water condensing in an organic solvent scrubber. *Ind Eng Chem Res* 2005;44:1576-84.

[65] Jansen JIC, Jönsson K, Hagman M. Biological detoxification of tar-water. *Water Sci Technol* 2002;46:59-65.

[66] Zwart R, Van der Drift A, Bos A, Visser H, Cieplik M, Könemann H. Oil-based gas washing—Flexible tar removal for high-efficient production of clean heat and power as well as sustainable fuels and chemicals. *Environ Prog Sustain Energy* 2009;28:324-35.

[67] Coll R, Salvado J, Farriol X, Montane D. Steam reforming model compounds of biomass gasification tars: conversion at different operating conditions and tendency



towards coke formation. *Fuel Process Technol* 2001;74:19-31.

[68] Nam H, Wang Z, Shanmugam SR, Adhikari S, Abdoulmoumine N. Chemical looping dry reforming of benzene as a gasification tar model compound with Ni- and Fe-based oxygen carriers in a fluidized bed reactor. *Int J Hydrogen Energy* 2018;43:18790-800.

[69] Zhao Z, Situmorang YA, An P, Chaihad N, Wang J, Hao X, et al. Hydrogen production from catalytic steam reforming of bio-oils: a critical review. *Chemical Engineering Technology* 2020;43:625-40.

[70] Siefert NS, Litster S. Exergy and economic analyses of advanced IGCC–CCS and IGFC–CCS power plants. *Appl Energy* 2013;107:315-28.

[71] Najafi B, Haghghat Mamaghani A, Baricci A, Rinaldi F, Casalegno A. Mathematical modelling and parametric study on a 30 kWel high temperature PEM fuel cell based residential micro cogeneration plant. *Int J Hydrogen Energy* 2015;40:1569-83.

[72] Tong A, Sridhar D, Sun Z, Kim HR, Zeng L, Wang F, et al. Continuous high purity hydrogen generation from a syngas chemical looping 25kWth sub-pilot unit with 100% carbon capture. *Fuel* 2013;103:495-505.

[73] Yu Z, Yang Y, Yang S, Zhang Q, Zhao J, Fang Y, et al. Iron-based oxygen carriers in chemical looping conversions: A review. *Carbon Resources Conversion* 2019;2:23-34.

[74] Oki Y, Inumaru J, Hara S, Kobayashi M, Watanabe H, Umemoto S, et al. Development of oxy-fuel IGCC system with CO<sub>2</sub> recirculation for CO<sub>2</sub> capture. *Energy Procedia* 2011;4:1066-73.

[75] Situmorang YA, Zhao Z, Yoshida A, Kasai Y, Abudula A, Guan G. Potential power generation on a small-scale separated-type biomass gasification system. *Energy* 2019;179:19-29.

- [76] Dong L, Liu H, Riffat S. Development of small-scale and micro-scale biomass-fuelled CHP systems – A literature review. *Appl Therm Eng* 2009;29:2119-26.
- [77] Madav V, Das D, Kumar M, Surwade M, Parikh PP, Sethi V. Studies for removal of tar from producer gas in small scale biomass gasifiers using biodiesel. *Biomass Bioenergy* 2019;123:123-33.
- [78] Dupont C, Boissonnet G, Seiler J-M, Gauthier P, Schweich D. Study about the kinetic processes of biomass steam gasification. *Fuel* 2007;86:32-40.
- [79] Carapellucci R, Giordano L. Steam, dry and autothermal methane reforming for hydrogen production: A thermodynamic equilibrium analysis. *J Power Sources* 2020;469.
- [80] Izquierdo-Colorado A, Dębek R, Da Costa P, Gálvez ME. Excess-methane dry and oxidative reforming on Ni-containing hydrotalcite-derived catalysts for biogas upgrading into synthesis gas. *Int J Hydrogen Energy* 2018;43:11981-9.
- [81] Fan M-S, Abdullah AZ, Bhatia S. Catalytic Technology for Carbon Dioxide Reforming of Methane to Synthesis Gas. *ChemCatChem* 2009;1:192-208.
- [82] Crisafulli C, Scirè S, Minicò S, Solarino L. Ni–Ru bimetallic catalysts for the CO<sub>2</sub> reforming of methane. *Appl Catal, A* 2002;225:1-9.
- [83] Usman M, Wan Daud WMA, Abbas HF. Dry reforming of methane: Influence of process parameters—A review. *Renew Sustain Energy Rev* 2015;45:710-44.
- [84] Gao Y, Jiang J, Meng Y, Yan F, Aihemaiti A. A review of recent developments in hydrogen production via biogas dry reforming. *Energy Convers Manage* 2018;171:133-55.
- [85] Dixon AG. Heat transfer in fixed beds at very low (< 4) tube-to-particle diameter ratio. *Ind Eng Chem Res* 1997;36:3053-64.

- [86] Eppinger T, Wehinger GD, Jurtz N, Aglave R, Kraume M. A numerical optimization study on the catalytic dry reforming of methane in a spatially resolved fixed-bed reactor. *Chem Eng Res Des* 2016;115:374-81.
- [87] Abashar M. Coupling of steam and dry reforming of methane in catalytic fluidized bed membrane reactors. *Int J Hydrogen Energy* 2004;29:799-808.
- [88] Ugarte P, Durán P, Lasobras J, Soler J, Menéndez M, Herguido J. Dry reforming of biogas in fluidized bed: Process intensification. *Int J Hydrogen Energy* 2017;42:13589-97.
- [89] Vakili R, Gholami R, Stere CE, Chansai S, Chen H, Holmes SM, et al. Plasma-assisted catalytic dry reforming of methane (DRM) over metal-organic frameworks (MOFs)-based catalysts. *Appl Catal, B* 2020;260.
- [90] Halabi M, de Croon M, van der Schaaf J, Cobden P, Schouten J. Modeling and analysis of autothermal reforming of methane to hydrogen in a fixed bed reformer. *Chem Eng J* 2008;137:568-78.
- [91] Dega FB, Chamoumi M, Braidy N, Abatzoglou N. Autothermal dry reforming of methane with a nickel spinellized catalyst prepared from a negative value metallurgical residue. *Renewable Energy* 2019;138:1239-49.
- [92] Shahhosseini HR, Saeidi S, Najari S, Gallucci F. Comparison of conventional and spherical reactor for the industrial auto-thermal reforming of methane to maximize synthesis gas and minimize CO<sub>2</sub>. *Int J Hydrogen Energy* 2017;42:19798-809.
- [93] Akri M, Achak O, Granger P, Wang S, Batiot-Dupeyrat C, Chafik T. Autothermal reforming of model purified biogas using an extruded honeycomb monolith: A new catalyst based on nickel incorporated illite clay promoted with MgO. *J Cleaner Prod* 2018;171:377-89.

- [94] Akri M, Chafik T, Granger P, Ayrault P, Batiot-Dupeyrat C. Novel nickel promoted illite clay based catalyst for autothermal dry reforming of methane. *Fuel* 2016;178:139-47.
- [95] Nikoo MK, Amin NAS. Thermodynamic analysis of carbon dioxide reforming of methane in view of solid carbon formation. *Fuel Process Technol* 2011;92:678-91.
- [96] Zhu J, Zhang D, King K. Reforming of CH<sub>4</sub> by partial oxidation: thermodynamic and kinetic analyses. *Fuel* 2001;80:899-905.

## CHAPTER 2: Simulation Software and Models

### 2.1 Computational fluid dynamics simulation

Computational fluid dynamics (CFD) is an interdisciplinary science combined modern fluid mechanics, numerical mathematics and computer science together. In CFD simulation, the integral and differential terms in the governing equations of fluid mechanics are approximately expressed as discrete algebraic forms, making them algebraic equations. And then, the discrete algebraic equations are solved by computer to obtain the numerical solutions at discrete time or space points. The CFD can almost replace the high-cost experimental equipment of fluid dynamics by complex numerical simulation and computer experiment, supporting the development of science and engineering technology.

In this study, the Eulerian-Eulerian model is applied to achieve the simulation of the gas-solids flow behaviors in gasifiers. In the Eulerian-Eulerian model, which is also named as Two-Fluid model (TFM), both continuous phase and dispersed phase are considered to be continuous. It is the most complex one of two-phase flow models and usually used for simulation of fluidized bed reactors. In my work, CFD commercial software FLUENT 19.0 is used to implement the Eulerian-Eulerian model. FLUENT 19.0 has many physical models, advanced numerical simulation methods and excellent pre-processing and post-processing functions, which can be used to simulate the complex flow. FLUENT 19.0 software adopts a solver based on the finite volume method and unstructured mesh, which can accurately simulate laminar flow, turbulence, heat transfer and chemical reaction. The detailed mathematical simulation models











coupled in FLUENT 19.0 software will be introduced in **chapter 3** and **chapter 5**.


## **2.2 Process simulation**

Process simulation is usually used to achieve the model-based representation of chemical, physical, biological, and other technical processes and operations of each unit in a system by computer software. In the process simulation, balances of material, heat, thermodynamic; rate correlations for momentum, heat, and mass transfer; and reaction stoichiometry and kinetic data are calculated to obtain the accurate products output and energy output or requirement, according to the operating parameter setting and material feeding. In this dissertation, the process simulation is applied to the study of **chapter 4** and **chapter 6**.

The most popular commercial software for process simulation is Aspen Plus<sup>TM</sup> (Aspen Technology Inc.), which also is used in this study. “Aspen” means Advanced System for Process Engineering. As a mature flowsheet simulator, Aspen Plus can accurately predict the behavior of a process using basic engineering relationships. It is usually used as preliminary study for design, optimization investigations, sensitivity analyses of the target system. Moreover, energy analyses and economic evaluation also been integrated in the recent versions of Aspen Plus. In Aspen Plus software, the flowsheet notation consists of stream icons and block icons. The stream icons are separated into material, heat, and work streams, and the block icons are categorized to mixers/splitters, separators, exchangers, columns, reactors, pressure changes, manipulators, solids, solids separators, and user models. The block icons used in this study are listed in **Table 2-1**.

**Table 2-1** Block icons of Aspen Plus used in this study

Name	Icon	Function
Mixers/Splitters		
MIX		Stream mixer. Also used to heat or work streams. Help for usage.
SSplit		Substream splitter. Divides beside on splits specified for each substream.
Separators		
Flash2		Two-outlet flash. Models flash drums, evaporators, etc. using rigorous VL or VLL equil.
Sep		Component separator. Separate components based on specified flows or split fractions.
Exchangers		
Heater		Thermal and phase state changer. Models heaters, coolers, condensers, etc.
HeatX		2 stream cocurrent or countercurrent heat exchanger.
MHeatX		Multistream heat exchanger. Model LNG exchangers, cold boxes, etc., and performs zone analysis.
Reactors		
RYield		Nostoichiometric reactor based on known yield distribution.
RGibbs		Rigorous reaction and/or multiphase equilibrium based on Gibbs free energy minimization.
Pressure changers		
Pump		Pump or hydraulic turbine.

Compr		Compressor/turbine. Models polytropic or isentropic compressors, etc.
-------	---	---



## **CHAPTER 3: Numerical Simulation of Hydrodynamic Behaviors in A Gas-Solids Dense Downer Reactor**

### **3.1 Introduction**

According to the World Energy Outlook 2020, coal is still the second world-wide energy resource after oil and provides about 26.2% of the world's energy consumption [1]. In order to use coal very efficiently and completely, the integrated coal gasification combined cycle (IGCC) system and integrated gasification fuel cell combined cycle (IGFC) system have been developed widely [2-4]. However, exergy loss is still high in the conventional IGCC/IGFC system. To solve this problem, an advanced IGCC (A-IGCC) system and an advanced IGFC (A-IGFC) system are proposed based on the exergy recuperation concept, which could recycle the exhaust heat of the gas turbine or solid oxide fuel cell by steam and achieve higher power generation efficiencies [3-15]. To realize the A-IGCC/A-IGFC technologies, a novel triple-bed combined circulating fluidized bed (TBCFB) gasifier was proposed, in which the recycled steam is utilized as one of heat sources for endothermic char gasification [3, 4, 13-16] and the gasifier is operated at relatively low temperatures. Since tar, light hydrocarbon gases and inorganic gases generated during the coal pyrolysis will hinder the gasification of char, the TBCFB system with a downer (coal pyrolyzer), a bubbling fluidized bed (low-temperature coal-char gasifier) and a riser (the remaining char combustor) was developed [4, 9, 11-15, 17-22]. In this system, coal is pyrolyzed quickly in the downer-type pyrolyzer at first and then, the produced fuel gases are quickly separated from the

char by using a gas-solids separator, and the char enters the bubbling fluidized bed gasifier for steam gasification. Since the char cannot be completely gasified, the non-gasifying char is moved into the riser combustor and combusted by air to generate heat. Herein, the heat is carried by heat-carrying particles such as silica sand or porous tar capture and cracking particles, which are circulated in the TBCFB system to transfer the heat from the riser to the downer reactor for the coal pyrolysis and the bubbling fluidized bed for the char gasification [4]. As such, the total gasification efficiency can be improved effectively [3, 4].

The downer pyrolyzer is an important part of this TBCFB gasification system and many previous works have been performed for it. Guan *et al.* [13] investigated the solids holdup in the case of a high solids mass flux ( $G_s = 406 \text{ kg/m}^2\text{s}$ ), and found that the average solids holdup decreased from 0.0212 to 0.0128 in the developed region of the downer pyrolyzer by increasing the downer gas superficial velocity from 0 to 1 m/s. In order to increase the solids mass flux more, they set up a gas seal bed (GSB) in the TBCFB system, and concluded that the solids holdup in the developed region of downer with a gas superficial velocity of 3 m/s could exceed 0.1 as the length of GSB was larger than 7.53 m [9]. Fushimi *et al.* [23] analyzed the pyrolysis and tar reforming processes in a lab-scale downer pyrolyzer at 1173 K in the absence and presence of the steam and found that the estimated residence time of coal particles was 0.54-0.61 s, in which the temperature of coal particles can be raised to 1053-1160 K. However, they considered that the low solids holdup and short residence time were not enough for the full coal pyrolysis and tar decomposition. In this case heavy tar could be adhered on the surfaces of silica sand and get into the char gasifier with the char. In order to completely pyrolyze coal as well as decompose the heavy tar in the conventional downer, it is

necessary to increase residence time and/or enhance the heat transfer in the downer pyrolyzer. However, the increase of length of downer pyrolyzer to extend the residence time will increase the total height of the set-up, resulting in a high cost. Meanwhile, an excellent heat transfer needs a high solids holdup, but it is difficult to achieve a solids holdup higher than 0.1 by increasing the solids mass flux in the conventional cylindrical downer. To solve this issue, Lian *et al.* [15] proposed and simulated a conical downer. Comparing with the conventional cylindrical downer, the conical downer could increase solids holdup by about 14%. However, the increase of solids holdup was still not enough to satisfy the reaction. Thus, as seen in Fig. 3-1, a novel gas-solids dense downer reactor was proposed to connect with the dilute downer with a cone structure in this study. The cone structure can change the direction of particle movement rapidly and concentrate particles on the dense downer, achieving a high solids holdup. The high solids holdup can enhance the contact of heat-carrying particles with the coal and char particles and increase radiative and convective heat transfer to coal so that the unpyrolyzed coal particles and the remaining tar can be completely decomposed in it and only the char is fed into the char gasifier.

To sufficiently reduce the entrainment of unpyrolyzed coal and heavy tar from the downer pyrolyzer to the following gas-solid separator and char gasifier, it is very important to know the flow behaviors in such a dense downer. In this study, Computational Fluid Dynamics (CFD) numerical simulation was used to systematically investigate the flow behaviors in such a dense downer. The objectives are to characterize the hydrodynamics of the dense downer and explore the optimal structure for achieving a high solids holdup in it. Influences of the diameter of dense downer ( $D = 25\text{-}35\text{ mm}$ ), cone angle ( $\alpha = 30\text{-}75^\circ$ ) and solids mass flux ( $G_s = 212.2\text{-}1167.1\text{ kg/m}^2\text{s}$ )

on the flow behaviors were investigated in details. It is expected to offer some qualitative understandings on the flow behaviors in the dense downer and provide a guidance to improve the solids holdup in the pyrolyzer.

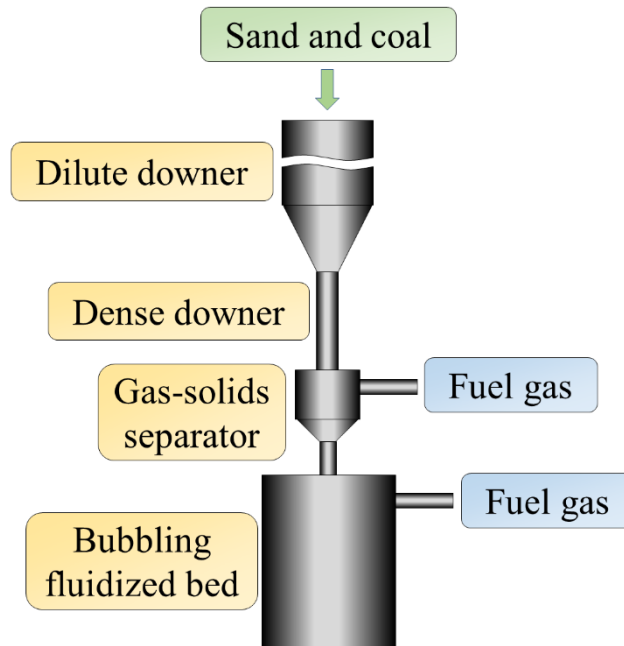


**Fig. 3-1.** Schematic diagram of apparatus.

## 3.2 Simulation methods

The dense downer reactor system contains silica sand as the solids phase and air as the gas phase.

### 3.2.1 Mathematical model

The gas-solids flow behavior was simulated by using Eulerian-Eulerian two-fluid model incorporated with the kinetic theory of granular flow (KTGF). Herein, the  $k-\epsilon$

model was used to describe the turbulence of gas, and the KTGF is used to describe the collision behavior of solid particles. The governing equations are summarized as follows (subscripts of g and s referred to gas and sand, respectively): [24-37]

The continuity equations of gas and solids phases,

$$\frac{\partial(\alpha_g \rho_g)}{\partial t} + \nabla(\alpha_g \rho_g \bar{v}_g) = 0, \quad (3-1)$$

$$\frac{\partial(\alpha_s \rho_s)}{\partial t} + \nabla(\alpha_s \rho_s \bar{v}_s) = 0, \quad (3-2)$$

Momentum conservation equations for gas and solids phases,

$$\frac{\partial}{\partial t}(\alpha_g \rho_g \bar{v}_g) + \nabla \cdot (\alpha_g \rho_g \bar{v}_g \bar{v}_g) = -\alpha_g \nabla p + \nabla \cdot \bar{\tau}_g + K_{gs}(\bar{v}_s - \bar{v}_g) + \alpha_g \rho_g \bar{g}, \quad (3-3)$$

$$\frac{\partial}{\partial t}(\alpha_s \rho_s \bar{v}_s) + \nabla \cdot (\alpha_s \rho_s \bar{v}_s \bar{v}_s) = -\alpha_s \nabla p - \nabla p_s + \nabla \cdot \bar{\tau}_s + K_{gs}(\bar{v}_g - \bar{v}_s) + \alpha_s \rho_s \bar{g}. \quad (3-4)$$

The turbulent kinetic energy and turbulent dissipation rate in the k-ε model were given as follows:

$$\frac{\partial}{\partial t}(\alpha_g \rho_g k_g) + \nabla(\alpha_g \rho_g k_g \bar{v}_g) = \nabla \left( \alpha_g \frac{\mu_{t,g}}{\sigma_k} \nabla k_g \right) + \alpha_g G_{k,g} - \alpha_g \rho_g \varepsilon_g + \alpha_g \rho_g \Pi_{k_g}, \quad (3-5)$$

$$\frac{\partial}{\partial t}(\alpha_g \rho_g \varepsilon_g) + \nabla(\alpha_g \rho_g \varepsilon_g \bar{v}_g) = \nabla \left( \alpha_g \frac{\mu_{t,g}}{\sigma_k} \nabla \varepsilon_g \right) + \alpha_g \frac{\varepsilon_g}{k_g} (C_{1\varepsilon} G_{k,g} - C_{2\varepsilon} \rho_g \varepsilon_g) + \alpha_g \rho_g \Pi_{\varepsilon_g}, \quad (3-6)$$

The concept of KTGF, which considers the conservation of particles velocity fluctuation energy, was used to close solids stress terms [37]. The motion of single particle in gas-solids flow was considered to be similar as the thermal motion of gas molecule. Herein, there is a random fluctuation of single particle, which is caused by collision of particles. Based on the random fluctuation of particle, the concept of “particle temperature” was proposed and adopted in the Gidaspow’s model [27].

$$\frac{3}{2} \left[ \frac{\partial}{\partial t} (\rho_s \alpha_s \Theta_s) + \nabla (\rho_s \alpha_s \vec{v}_s \Theta_s) \right] = \left( -p_s \bar{I} + \bar{\tau}_s \right) : \nabla \vec{v}_s + \nabla (k_{\Theta_s} \nabla \Theta_s) - \gamma_{\Theta_s} + \varphi_{gs}. \quad (3-7)$$

In order to accurately describe the interaction between gas and solids phases, Gidaspow's drag force model was used to calculate the momentum transfer in this study [27]. The corresponding equations of drag coefficient are written as follows:

$$\text{at } \alpha_g > 0.8, \quad K_{gs} = \frac{3}{4} C_D \frac{\alpha_s \alpha_g \rho_g |\vec{v}_s - \vec{v}_g|}{d_s} \alpha_g^{-2.65}, \quad (3-8)$$

$$\text{and at } \alpha_g \leq 0.8, \quad K_{gs} = 150 \frac{\alpha_s (1 - \alpha_g) \mu_g}{\alpha_g d_s^2} + \frac{7}{4} \frac{\alpha_s \rho_g |\vec{v}_s - \vec{v}_g|}{d_s}. \quad (3-9)$$

$$C_D = \frac{24}{\alpha_g \text{Re}_s} \left[ 1 + 0.15 (\alpha_g \text{Re}_s)^{0.687} \right], \quad \text{for } \text{Re}_s > 1000, \quad (3-10)$$

$$C_D = 0.44, \quad \text{for } \text{Re}_s \leq 1000, \quad (3-11)$$

$$\text{and } \text{Re}_s = \frac{\rho_g d_s |\vec{v}_s - \vec{v}_g|}{\mu_g}. \quad (3-12)$$

Constitutive equations for the solids phase stress based on the kinetic theory concepts of Lun *et al.* [28] and widely applied in the CFD simulation studies. In this study, the following constitutive equations were used.

The closure for gas phase stress tensor,

$$\bar{\tau}_g = \alpha_g \mu_g \left( \nabla \vec{v}_g + \nabla \vec{v}_g^T \right); \quad (3-13)$$

The closure for gas phase stress tensor,

$$\bar{\tau}_s = \alpha_s \mu_s \left( \nabla \vec{v}_s + \nabla \vec{v}_s^T \right) + \alpha_s \left( \lambda_s - \frac{2}{3} \mu_s \right) \nabla \vec{v}_s; \quad (3-14)$$

where, the bulk viscosity,

$$\lambda_s = \frac{4}{3} \alpha_s^2 \rho_s d_s g_0 (1 + e_s) \left( \frac{\Theta_s}{\pi} \right)^{1/2}; \quad (3-15)$$

in which, the radial distribution function,

$$g_0 = \left[ 1 - \left( \frac{\alpha_s}{\alpha_{s,\max}} \right)^{1/3} \right]^{-1}; \quad (3-16)$$

the solids shear viscosity,

$$\mu_s = \mu_{s,col} + \mu_{s,kin} + \mu_{s,fr}; \quad (3-17)$$

the solids collision viscosity,

$$\mu_{s,col} = \frac{4}{5} \alpha_s \rho_s d_s g_0 \cdot (1 + e_s) \cdot \left( \frac{\Theta_s}{\pi} \right)^{1/2}; \quad (3-18)$$

the kinetic viscosity (Gidasapow),

$$\mu_{s,kin} = \frac{10 \rho_s d_s (\Theta_s \pi)^{1/2}}{96 \alpha_s (1 + e_s) g_0} \left[ 1 + \frac{4}{5} g_0 \alpha_s \cdot (1 + e_s) \right]^2; \quad (3-19)$$

the solids frictional viscosity,

$$\mu_{s,fr} = \frac{p_s \sin \theta}{2 I_{2D}^{1/2}}; \quad (3-20)$$

the collision dissipation energy,

$$\gamma_{\Theta_s} = \frac{12 \cdot (1 - e_s^2) \cdot g_0}{d_s \sqrt{\pi}} \rho_s \alpha_s^2 \Theta_s^{3/2}; \quad (3-21)$$

and the solids pressure,

$$p_s = \alpha_s \rho_s \Theta_s + 2 \rho_s (1 + e_s) \alpha_s^2 g_0 \Theta_s. \quad (3-22)$$

### 3.2.2 Verification of model correctness

Since this work is concentrated in a prediction of the novel dense downer, we used

the method mentioned above to simulate a conventional downer reported by Guan *et al.* [38] and compared the simulation results with the experimental data to verify the model correctness. Herein, the experiment mainly focused on the investigation of average solids holdup and was carried out under a cold state (no chemical reactions, material consumption, or product generation). Fig. 3-2 shows the comparison results. The solid and dashed lines signify the experimental and simulation results, respectively. It can be seen that a downward average solids holdup trend existed with the increase of superficial gas velocity and the maximum difference between experimental and simulation results was less than 0.015. Based on the similarities of these two sets of results, the methods can be then further used to evaluate the flow behaviors in the dense downer in this study.

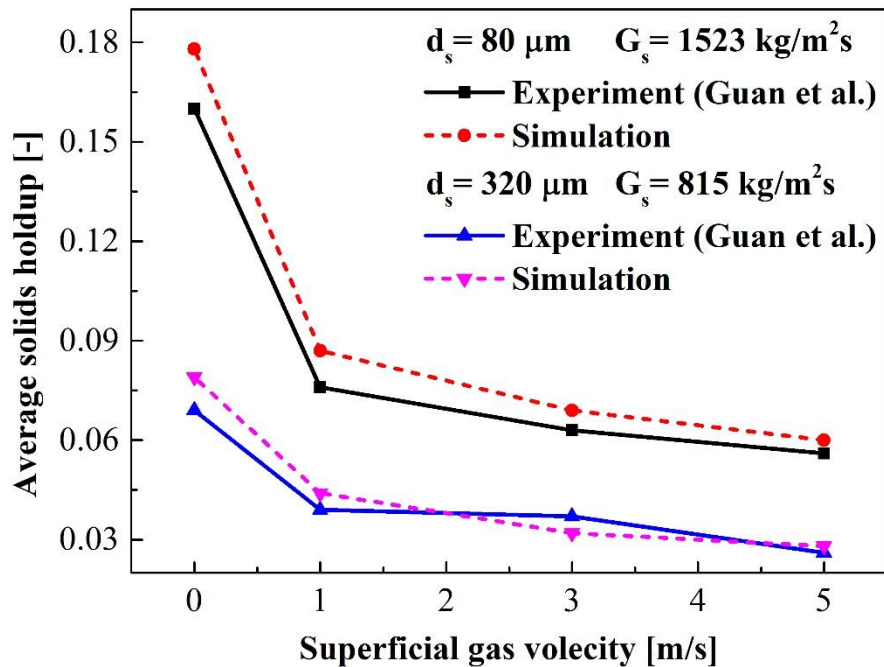


**Fig. 3-2.** Comparisons between model predictions and available data from Guan *et al.*

[38].



### 3.2.3 Simulation conditions

Computational Fluid Dynamics commercial software FLUENT 19.0 was used to implement the Eulerian-Eulerian model. Herein, the phase coupled SIMPLE algorithm was adopted to achieve pressure and velocity coupling, and the second-order upwind scheme was applied to discretize the governing equations. Velocity-inlet and pressure-outlet boundary condition were applied at inlet and outlet of the downer, respectively. In addition, no-slip boundary condition of wall was applied for air. The detailed simulation conditions and geometrical dimensions are shown in **Table 3-1**.

**Table 3-1** Simulation parameters

Description	Value
Solids mass flux ( $G_s$ )	212.2-1167.1 kg/m <sup>2</sup> s
Particles density	2560 kg/m <sup>3</sup>
Particles diameter	116 $\mu$ m
Gas density	1.225kg/m <sup>3</sup>
Gas viscosity	1.7894 $\times 10^{-5}$ kg/m $\cdot$ s
Diameter of dense downer ( $D$ )	25-35 mm
Cone angle ( $\alpha$ )	30-75 $^\circ$
Superficial gas velocity	1 m/s
Wall boundary conditions	No-slip for air, specular coefficient 0.001 for solids
Packing limit	0.63
Granular viscosity	Gidspow [27]
Granular bulk viscosity	Lun <i>et al.</i> [28]

Frictional viscosity	Schaeffer [34]
Angle of internal friction	30°
Granular temperature	Algebraic
Drag force	Gidspow [27]
Coefficient of restitution for particle-particle collisions	0.95
Gravitational acceleration	9.81 m/s <sup>2</sup>
Time steps	1×10 <sup>-5</sup> s
Convergence criteria	10 <sup>-3</sup>

---

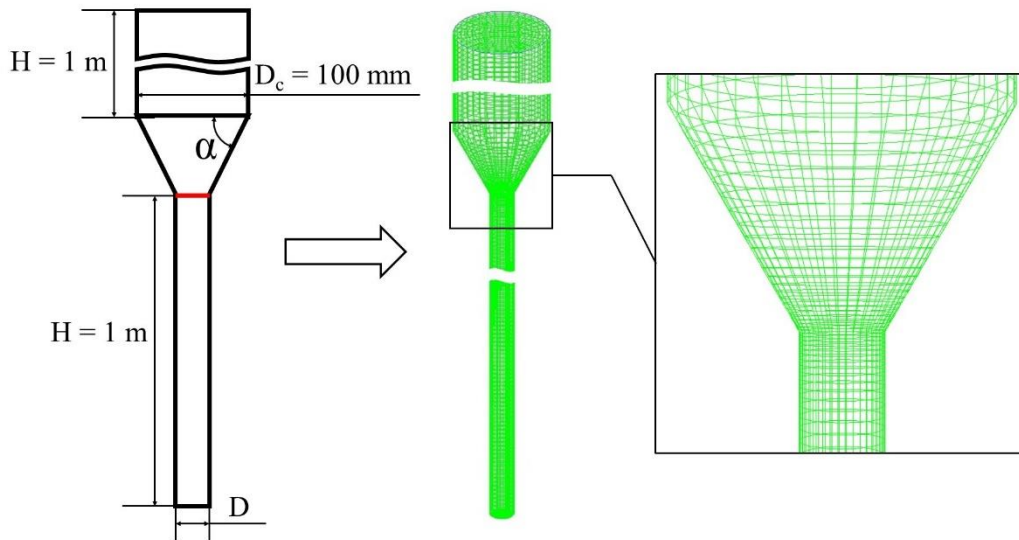


**Fig. 3-3.** Geometry and dimensions of dense downer in the simulation.

Fig. 3-3 shows the dense downer geometry and dimensions which were used to simulate gas-solids flow behavior. The unstructured mesh was applied in the numerical simulations. It is well known that the flow behavior is relatively complex at the position

of diameter changing in a long straight pipe. In order to improve accuracy, the meshes of cone structure were arranged more intensively than other positions (Fig. 3-3). Moreover, grid independence was tested to avoid the negative impacts of grid number and size on accuracy. The simulations were carried out with six grid dimensions (grid numbers: 58608, 76752, 97740, 121716, 148824, 179208). As shown in Fig. 3-4, the increase of grids caused a simulated average solids holdup decrease of about 0.007. It should be noticed that the results were almost identical when the grids were more than  $1.2 \times 10^5$ , indicating that these results of simulations were independent on the grid size. Therefore, considering both of accuracy and the workload, the  $1.2 \times 10^5$  grids condition was used in this study.

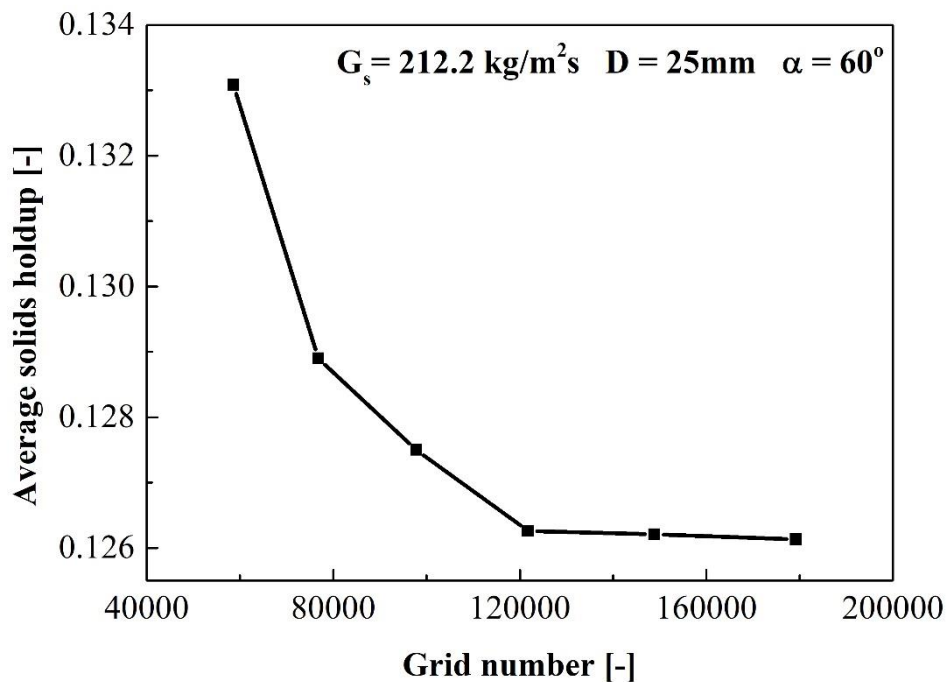


**Fig. 3-4.** Grid sensitivity analysis.

### 3.3 Results and discussion

#### 3.3.1 Effect of the diameter of dense downer

As shown in Fig. 3-5, the dense downer can increase the solids holdup extremely. When the solids mass flux ( $G_s$ ) was  $212.2 \text{ kg/m}^2\text{s}$ , the solids holdup was only about 0.02 in the dilute downer. However, in the conditions with the same solids mass flux, when the cone angle ( $\alpha$ ) was  $60^\circ$  and the diameter of dense downer ( $D$ ) were 25, 30 and 35 mm, the solids holdups in the dense downer reached 0.126, 0.108 and 0.100, respectively. In addition to the diameter, residence time is also an important point to evaluate the performance of dense downer. The residence time can be calculated by Eq. (3-23). With the decrease in  $D$ , the solids holdup increased, but the residence time decreased, and at  $D = 25 \text{ mm}$ , the residence time was only 0.079 s in the 1 m length of the dense downer.

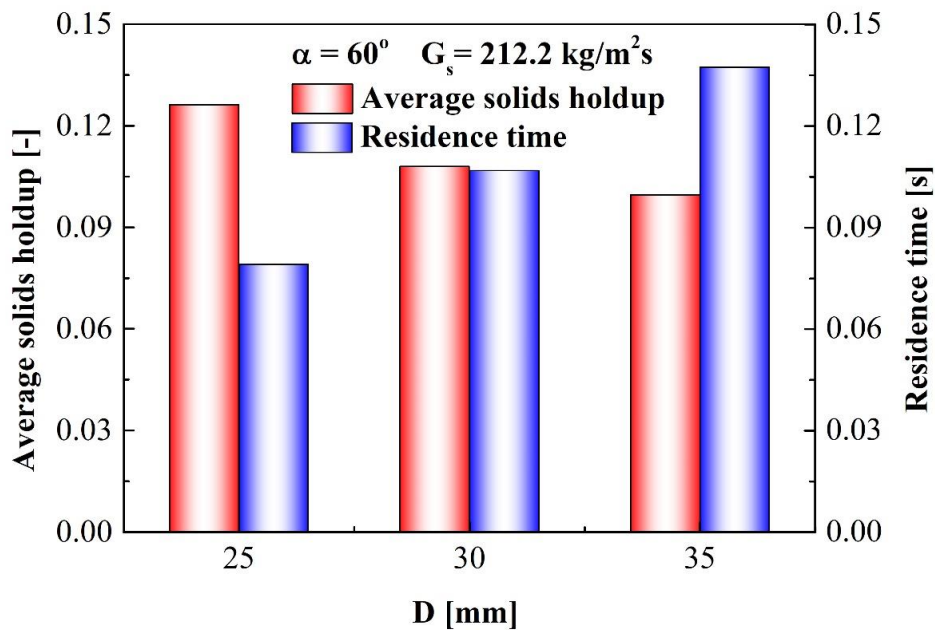
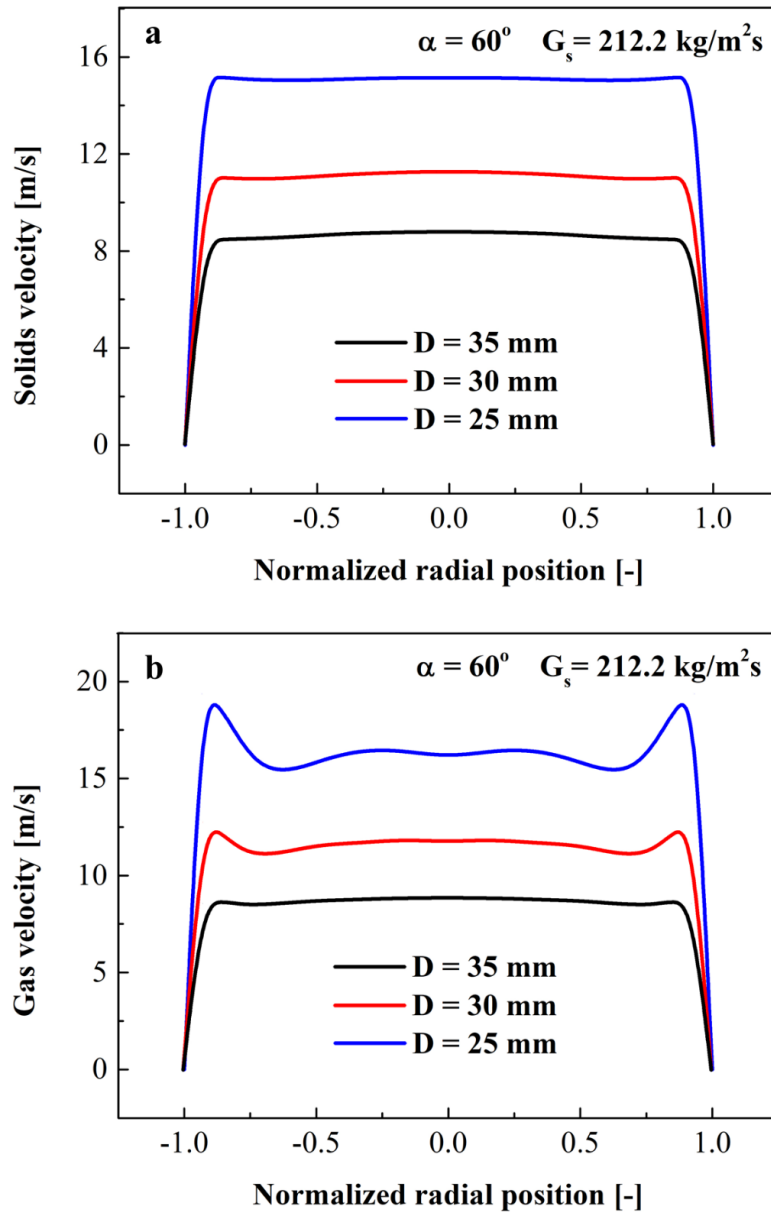


Fig. 3-5. Average solids holdup and residence time with different  $D$ .

$$t_{s,r} = \frac{H}{v_{s,ave}}. \quad (3-23)$$

Fig. 3-6 shows the radial distributions of solids and gas velocities in the dense downer. One can see that the radial distributions of solids and gas velocities were relatively uniform, and the difference occurred only at the annular region due to the wall effect. It identified that the flow behavior of this dense downer was approximately a plug flow, in which the residence time decreased with the increase in the solids and gas velocities. Moreover, the solids and gas velocities were greatly affected by the diameter of the dense downer (Fig. 3-6). According to the continuous medium hypothesis, the gas velocity should be increased with the decrease of the flow area. The smaller diameter of the dense downer is, the more particles in the cross section of the downer, resulting in the further decrease of the flow area. Therefore, with the decrease in the diameter of the dense downer the gas velocity and slip velocity increased, resulting in the increase of solids velocity. Herein, the high velocities of solids and gas could lead to the turbulence, enhancing heat and mass transfer in the reactor, which will be benefit for the pyrolysis of coal and decomposition of tar. However, in the case of  $G_s = 212.2 \text{ kg/m}^2\text{s}$ , if the diameter of the dense downer is less than 25 mm, the residence time could be not enough for the reaction and meanwhile, the wall effect on the flows of solids and gas will be obvious. Thus, considering both the residence time, solids holdup and the wall effect, in this study, the diameter of dense downer ( $D$ ) was selected at 25 mm.



**Fig. 3-6.** Radial distributions with different  $D$  at the outlet of dense downer: (a) solids velocity and (b) gas velocity.

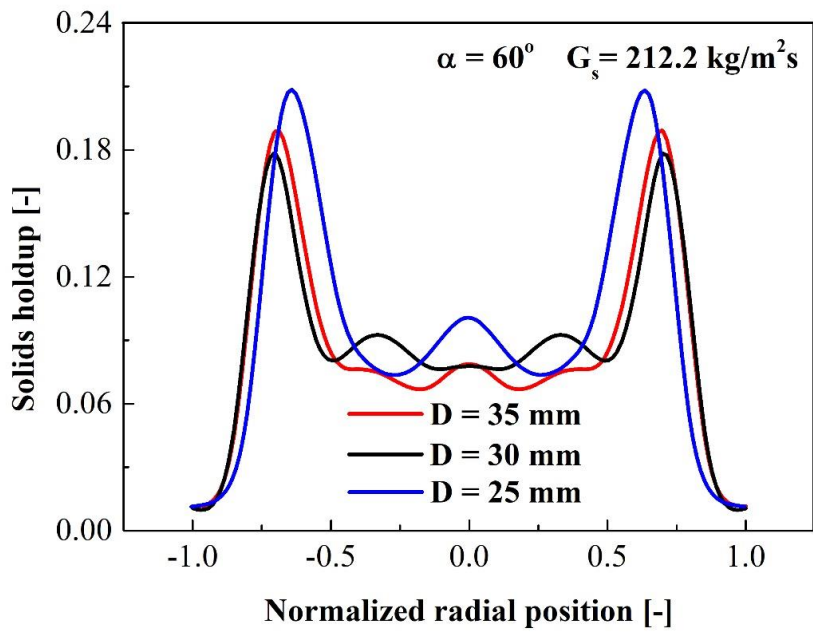


Fig. 3-7. Radial distributions of solids holdups at the outlets of dense downers with different  $D$ .

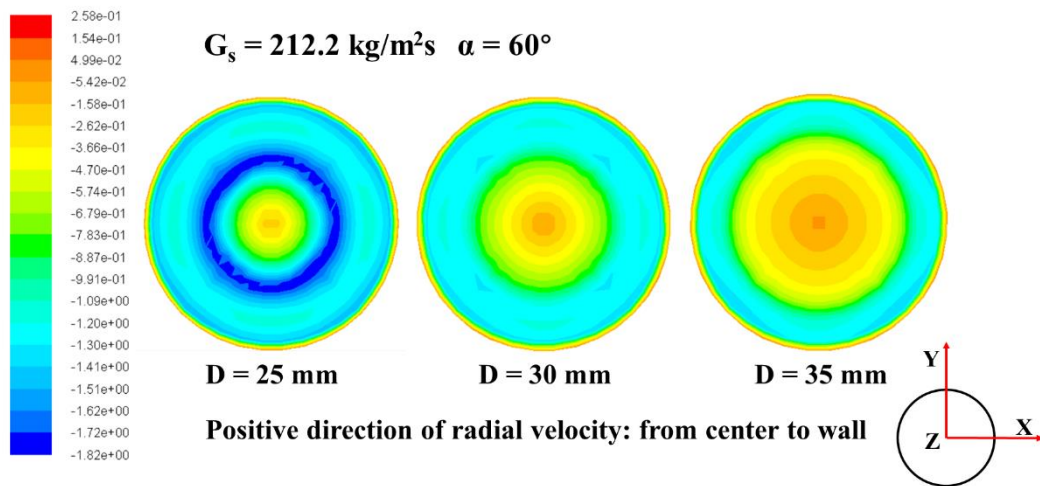
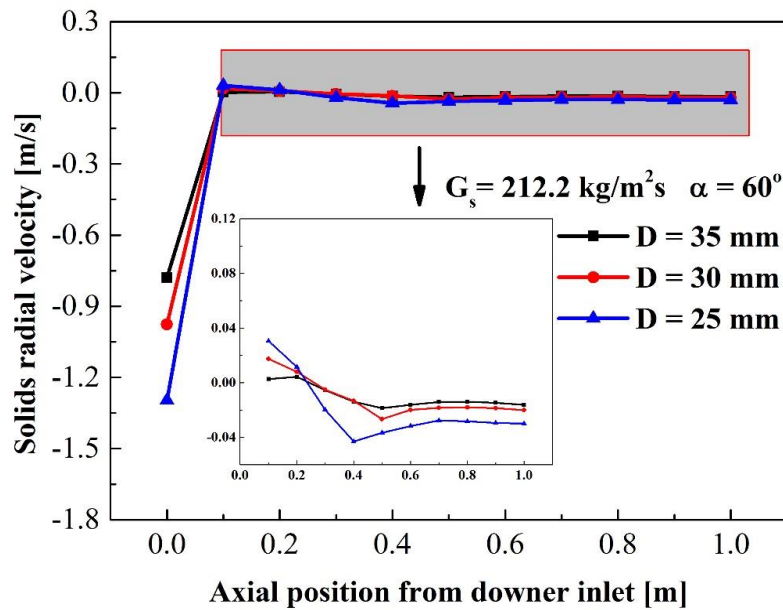


Fig. 3-8. Solids radial velocity distributions at the inlets of dense downers with different  $D$ .



**Fig. 3-9.** Axial distributions of solids radial velocity along the dense downers with different  $D$ .

In the radial solids holdup distributions at the outlets of the dense downers with different  $D$ , a peak solids holdup in the annular region near the wall appeared whereas many particles concentrated at the center (Fig. 3-7). In the conventional downer, the dense ring formed near the wall is usually considered to be resulted from the fact that the acceleration velocity of particles in the central region is faster than that of particles near the wall [40]. In contrast, in the dense downer here, besides this reason, the radial movement of particles from the center to wall caused the solids holdup maldistribution so that the dense ring was formed near the wall. Fig. 3-8 shows the radial velocity distribution by contour images at the inlet of dense downer (marked by a red line in Fig. 3-3), where the direction from the center to wall is taken as the positive direction of radial velocity. Since the cone structure before the inlet of the dense downer made the particles move radially to the wall, the smaller  $D$  led higher solids radial velocity. Also,



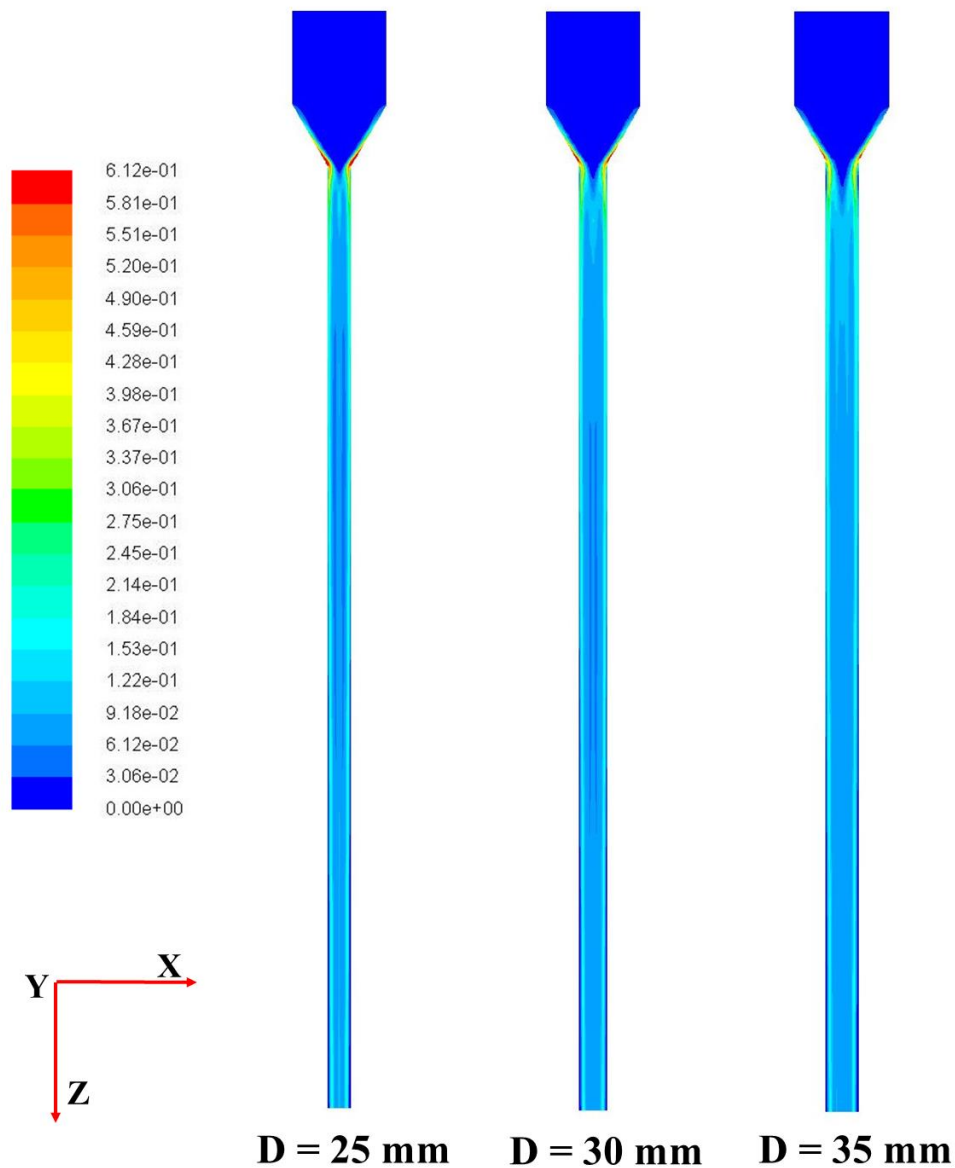


**Fig. 3-10.** Contours of solids holdup distributions of dense downer.

it can be observed that there was a radial velocity gradient of solids, which would cause intense particles collisions in the dense downer. In other words, at the inlet of dense downer, the particles concentrated in the central region and collide with each other. The collisions changed the direction of particle radial velocity and made them move towards the wall. Meanwhile, the particles reached the wall were bounced back and collided with subsequent coming particles. Therefore, a dense ring is formed in the annular

region. Fig. 3-9 shows the average solids radial velocity of horizontal cross-section along the dense downers with different  $D$  and Fig. 3-10 shows the solids holdup distribution by contour images. One can see that the average solids radial velocity almost became to a constant value after a short moving distance from the inlet, indicating that the solids flow along the dense downer was relatively stable and the particles moved towards center slowly except for the entrance area. This is the reason why the positions of dense ring in the dense downer ( $r/R = 0.65-0.75$ ) are closer to the center than the conventional downer ( $r/R = 0.85-0.95$ ).

### 3.3.2 Effect of the cone angle

Fig. 3-11 shows the effects of cone angle shown in Fig. 3-3 on the average solids holdup, average solids velocity and average gas velocity in the dense downer. One can see that the average solids holdup, average solids velocity and average gas velocity in the dense downer maintained almost unchanged with the change of the cone angle in either lower solids mass flux ( $G_s = 212.2 \text{ kg/m}^2\text{s}$ ) or high solids mass flux ( $G_s = 636.6 \text{ kg/m}^2\text{s}$ ). However, as shown in Fig. 3-12, in the radial distribution of solids holdup, with the decrease in the cone angle, the solids holdup in the central region decreased whereas the solids holdup near the wall increased, indicating more particles moved to the annular region from the center. Fig. 3-13 shows the average solids radial velocity of horizontal cross-section along the dense downers with different cone structures above them. Herein, the direction from the center to wall is taken as the positive direction of velocity. With the decrease in cone angle, the solids radial velocity increased, indicating that the cone structure with a smaller cone angle could result in more particles concentrating on the annular region.

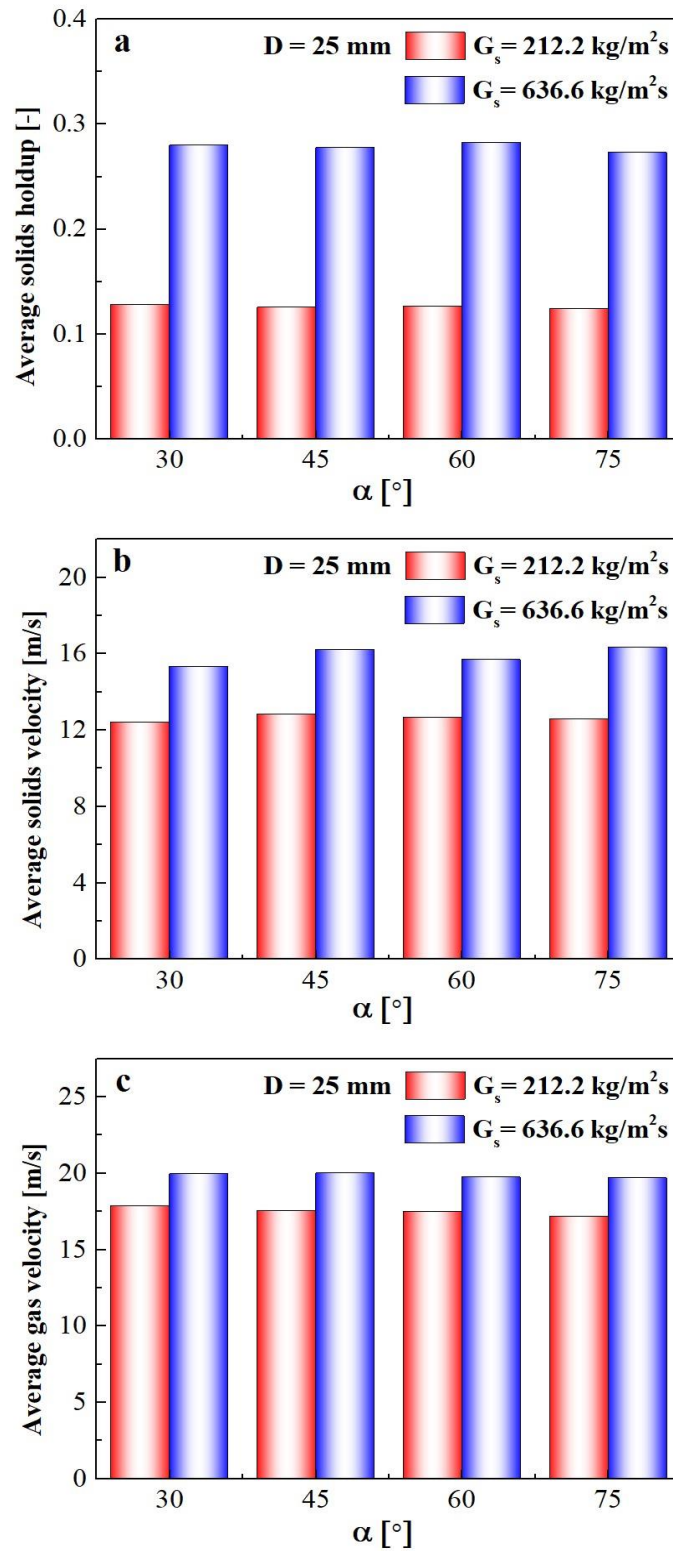


**Fig. 3-11.** Effect of cone angle on: (a) average solids holdup, (b) average solids velocity and (c) average gas velocity.

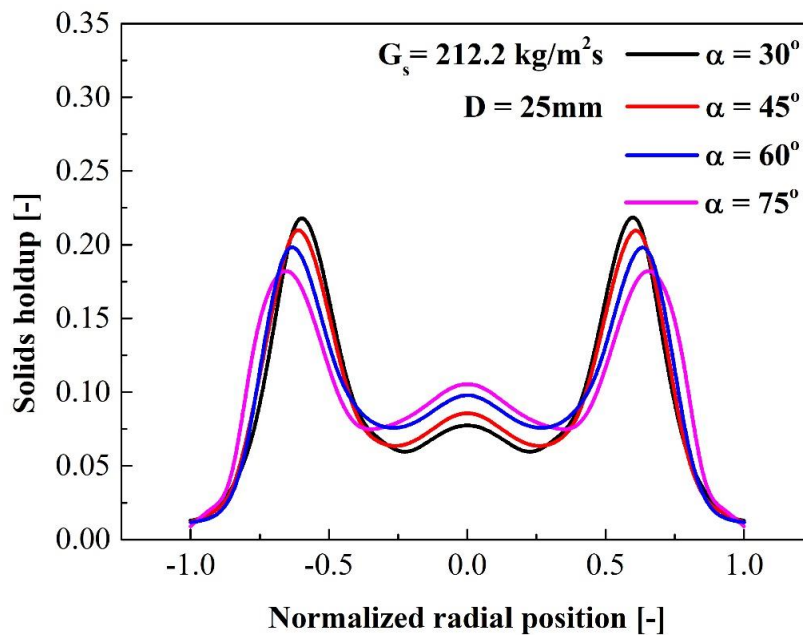


**Fig. 3-12.** Radial distributions of solids holdups at outlets of dense downers with different cone angles.

In general, a large number of agglomerates could appear inevitably with the increasing of solids holdup in a fluidized bed, and hinder the interaction of gas-solids, reducing the heat and mass transfers between gas and solids. In contrast, the agglomerates formation becomes difficult in the conventional dilute downer because the dilute gas-solids flow is along the gravitation and particles are more uniform distributed [39]. However, in the dense downer, the axial downward movement and radial movement of particles exist, and the radial movement could make particles collide with each other, but the violent collision and turbulence could hinder the formation of the agglomerates. Thus, as stated above, since the smaller cone angle resulted in the increasing of the solids radial velocity, the agglomerates could be more difficult to be formed, which will be benefit for the mass and heat transfer in the dense downer. In

addition, the high solids velocity (Fig. 3-11b) and gas velocity (Fig. 3-11c) could also improve turbulence to break up agglomerates in the dense downer with a smaller cone angle above it. However, the cone angle could not be decreased without limitation. When the cone angle is less than the angle of repose of silica sand ( $30^\circ$ ), the solids will not move into the dense downer. Therefore, considering the excellent radial mixing and the smooth operation of equipment,  $\alpha = 30^\circ$  was selected as the best parameter for cone structure in this study.

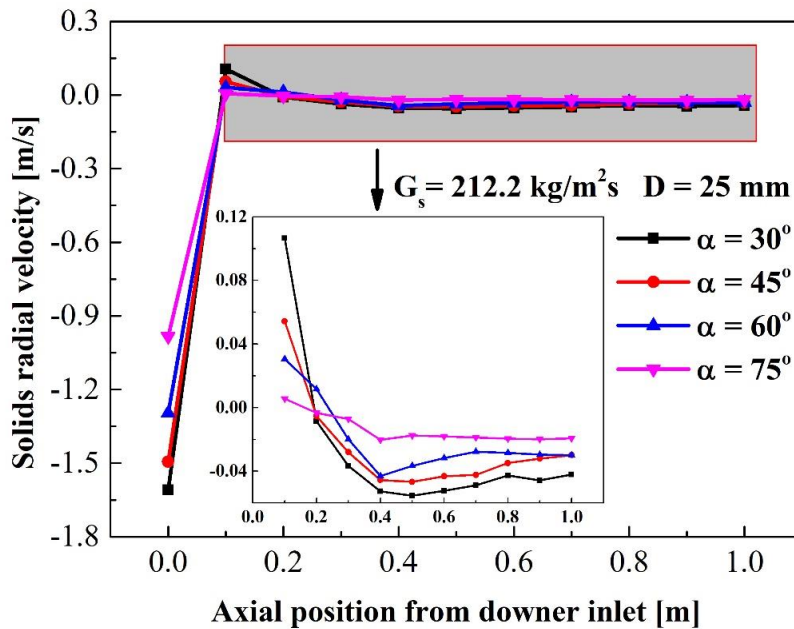


**Fig. 3-13.** Axial distributions of solids radial velocities at outlets of dense downers with different cone angles.

### 3.3.3 Effect of solids mass flux

To obtain the utmost limit of solids holdup in such a dense downer, the relationship of the solids holdup and the solids mass flux was investigated in a dense downer with a diameter of 25 mm. As shown in Fig. 3-14, the solids holdup increased linearly with the

increase in  $G_s$ , and the highest average solids holdup reached about 0.39. However, when the  $G_s$  exceeded 956.9  $\text{kg/m}^2\text{s}$ , the average solids holdup remained almost unchanged at 0.4 instead of a linear rise. Herein, the solids mass flow flux at  $G_s = 1061$  and  $1167.1 \text{ kg/m}^2\text{s}$  were further investigated. The differences of solids mass flow rates between inlet and outlet were  $0.42 \text{ kg/s}$  and  $1.12 \text{ kg/s}$ , respectively. In this case, some particles would be accumulated in the cone structure and dilute downer. In other words, the mass conservation has been broken. The phenomenon indicates that the carrying capacity of dense downer reaches the maximum. According to these results, the  $G_s$  should be limited to less than  $956.9 \text{ kg/m}^2\text{s}$ .

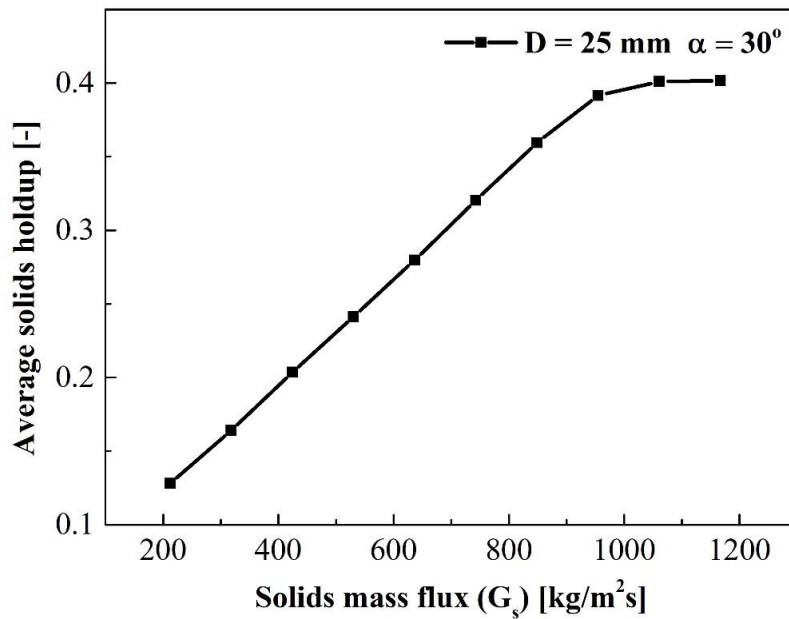


**Fig. 3-14.** Effects of  $G_s$  on average solids holdup.

Fig. 3-15 shows the effects of  $G_s$  on the radial distribution of solids holdup. When the  $G_s$  was less than  $636.6 \text{ kg/m}^2\text{s}$ , the solids holdup increased at all radial positions with the increase in  $G_s$ . When the  $G_s$  was over  $636.6 \text{ kg/m}^2\text{s}$ , the maximum solids

holdup remained unchanged at about 0.52 in the annular region and exhibited an accelerating rise in the central region. As discussed above, the particles will move towards the wall after the collision at the inlet region. In the case of high  $G_s$ , because the solids holdup in annular region reached the saturation state, the particles in the central region cannot move to the wall, leading to an accelerated rise of solids holdup in the center region. When the  $G_s$  was less than  $636.6 \text{ kg/m}^2\text{s}$ , the gas flow resistance in the central region should be low due to the low solids holdup so that the gas tends to flow into the central region, which could cause a separation of gas and solids phases. Thusly, the gas and solids should contact more sufficiently in the case of high  $G_s$ .

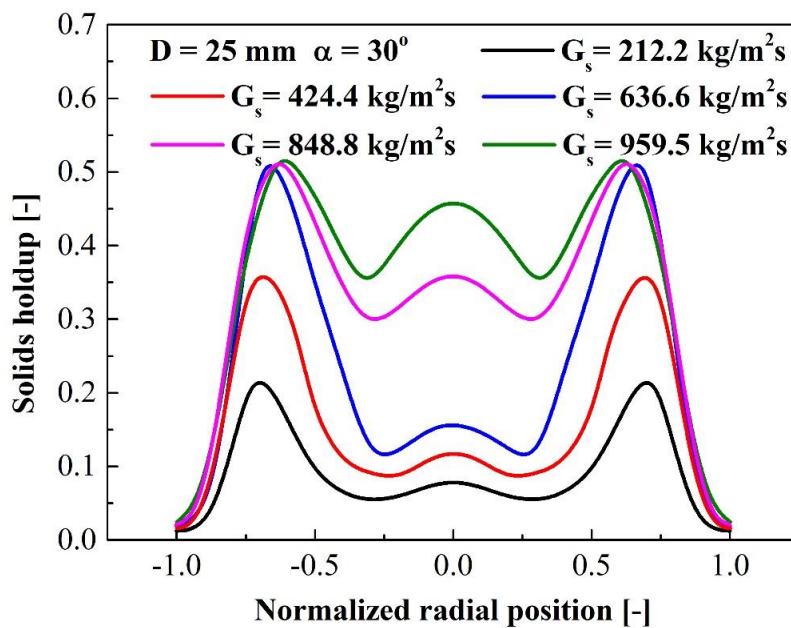


**Fig. 3-15.** Radial distribution of solids holdup with different  $G_s$  at outlet of dense downer.

Moreover, when the solids and gas get into the dense downer from the cone structure, according to the continuous medium hypothesis, the gas velocity will increase

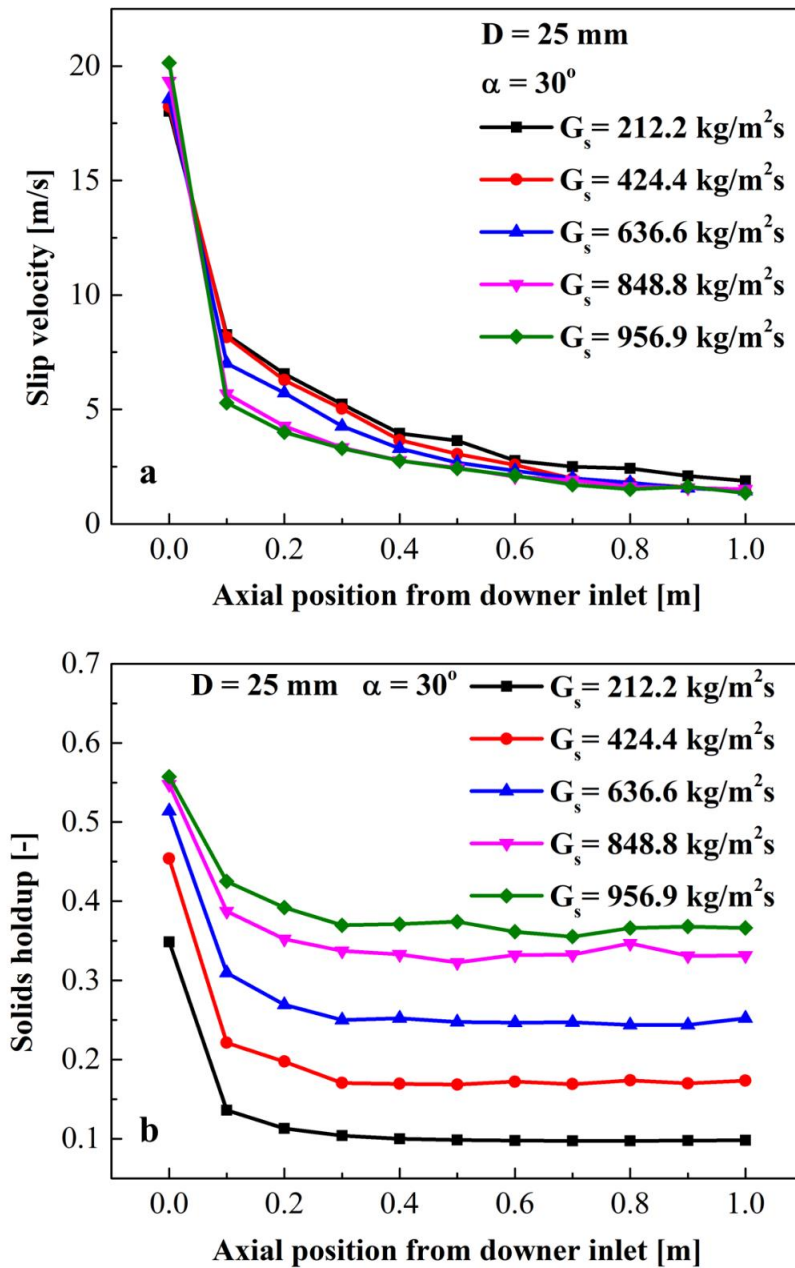


**Fig. 3-16** Axial distribution with different  $G_s$ : (a) slip velocity, and (b) solids holdup.

rapidly, causing a high slip velocity at the inlet of dense downer (Fig. 3-16a). In this case, the particles will be rapidly accelerated downward in the dense downer under the combined action of gas-solids drag force and gravity, and as such, the slip velocity will



decrease along the dense downer. As shown in Fig. 3-16a, the solids velocity did not exceed the gas velocity so that the kinetic energy is continuously transferred from the gas to the solids. Fig. 3-16b shows the effect of  $G_s$  on the solids holdup axial distribution. With the increase in  $G_s$ , the solids holdup increased at each axial position along the dense downer. It should be noted that the solids holdup decreased rapidly at the inlet of dense downer owing to the particles accelerating. Moreover, the axial distribution of solids holdup appeared an exponential form, indicating that the gas-solids flow developed rapidly in the accelerating stage. As such, the solids holdup became almost a constant below the position of  $Z = 0.4$  m. Herein, one can see that the axial flow characteristics in the dense downer was the similar as that in the first acceleration region and the developed region of the conventional downer. However, the second acceleration region was not observed due to the short length of the downer in this study.

### 3.4. Conclusions

In this study, the gas-solids flow behaviors of a dense downer setting under a dilute conventional downer were simulated. In order to obtain the optimal structural parameters and operating conditions, the influences of  $D$ ,  $\alpha$  and  $G_s$  on the solids holdup were investigated in details. The results of simulation on the dense downer in the cold state are as follows:

(1) The novel dense downer could increase solids holdup extremely. It is found that there is a peak solids holdup in the annular region near the wall whereas many particles concentrate at the center of the dense downer. The unique solids radial distribution is

caused by the radial movement of particles.

(2) With the decrease in  $D$ , the solids holdup and the velocities of gas and solids increase, but the residence time decreases. Considering enough residence time and solids holdup and avoiding the wall effect, the optimum diameter of dense downer ( $D$ ) should be 25 mm.

(3) The cone structure with small  $\alpha$  pushes more particles towards the annular region and inhibits the agglomerates by collisions, which could enhance the radial mixing, and the heat and mass transfers. Because the  $\alpha$  should not be less than the angle of repose of the solids,  $\alpha = 30^\circ$  is selected the optimum parameter for the cone structure.

(4) It is found that the utmost limit of the average solids holdup is about 0.4, and in this case, the carrying capacity of dense downer reaches the maximum, and the peak solids holdup of annular region is about 0.52. In addition, it is found that the axial flow characteristic in the dense downer the similar as that in the first acceleration and developed regions of the conventional downer.

## Nomenclature

### *Notations*

$c_v$	coefficient of variation
$C_D$	drag coefficient, dimensionless
$C_\mu, C_{1\varepsilon}, C_{2\varepsilon}$	coefficients in turbulence model, dimensionless
$d_s$	particle diameter, m
$D$	diameter of dense downer, m
$e_s$	particle-particle restitution coefficient, dimensionless

$e_w$	particle-wall restitution coefficient, dimensionless
$g$	gravitational acceleration, $\text{m/s}^2$
$g_0$	radial distribution coefficient, dimensionless
$G_{k, m}$	production of turbulent kinetic energy, dimensionless
$G_s$	circulating flux of solid particles, $\text{kg/m}^2\text{s}$
$H$	height of the dense downer, m
$\bar{I}$	stress tensor, dimensionless
$I_{2D}$	second invariant of the deviatoric stress tensor, dimensionless
$k$	turbulence kinetic energy tensor, dimensionless
$k_{\Theta_s}$	diffusion coefficient for granular energy, $\text{kg/s}\cdot\text{m}$
$K_{gs}$	interphase exchange coefficient, $\text{kg}\cdot\text{m}^2/\text{s}$
$n$	sample size of radial distribution of solids holdup
$p$	pressure, Pa
$p_s$	particulate phase pressure, Pa
$p_f$	pressure for wall friction, Pa
$r$	Radial distance, m
$R$	radius of the downer, m
$Re$	relative Reynolds number, dimensionless
$Re_s$	particle Reynolds number, dimensionless
$t$	time, s
$t_{s,r}$	residence time, s
$v_g$	gas velocity, $\text{m/s}$
$v_s$	solids velocity, $\text{m/s}$

$v_{s,ave}$	average solids velocity, m/s
$z$	height of the measured section, m
$Z$	axial distance from the inlet of dense downer, m

***Greek letters***

$\alpha$	angle of cone structure, degrees
$\alpha_g$	volume fraction of gas phase, dimensionless
$\alpha_s$	volume fraction of solids phase, dimensionless
$\alpha_{s,ave}$	average volume fraction of solids phase, dimensionless
$\varepsilon$	turbulence dissipation rate, $m^2/s^3$
$\varphi_{gs}$	dissipation of granular energy resulting from the fluctuating forcer, $m^2/s^2$
$\mu_g$	viscosity of gas phase, Pa·s
$\mu_s$	solids shear viscosity, Pa·s
$\mu_{s,col}$	solids collisional viscosity, Pa·s
$\mu_{s,kin}$	solids kinetic viscosity, Pa·s
$\mu_{s,fr}$	solids frictional viscosity, Pa·s
$\mu_{t,m}$	frictional viscosity of system m, Pa·s
$\Pi_{kg}$	source term caused by influence of solids phase on turbulent kinetic energy, $m^2/s^3$
$\Pi_{\varepsilon g}$	source term caused by influence of solids phase on turbulence energy dissipation rate, $m^2/s^4$
$\sigma_\varepsilon$	granular kinetic theory parameter (kinetic viscosity), Pa·s
$\sigma(\alpha_s)$	standard deviation of volume fraction of solids phase, dimensionless
$\theta$	angle of internal friction, degrees

$\theta_s$	granular temperature, $m^2/s^2$
$\gamma_{\theta_s}$	collisional dissipation of energy, $m^2/s^2$
$\overline{\tau}_g$	shear stress of gas phase, $N/m^2$
$\overline{\tau}_s$	shear stress of solids phase, $N/m^2$
$\lambda_s$	solids bulk viscosity, $Pa \cdot s$
$\rho_g$	gas density, $kg/m^3$
$\rho_s$	solids density, $kg/m^3$

## References

- [1] IEA, World Energy Outlook 2020, <https://www.iea.org/reports/world-energy-outlook-2020#>; 2020 [accessed in 12 Jun 2020]
- [2] Bayarsaikhan B, Sonoyama N, Hosokai S, Shimada T, Hayashi J-i, Li C-Z, et al. Inhibition of steam gasification of char by volatiles in a fluidized bed under continuous feeding of a brown coal. *Fuel* 2006;85:340-9.
- [3] Tsutsumi A. Advanced IGCC/IGFC using exergy recuperation technology. *Clean Coal Technol J* 2004;11:17-22.
- [4] Guan G, Fushimi C, Tsutsumi A, Ishizuka M, Matsuda S, Hatano H, et al. High-density circulating fluidized bed gasifier for advanced IGCC/IGFC—Advantages and challenges. *Particuology* 2010;8:602-6.
- [5] Kawabata M, Kurata O, Iki N, Tsutsumi A, Furutani H. System modeling of exergy recuperated IGCC system with pre- and post-combustion CO<sub>2</sub> capture. *Appl Therm Eng* 2013;54:310-8.
- [6] Kawabata M, Kurata O, Iki N, Tsutsumi A. Advanced integrated gasification

combined cycle (A-IGCC) by exergy recuperation--technical challenges for future generations. *J Chem Eng Jpn* 2012;92.

[7] Kuchonthara P, Bhattacharya S, Tsutsumi A. Combination of thermochemical recuperative coal gasification cycle and fuel cell for power generation. *Fuel* 2005;84:1019-21.

[8] Cheng Y, Guan G, Ishizuka M, Fushimi C, Tsutsumi A, Wang C-H. Numerical simulations and experiments on heat transfer around a probe in the downer reactor for coal gasification. *Powder Technol* 2013;235:359-67.

[9] Guan G, Fushimi C, Ishizuka M, Nakamura Y, Tsutsumi A, Matsuda S, et al. Flow behaviors in the downer of a large-scale triple-bed combined circulating fluidized bed system with high solids mass fluxes. *Chem Eng Sci* 2011;66:4212-20.

[10] Yoshie Y, Ishizuka M, Guan G, Fushimi C, Tsutsumi A. A novel experimental technique to determine the heat transfer coefficient between the bed and particles in a downer. *Adv Powder Technol* 2013;24:487-94.

[11] Fushimi C, Guan G, Nakamura Y, Ishizuka M, Tsutsumi A, Suzuki Y, et al. Mixing behaviors of cold-hot particles in the downer of a triple-bed combined circulating fluidized bed. *Powder Technol* 2012;221:70-9.

[12] Fushimi C, Ishizuka M, Guan G, Suzuki Y, Norinaga K, Hayashi J-i, et al. Hydrodynamic behavior of binary mixture of solids in a triple-bed combined circulating fluidized bed with high mass flux. *Adv Powder Technol* 2014;25:379-88.

[13] Fushimi C, Guan G, Nakamura Y, Ishizuka M, Tsutsumi A, Matsuda S, et al. Hydrodynamic characteristics of a large-scale triple-bed combined circulating fluidized bed. *Powder Technol* 2011;209:1-8.

[14] Hoya R, Fushimi C. Thermal efficiency of advanced integrated coal gasification

combined cycle power generation systems with low-temperature gasifier, gas cleaning and CO<sub>2</sub> capturing units. *Fuel Process Technol* 2017;164:80-91.

[15] Lian W, Yang J, Li P, Wang J, Zhang Z, Fushimi C, et al. Numerical simulation of hydrodynamic behaviors in a novel gas-solids conical downer. *Powder Technol* 2018;336:573-83.

[16] Lv P, Chang J, Xiong Z, Huang H, Wu C, Chen Y, et al. Biomass air– steam gasification in a fluidized bed to produce hydrogen-rich gas. *Energy Fuels* 2003;17:677-82.

[17] Zhao Z, Yang J, Zhang W, Li P, Lian W, Zhang Z, et al. Hydrodynamic simulation and optimization of the feeding system of a bubbling fluidized-bed gasifier in a triple-bed circulating fluidized bed with high solids flux. *Powder Technol* 2017;321:336-46.

[18] Cheng Y, Lim EWC, Wang C-H, Guan G, Fushimi C, Ishizuka M, et al. Electrostatic characteristics in a large-scale triple-bed circulating fluidized bed system for coal gasification. *Chem Eng Sci* 2012;75:435-44.

[19] Cheng Y, Zhang W, Guan G, Fushimi C, Tsutsumi A, Wang C-H. Numerical studies of solid–solid mixing behaviors in a downer reactor for coal pyrolysis. *Powder Technol* 2014;253:722-32.

[20] Cheng Y, Lau DYJ, Guan G, Fushimi C, Tsutsumi A, Wang C-H. Experimental and numerical investigations on the electrostatics generation and transport in the downer reactor of a triple-bed combined circulating fluidized bed. *Ind Eng Chem Res* 2012;51:14258-67.

[21] Zhang W, Cheng Y, Wang C, Yang W, Wang C-H. Investigation on hydrodynamics of triple-bed combined circulating fluidized bed using electrostatic sensor and electrical capacitance tomography. *Ind Eng Chem Res* 2013;52:11198-207.

- [22] Hayashi J-I, Hosokai S, Sonoyama N. Gasification of low-rank solid fuels with thermochemical energy recuperation for hydrogen production and power generation. *Process Saf Environ Prot* 2006;84:409-19.
- [23] Fushimi C, Okuyama S, Kobayashi M, Koyama M, Tanimura H, Fukushima H, et al. Pyrolysis of low-rank coal with heat-carrying particles in a downer reactor. *Fuel Process Technol* 2017;167:136-45.
- [24] Shu Z, Fan C, Li S, Wang J. Multifluid modeling of coal pyrolysis in a downer reactor. *Ind Eng Chem Res* 2016;55:2634-45.
- [25] Chen X-Z, Shi D-P, Gao X, Luo Z-H. A fundamental CFD study of the gas–solid flow field in fluidized bed polymerization reactors. *Powder Technol* 2011;205:276-88.
- [26] Peng G, Dong P, Li Z, Wang J, Lin W. Eulerian simulation of gas–solid flow in a countercurrent downer. *Chem Eng J* 2013;230:406-14.
- [27] Ding J, Gidaspow D. A bubbling fluidization model using kinetic theory of granular flow. *AIChE J* 1990;36:523-38.
- [28] Lun C, Savage SB, Jeffrey D, Chepurniy N. Kinetic theories for granular flow: inelastic particles in Couette flow and slightly inelastic particles in a general flowfield. *J Fluid Mech* 1984;140:223-56.
- [29] Syamlal M, Rogers W, OBrien TJ. MFIX documentation theory guide. USDOE Morgantown Energy Technology Center, WV (United States); 1993.
- [30] Chapman S, Cowling TG, Burnett D. The mathematical theory of non-uniform gases: an account of the kinetic theory of viscosity, thermal conduction and diffusion in gases. Cambridge: Cambridge university press; 1990.
- [31] Geldart D. Gas fluidization technology. United States 1986.
- [32] Shi D-P, Luo Z-H, Zheng Z-W. Numerical simulation of liquid–solid two-phase



- flow in a tubular loop polymerization reactor. *Powder Technol* 2010;198:135-43.
- [33] Gidaspow D. *Multiphase flow and fluidization: continuum and kinetic theory descriptions*. San Diego: Academic press; 1994.
- [34] Schaeffer DG. Instability in the evolution equations describing incompressible granular flow. *J Differ Equations* 1987;66:19-50.
- [35] Bradshaw P, Cebeci T, Whitelaw JH. *Engineering calculation methods for turbulent flow*. London: Academic Press; 1981.
- [36] Chen CJ. *Fundamentals of turbulence modelling*. Florida: CRC Press; 1997.
- [37] Taghipour F, Ellis N, Wong C. Experimental and computational study of gas–solid fluidized bed hydrodynamics. *Chem Eng Sci* 2005;60:6857-67.
- [38] Guan G, Ishizuka M, Fushimi C, Suzuki Y, Tsutsumi A. Downward gas-solids flow characteristics in a high-density downer reactor. *J Chem Eng Jpn* 2012;948-54.
- [39] Jin Y, Zhu J, Wang Z, Yu Z. *Fluidization engineering principles*. Beijing: Tsinghua University Press; 2001.

## **CHAPTER 4: A Biomass-Based Small-Scale Power Generation System with Energy/Exergy Recuperation**

### **4.1 Introduction**

Nowadays, electricity accounts for 19% of total final consumption of energy [1], which is increasing year by year with the economic growth [2]. Fossil fuels are still the major energy resources for the world's electricity generation [3]. However, the fossil fuels will be not enough for world energy requirement and diminish completely in 2100s based on the current rate of energy consumption [4]. Moreover, the utilization of fossil fuels has caused global warming and environmental pollution because of the emission of greenhouse gas, acid gas and aerosol particles [5]. Therefore, it is becoming more and more important for the application of environmentally friendly natural energy to replace the traditional fossil fuels to generate electricity. Among various natural energies, biomass is considered as the renewable and sustainable one which can provide stable electricity and attracted much attention from both industrial and academic research fields [6]. Especially, the carbon dioxide produced from the utilization of biomass can be captured by afforestation, preventing the carbon dioxide from exacerbating global warming [7].

Due to the scattered geographical distribution of biomass, to reduce the costs of collection and transportation and fully use the locally available biomass, small-scale biomass power generation system should be more suitable for the biomass energy applications [8]. Nevertheless, the net biomass to electricity efficiencies of conventional

combustion-type power plants are still low, which only range from 20% to 30% (based on lower heating value (LHV)) [9]. In addition, the high specific investment cost and emissions of acid gases such as nitrogen oxides ( $\text{NO}_x$ ) and sulfur oxides ( $\text{SO}_x$ ) are also essential to be solved [10]. Thus, the biomass-based combined heat and power (CHP) systems with high thermal efficiency and excellent pollutants removing capability have become the main stream in the application of biomass energy [11]. It is reported that a CHP system consisted of solid oxide fuel cells (SOFCs) and/or gas turbine (GT) could achieve a high efficiency for the generation of electrical power [12], in which biomass should firstly react with different gasifying agents such as air, steam, oxygen, and carbon dioxide to produce syngas rich in hydrogen and carbon monoxide. Thus, how to effectively obtain high quality syngas becomes the key process for the biomass-based CHP system.

The effects of reactor type, gasifying agent and catalyst on the biomass gasification efficiency have been widely investigated. Usually, gasification is carried out in a fixed bed, a moving bed or a fluidized bed [13]. The fixed bed and moving bed are always used in small-scale biomass gasifiers since their simple structure and easy operation. However, their temperature distributions are always nonuniform and gasification efficiencies are low and especially tar is easily generated. In contrast, by using the fluidized bed, the formation of hot spots can be refrained, and simultaneously the interaction between solids and gas can be enhanced. However, a large amount of fly-ashes and tar could be also generated along with the syngas, leading to the increase of purification cost and risk of tube blockage [14].

Meanwhile, the selection of gasifying agent could greatly affect the quantity and quality of the products. When pure oxygen or air is used as the gasifying agent, partial

combustion occurs to provide heat for the gasification. In the case of using air, the produced syngas has a relatively lower heating value due to the dilution of nitrogen [15]. On the other hand, in the case of using pure oxygen, the generation of oxygen from air needs an air separation unit (ASU), which will significantly increase the cost due to the high electrical consumption. Carbon dioxide is also used as the gasifying agent, but the gasification needs high temperature and the efficiency is low [16]. In contrast, the steam gasification can be carried out at a relatively low temperature condition to obtain the syngas with high heating value [15]. However, in the steam gasification of biomass, biomass pyrolysis, volatiles reforming and bio-char gasification usually occur at different temperature ranges with different reaction rates. For example, biomass pyrolysis and tar reforming are relatively fast reaction processes whereas it has to take a long time for the complete steam gasification of bio-char at a high temperature (800-1000 °C) [17]. Due to the endothermicity and long required residence time of bio-char reaction in steam gasification process, circulating fluidized bed (CFB) systems are often adopted to subdivide the reaction process into gasification and bio-char oxidation [18]. In the conventional CFB biomass gasification system, the unreacted bio-char in gasifier flows into a combustor to provide required thermal energy for the total system by using inert heat carriers. Although this design can reduce the required residence time of biomass particles in the gasifier, how to achieve a heat balance in the system is still a difficult issue. Especially, the consumption of fuel in the combustor is commonly in the range of 30-40% of the total fuel input for the gasification system [19]. However, since the range of bio-char yield in general pyrolysis is 9.5-48% and in particular, the range of bio-char yield during the fast pyrolysis process is only 12-15% [20], obviously, the heat provided by unreacted bio-char may not be enough for the biomass pyrolysis and steam

reforming of tar and gasification of bio-char. To ensure sufficient heat with high temperature, some researchers tried to provide heat for gasification system by using heat-exchange type combustor, in which some fuels or part of syngas was combusted to provide heat for the gasification reaction [19]. Such methods can separate the gasification from combustion completely to avoid mixing combustion exhaust with produced syngas. However, the introduction of heat exchanger units into the system needs further spatial subdivisions of gasification system. In addition, the high mass fraction of volatiles during the biomass gasification could promote the coke formation on the catalyst surface, resulting in rapid catalyst deactivation [21]. Thus, considering the difference in reaction time, heat supplement and catalyst deactivation, the spatial subdivision of biomass pyrolysis, combustion, tar reforming and catalyst regeneration processes is adopted by using a separated-type biomass gasification process to realize the optimization of each conversion step and improve the whole performance.

Moreover, in the biomass-based CHP system, along with the syngas production and electrical power generation, how to recuperate and reuse the exhausting energy/exergy from the gasifier, SOFC, gas turbine and the auxiliary equipment is also very important [22]. In addition, the high-temperature crude syngas produced from the gasifier cannot be applied in SOFC and gas turbine directly due to the existence of many impurities and toxic substances in it. Since the techniques of the high-temperature separation of impurities and toxic substances are still immature, the crude syngas has to be cooled down, purified at low temperatures, compressed and reheated before entering SOFCs. As such, during the process of cooling and reheating, a large amount of energy/exergy is lost, leading to the decrease of whole thermal efficiency in the system [23]. Therefore, avoiding the energy/exergy loss as much as possible is the key to

realize high-efficiency of the biomass-based CHP system.

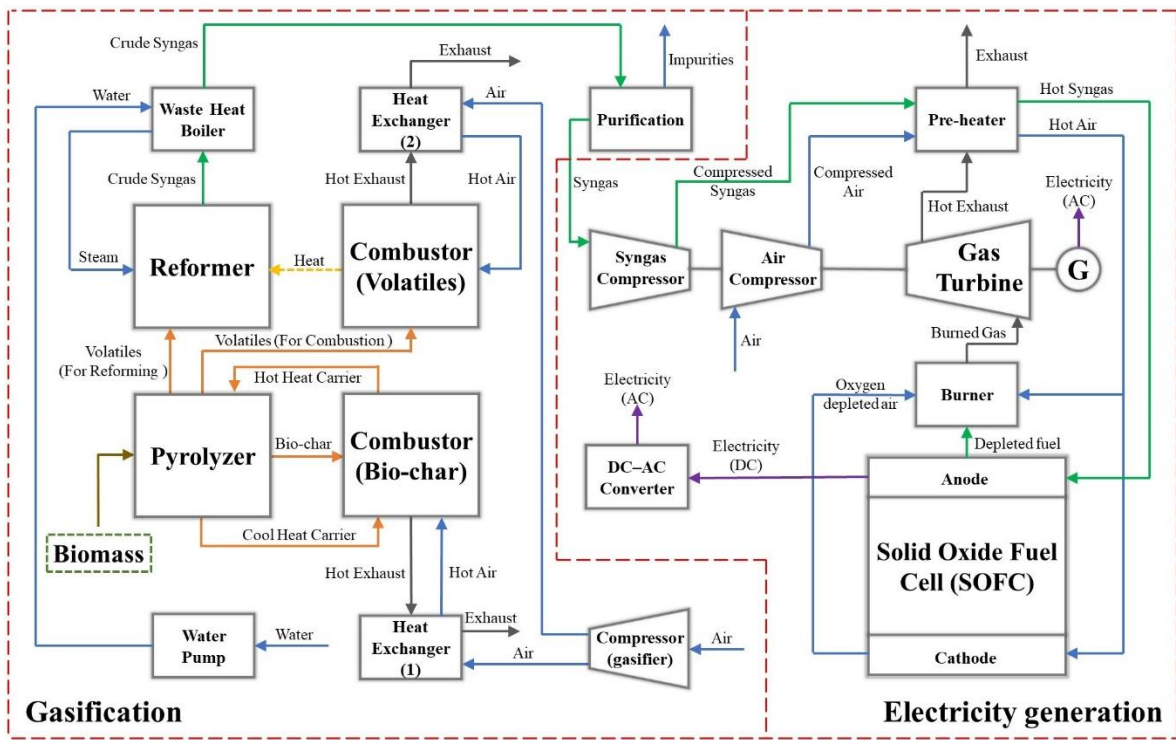


**Fig. 4-1.** Schematic of the proposed biomass-based power generation system with energy/exergy recuperation.

In this work, a novel small-scale high-efficient power generation system with a separated-type biomass gasification process and energy/exergy recuperation is proposed for the first time. As shown in the flowsheet diagram (Fig. 4-1), the system is mainly operated as follows:

- (1) Biomass is fed into the separated-type biomass gasification process and converted to crude syngas by a fast pyrolysis unit combined with a catalytic steam reforming unit for tar.
- (2) The produced crude syngas is cooled down, purified, compressed and pre-heated.
- (3) High-temperature clean syngas flows into the SOFCs to generate electrical power.
- (4) Unreacted fuel gas burns in a gas turbine to generate electrical power.

(5) Exhaust from gas turbine provides heat for pre-heating the syngas and air used in SOFCs and gas turbine.

In addition, heat is also recuperated by heat exchangers from the exhausts of bio-char and volatiles combustion and reutilized in the gasification process. It should be noted that the fast pyrolysis of biomass combined with the catalytic steam tar reforming is considered in this new system for the first time, which is expected to provide a new biomass conversion process with highly efficient utilization of biomass for the power generation.

## **4.2 System process and simulation methods**

As illustrated in Fig. 4-1, the proposed power generation system mainly includes a separated-type biomass gasification process with a pyrolyzer, a tar (volatiles) reformer, a bio-char combustor, a volatiles combustor, a syngas purifier, and an electrical power generation process with a SOFC and a gas turbine. The main auxiliary equipment includes heat exchangers, compressors, water pumps and waste heat boiler. In this work, Aspen Plus software (10.0 version) is applied for the total system analysis, and the detail model is built as illustrated in Fig. 4-2. Herein, the basic assumptions for the simulation are listed as follows:

- (1) All units are operated at steady-state conditions.
- (2) The heat loss in the gasification system by wall is assumed to be 4% of LHV of biomass [24];
- (3) All reactors reach the equilibrium states;
- (4) The standard condition (dead state) for specific enthalpy, specific entropy, standard

chemical exergy is temperature  $T_0 = 25 \text{ °C}$  and absolute pressure  $P_0 = 1 \text{ atm}$ ;

(5) All inputs of biomass, air and water are in the standard condition.

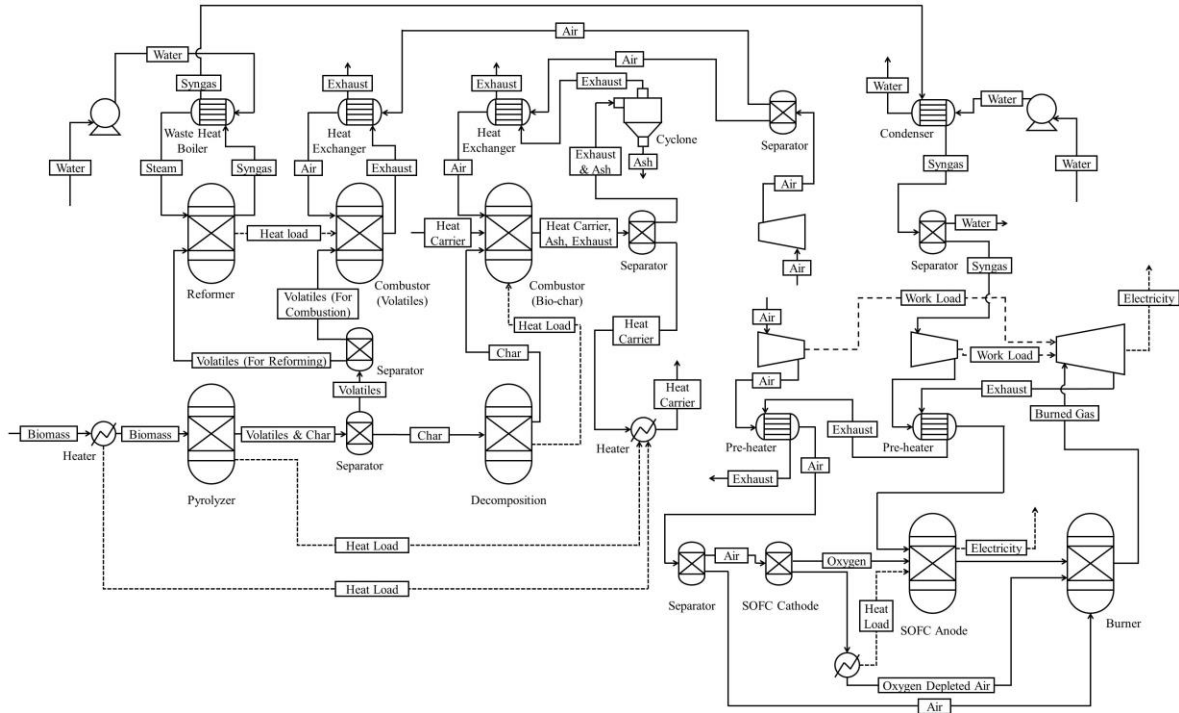


**Fig. 4-2.** Detailed flowsheet of the system in Aspen Plus software.

#### 4.2.1 The proposed separated-type biomass gasification process

Fig. 4-3 shows the schematic diagram of the proposed novel separated-type biomass gasification process in this work, in which a downer-type pyrolyzer, a riser-type combustor (bio-char) and a tube-and-shell-type tar (volatiles) reformer are included. In the simulation, wood chips are considered as the biomass feedstock, which are introduced into the downer-type pyrolyzer and heated to 500 °C by the heat carrier (e.g., silica sands) and pyrolyzed rapidly at first. Herein, the feedstock information and the related fast pyrolysis data (**Table 4-1**) obtained by National Renewable Energy Laboratory (NREL) [25] were used with minor modification. Then, the produced volatiles are quickly separated from the char by using a fast gas-solids separator. The



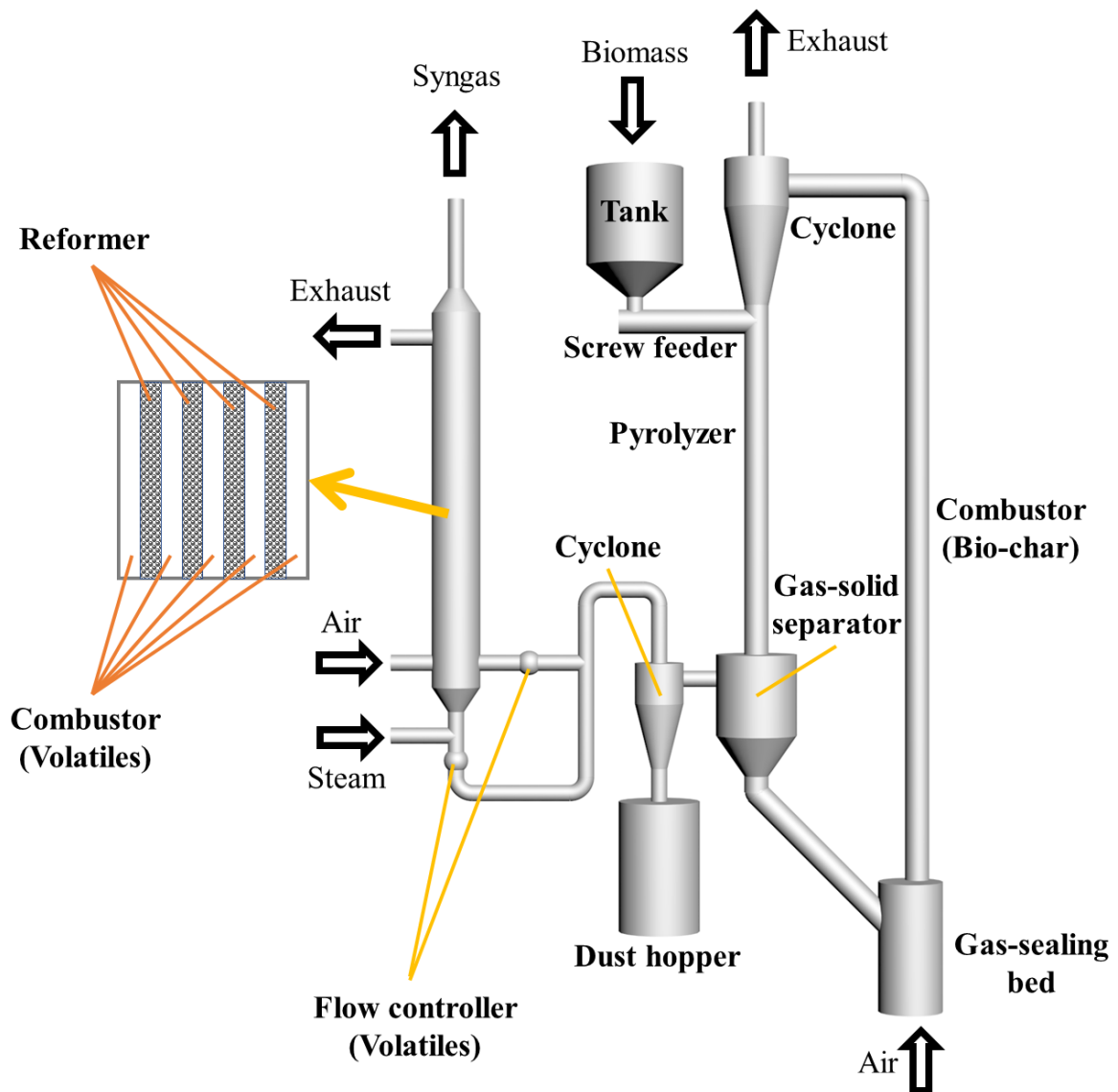


**Fig. 4-3.** Schematic diagram of the proposed separated-type biomass gasification system.

produced bio-char with a relatively low yield from the fast pyrolysis process is not gasified but completely combusted to provide the heat for the pyrolyzer. Meanwhile, the volatiles with a large yield in the fast biomass pyrolysis are separately applied in two parts: the main one is reformed by steam to generate syngas in the tube-reforming reactor and the other is combusted in the shell-combustion reactor to supply heat for the

catalytic tar reforming process. In the reformer, a cheap and active dolomite catalyst is assumed to be used, and as the catalyst is deactivated, the stream of volatiles can be switched to a spare reformer to realize continuous work, and simultaneously, the deactivated catalyst is regenerated or replaced. It should be noted that the pyrolyzer and reformer are independently operated, allowing each can be operated in its optimum condition. In addition, although air is also introduced in the system, the produced syngas is not directly exposed to air, avoiding the dilution by nitrogen. **Table 4-2** summarizes the possible reactions in the separated-type biomass gasification process [15]. Besides, the heat exchanger is used to deliver heat from the hot exhausts of combustors to the pyrolyzer as well as the reformer, and the waste heat boiler is applied to rapidly cool down the crude syngas and simultaneously to generate the steam. The cooled crude syngas is purified before entering the power generation part.

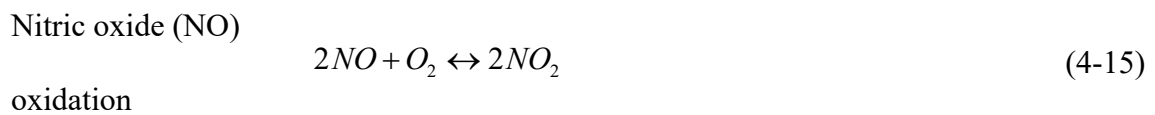
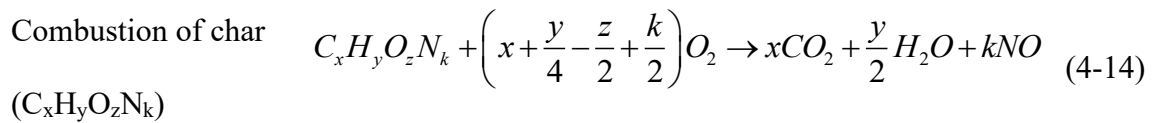
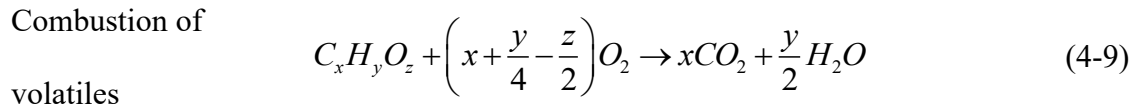
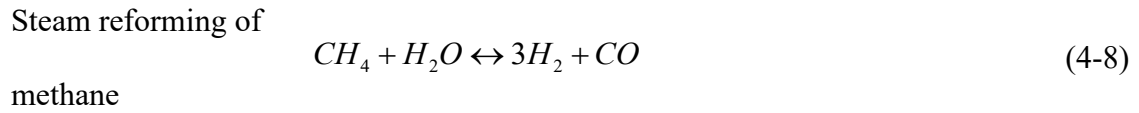
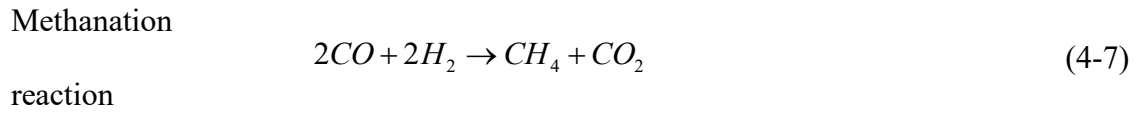
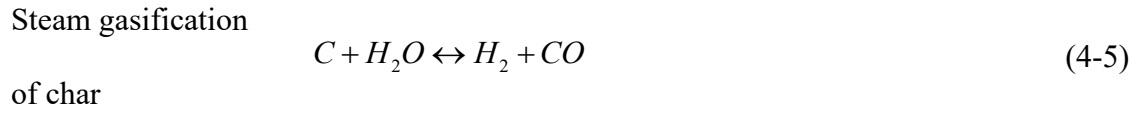
**Table 4-1** Main characteristics of feedstock and pyrolysis products (based on the literatures [25])

<b>Characteristics</b>	<b>Value</b>	<b>Pyrolysis products</b>	<b>(g/kg dry feed)</b>
Particle size	< 3 mm	Bio-oil	
Moisture	7%	Acetic acid (C <sub>2</sub> H <sub>4</sub> O <sub>2</sub> )	59.3
Carbon (C)	50.93%	Propionic acid (C <sub>3</sub> H <sub>6</sub> O <sub>2</sub> )	73.1
Hydrogen (H)	6.05%	Guaiacol (C <sub>7</sub> H <sub>8</sub> O <sub>2</sub> )	6.1
Oxygen (O)	41.93%	Syringol (C <sub>8</sub> H <sub>10</sub> O <sub>3</sub> )	38.0
Nitrogen (N)	0.17%	Formic acid (CH <sub>2</sub> O <sub>2</sub> )	34.1
Sulfur (S)	0.0%	Propyl benzoate (C <sub>10</sub> H <sub>12</sub> O <sub>2</sub> )	163.6

Ash	0.92%	Phenol (C <sub>6</sub> H <sub>6</sub> O)	4.6
Feed rate	107.53 kg/h	Toluene (C <sub>7</sub> H <sub>8</sub> )	22.7
		Furfural (C <sub>5</sub> H <sub>4</sub> O <sub>2</sub> )	189.8
		Benzene (C <sub>6</sub> H <sub>6</sub> )	7.7
		Gas	
		Carbon dioxide (CO <sub>2</sub> )	54.2
		Carbon monoxide (CO)	65.6
		Methane (CH <sub>4</sub> )	0.35
		Ethylene (C <sub>2</sub> H <sub>4</sub> )	1.42
		Hydrogen (H <sub>2</sub> )	5.88
		Propylene (C <sub>3</sub> H <sub>6</sub> )	1.52
		Ammonia (NH <sub>3</sub> )	0.12
		Others	
		Char and ash	162
		Water (H <sub>2</sub> O)	108

**Table 4-2** Reactions in the separated-type biomass gasification process.

Reaction name	Chemical reaction equation	Eq.
Biomass pyrolysis	$Biomass \rightarrow Volatiles (gases + bio - oil) + Char$	(4-1)
Steam reforming of tar (C <sub>x</sub> H <sub>y</sub> O <sub>z</sub> )	$C_xH_yO_z + (x - z)H_2O \rightarrow xCO + \left(x + \frac{y}{2} - z\right)H_2$	(4-2)
Water-gas shift reaction	$CO + H_2O \leftrightarrow H_2 + CO_2$	(4-3)



## 4.2.2 Solid oxide fuel cells

SOFCS has a high electrical efficiency of 40-60% [26], which is applied to convert

the syngas to electricity in this system. As illustrated in Fig. 4-1, the purified syngas and the compressed air are introduced into the anode and cathode of SOFCs, respectively. It is reported that the introduction of an appropriate amount of moisture with the syngas into the SOFCs could improve the efficiency by water-gas shift reaction (WGSR) [27]. Therefore, in this study, the moisture of about 6% (Molar fraction) is assumed to be retained in the syngas after the purification.

The SOFC model is from the publications of Tjaden et al. [28] and Hauck et al. [29] and the detail model using in this work is depicted in Fig. 4-2. The RGibbs block is adopted as the anode of SOFC, by which the electricity output can be calculated by minimizing the Gibbs free energy (G). Meanwhile, the cathode is simulated based on the Sep block which splits the incoming compressed air stream into the oxygen stream and oxygen depleted air stream. Herein, the oxygen stream is introduced into the anode of SOFC to simulate the oxygen species transfer through the SOFC electrolyte. In the SOFC model, the total electric current (I) is calculated based on the electrons needed for the oxidation reaction, fuel utilization factor ( $U_f$ ) and Faraday constant (F) by Eq. (4-16):

$$I = \frac{U_f (2\dot{n}_{H_2} + 8\dot{n}_{CH_4} + 2\dot{n}_{CO})F}{1000} \quad (4-16)$$

Meanwhile, the operating voltage (V) is calculated based on the Gibbs free energy change and area specific resistance (ASR) and current density (j) by Eq. (4-17):

$$V = \frac{\Delta G}{I} - ASR \cdot j \quad (4-17)$$

For a SOFC, the direct current (DC) power output can be calculated by Eq. (4-18):

$$W_{DC} = I \cdot V \quad (4-18)$$

### 4.2.3 Gas turbine

The gas turbine is used to convert the unreacted syngas in SOFCs to the electrical power. Herein, the exhaust expansion in the gas turbine could also compress the air which is used for SOFCs and combustion of unreacted syngas in the gas turbine since the air compressor and gas turbine could be connected on the same shaft. Moreover, in the exhaust discharged from the gas turbine, there is a large amount of energy/exergy in the form of heat, which can be reused for the pre-heating of syngas and air.

### 4.2.4 Simulation methods

In the simulation, solids processing model is adopted. The selected physical property model used for the calculation of the thermodynamic and transport properties of the conventional components is Peng-Robinson equation of state with Boston-Mathias modifications (PR-BM) whereas those for nonconventional components (biomass and bio-char) are the HCOALGEN and DCOALIGT property models. In addition, some essential simulation assumptions for the units and their simulation blocks in Aspen Plus are summarized in **Table 4-3**.

**Table 4-3** Essential simulation assumptions and models in the proposed small-scale high-efficient power generation process.

<b>Unit</b>	<b>Simulation assumption</b>	<b>Simulation model</b>
Biomass pyrolyzer	Temperature: 500 °C Pressure: 1.015 bar [30]	RYield block
Bio-char combustor	Pressure: 1.015 bar	RGibbs block
Tar (Volatiles)	Temperature: 850-1100 °C	RGibbs block

reformer	Pressure: 1.015 bar	
Tar (Volatiles)	Pressure: 1.015 bar	RGibbs block
combustor		
SOFC	Operating temperature: 850 °C	Anode: RGibbs block
	Fuel utilization factor: 0.85	Cathode: Sep block [29]
	Air utilization factor: 0.30	
	DC-AC converter efficiency: 95%	
	ASR: 0.5 $\Omega \cdot \text{cm}^2$ [31]	
Gas turbine	Discharge pressure: 16.2 kPa	Compr block (turbine
	Isentropic efficiency: 90%	model)
	Mechanical and generator	
	efficiency: 98% [26]	
Compressor	Compression ratio: 2.9	Compr block (compressor
	Compressor efficiency: 80%	model)
	Mechanical and electrical	
	efficiency: 98% [32]	
Heat-exchanger	Approach point: 10 °C	Heater and HeatX blocks
	Pinch point: 10 °C	
	Pressure drop: 8% [26]	

---

### 4.3 Energy and Exergy Analyses

In thermodynamics, the results of energy and exergy analyses are usually used to

evaluate the processes of energy/exergy flow, transformation and storage in a system.

### 4.3.1 Energy analysis

The total energy of a stream can be defined as the sum of four types of energy: physical energy, chemical energy, kinetic energy and potential energy, which can be expressed as [33]:

$$En = En_{ph} + En_{ch} + En_{ki} + En_{ep} \quad (4-19)$$

In general, the kinetic and potential energies can be neglected due to their very low values [33]. Thus, the Eq. (4-19) can be simplified to:

$$En = En_{ph} + En_{ch} \quad (4-20)$$

The physical energy of a stream of conventional component can be calculated from the following equation [33]:

$$En_{ph} = \sum_{i=1} \dot{n}_i h_i \quad (4-21)$$

where,

$$h = h_0 + \int_{T_0}^T C_p dT \quad (4-22)$$

$C_p$  is the specific heat capacity of gas at the constant pressure which can be written as [34]:

$$C_p = a + bT + cT^2 + dT^3 \quad (4-23)$$

where  $a$ ,  $b$ ,  $c$ , and  $d$  are empirical coefficients for the specific heat capacity at the constant pressure. **Table 4-4** summarizes the empirical coefficients used in this work.

The chemical energy of a stream of conventional components is expressed by the higher heating value (HHV) [36]:



$$En_{ch} = \sum_{i=1} \dot{n}_i HHV_i \quad (4-24)$$

**Table 4-4** Empirical coefficients of specific heat capacity at the constant pressure [35].

Component	$a$	$b (\times 10^{-2})$	$c (\times 10^{-5})$	$d (\times 10^{-9})$	Temperature range (K)
H <sub>2</sub>	29.11	-0.1916	0.4003	-0.8704	273-1800
CO	28.16	0.1675	0.5327	-2.222	273-1800
CO <sub>2</sub>	22.26	5.981	-3.501	7.469	273-1800
CH <sub>4</sub>	19.89	5.024	1.269	-11.01	273-1800
N <sub>2</sub>	28.90	-0.1571	0.8081	-2.873	273-1800
O <sub>2</sub>	25.48	1.520	-0.7155	1.312	273-1800
H <sub>2</sub> O	32.24	0.1923	1.055	-3.595	273-1800

In general, it is considered that the energy of biomass is equal to chemical energy of biomass [37], which can be expressed as:

$$En_{biomass} = En_{ch,biomass} = \dot{m}_{biomass} HHV_{biomass} \quad (4-25)$$

Meanwhile, the lower heating value of biomass ( $LHV_{biomass}$ ) is calculated from the following equation [38]:

$$LHV_{biomass} = 0.0041868(1+0.15[O]) \left( 7837.667[C] + 33888.889[H] - \frac{[O]}{8} \right) \quad (4-26)$$

where [C], [H], [O], and [N] are the mass fractions of carbon, hydrogen, oxygen, nitrogen elements in the biomass, respectively. According to the relationship between  $LHV_{biomass}$  and  $HHV_{biomass}$ , the  $HHV_{biomass}$  is given by [39]:

$$HHV_{biomass} = LHV_{biomass} + 21.978n_H \quad (4-27)$$

The energy efficiencies of gasification system and the total power plant can be calculated by the following equations:

$$\eta_{En, gasification} = \frac{En_{syngas}}{En_{biomass} + En_{air} + En_{steam} + En_{electricity, input}} \times 100\% \quad (4-28)$$

$$\eta_{En, total} = \frac{En_{electricity, output}}{En_{biomass} + En_{air, total} + En_{steam} + En_{electricity, input}} \times 100\% \quad (4-29)$$

### 4.3.2 Exergy analysis

As we all know, not all energy can be fully utilized in a system. Thus, it is insufficient to evaluate the performance of a system only using energy analysis. Instead, the maximum useful work (i.e., exergy) from a thermal system should be also considered [26]. In other words, the exergy analysis based on the second law of thermodynamics should be a better way for the assessment of energy conversion quality in a system. Similar to energy, the exergy also consists of four parts: physical exergy, chemical exergy, kinetic exergy and potential exergy [33]. That is, the total exergy can be expressed as:

$$Ex = Ex_{ph} + Ex_{ch} + Ex_{ki} + Ex_{ep} \quad (4-30)$$

Herein, the kinetic and potential exergies can be neglected since they are very low. Thus, the Eq. (4-30) can be simplified to:

$$Ex = Ex_{ph} + Ex_{ch} \quad (4-31)$$

The physical energy of a stream of conventional component is calculated from the following equation [33]:

$$Ex_{ph} = \sum_{i=1} \dot{n}_i [(h - h_0) - T_0 (s - s_0)] \quad (4-32)$$

where,

$$s = s_0 + \int_{T_0}^T \frac{C_p}{T} dT - R \ln \frac{P}{P_0} \quad (4-33)$$

The chemical exergy of a stream of conventional component is expressed as:

$$Ex_{ch} = \sum_{i=1} \dot{n}_i (ex_{ch,i} + RT_0 \ln x_i) \quad (4-34)$$

where  $ex_{ch,i}$  is the specific chemical exergies of the components at the dead state which are summarized in **Table 4-5**.

**Table 4-5** Specific chemical exergies of the components at the dead state [40].

Component	Exergy (kJ/kmol)
H <sub>2</sub>	236100
CO	275110
CO <sub>2</sub>	19870
CH <sub>4</sub>	831650
N <sub>2</sub>	720
O <sub>2</sub>	3970
H <sub>2</sub> O (gas)	9500
H <sub>2</sub> O (liquid)	900
Air	900

For the biomass fed at the dead state, the physical exergy can be neglected [41].

Thus, the chemical exergy of biomass is written as:

$$Ex_{biomass} = Ex_{ch,biomass} = \dot{m}_{biomass} \beta LHV_{biomass} \quad (4-35)$$

Herein, when the ratio of  $[O/C] \leq 2$ , the coefficient  $\beta$  can be calculated from the

following equation [41]:

$$\beta = \frac{1.044 + 0.016 \left[ \frac{H}{C} \right] - 0.3493 \left[ \frac{O}{C} \right] \left( 1 + 0.0531 \left[ \frac{H}{C} \right] \right) + 0.0493 \left[ \frac{N}{C} \right]}{1 - 0.4124 \left[ \frac{O}{C} \right]} \quad (4-36)$$

According to the second law of thermodynamics, the exergy is always destroyed and converted to energy during an irreversible process. For a unit or the total system, the exergy destruction is expressed as:

$$Ex_D = Ex_{input} - Ex_{output} \quad (4-37)$$

As such, the exergy efficiencies of gasification process and the total power generation system can be calculated by the following equations:

$$\eta_{Ex, gasification} = \frac{Ex_{syngas}}{Ex_{biomass} + Ex_{air} + Ex_{steam} + Ex_{electricity, input}} \times 100\% \quad (4-38)$$

$$\eta_{Ex, total} = \frac{Ex_{electricity, output}}{Ex_{biomass} + Ex_{air, total} + Ex_{steam} + Ex_{electricity, input}} \times 100\% \quad (4-39)$$

## 4.4 Results and discussion

In this work, the energy and exergy are used to analyze the processes of energy flow, transformation and storage in the system, and the sensitivity, energy and exergy analyses of the proposed novel CHP system are investigated to optimize the performance.

### 4.4.1 Sensitivity analysis of the gasification process.

In order to investigate the effects of operating conditions on the gasification process, detailed sensitivity analyses are implemented by the simulation. As indicated

above, the catalytic reforming of tar can be considered as the main unit for the producing syngas in this separated-type biomass gasification process. Based on the feedstock information and results of fast pyrolysis from NREL, the main product in the fast pyrolysis of wood biomass at 500 °C is tar (volatiles) with the highest yield [42]. In this study, the effects of the reforming temperature ( $T_{SR}$ ) varied from 850-1100 °C and the ratio of steam to carbon in volatiles (S/C) in the range of 2-3 on the complete conversion of tar are simulated at first.

Fig. 4-4 presents the yields of components in the syngas produced from the tar reformer under different operating conditions. It can be seen that the high temperature favors the increase of CO yield while the yields of  $H_2$ ,  $CO_2$  and  $CH_4$  decrease with the increase of temperature. Since the temperature adopted in the simulation is high and the steam reforming reaction of  $CH_4$  (Eq. (4-8)) is endothermic, the yield of  $CH_4$  is very low. It should be noted that the  $H_2/CO$  molar ratio decreases with the increase in the temperature, indicating that water-gas shift reaction should be the dominant reaction in the tar reformer (Fig. 4-5), and the equilibrium of water-gas shift reaction (Eq. (4-3)) is shifted to the direction of CO by increasing the temperature. This behavior is consistent with the Le Chatelier's principle. Meanwhile, the effect of reforming temperature on the LHV of the produced syngas is shown in Fig. 4-6, which indicates that a syngas with a higher LHV can be obtained at a higher temperature. As such, by increasing the temperature from 850 to 1100 °C results in an increase of about 6% in LHV of syngas.

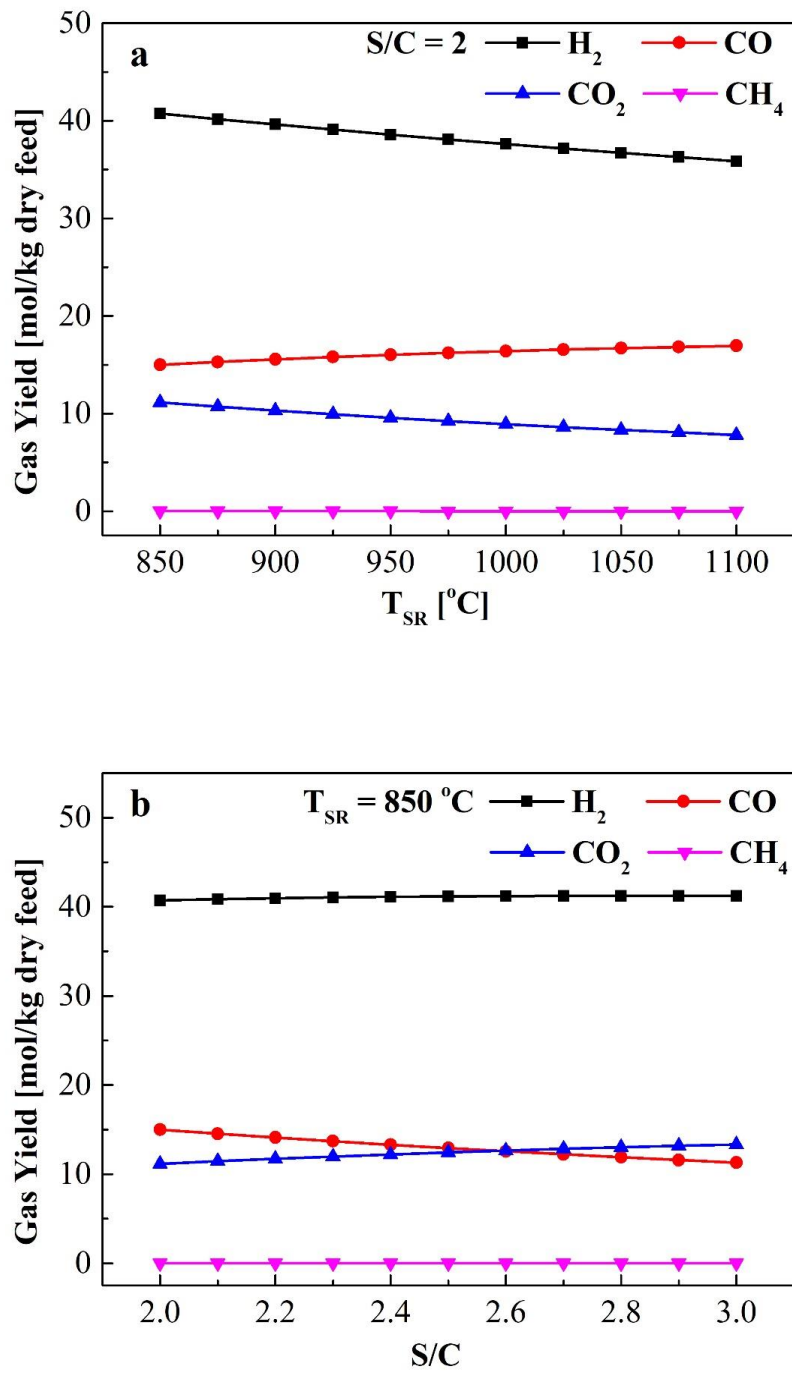


**Fig. 4-4.** Effect of operating condition of steam reforming on the produced syngas composition: a)  $T_{SR}$ , b) S/C.

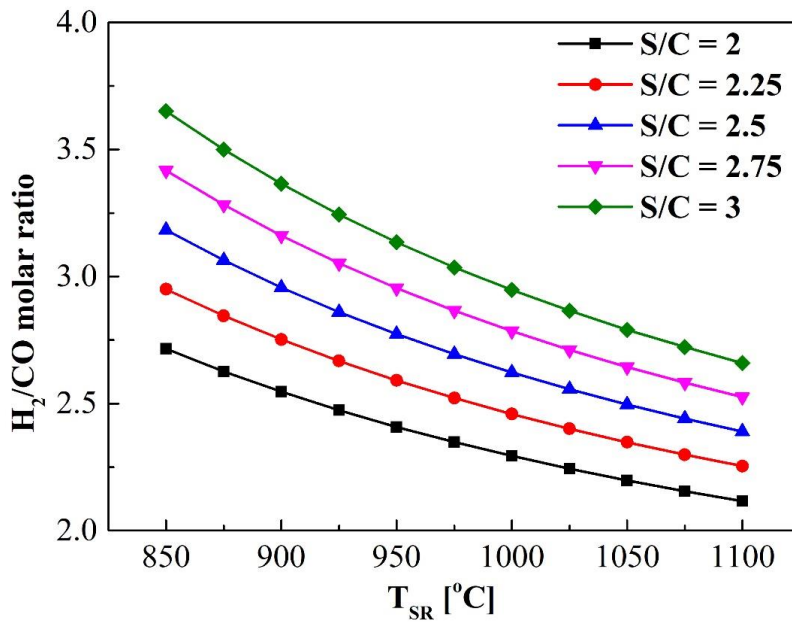


**Fig. 4-5.** Effect of operating condition on H<sub>2</sub>/CO molar ratio of produced syngas.

Compared the yields of the products under different S/C values, the yields of H<sub>2</sub> and CO<sub>2</sub> increase whereas those of CO and CH<sub>4</sub> decrease with the increase of S/C value (Fig. 4-4b), indicating that the increase of steam can shift the equilibrium of water-gas shift reaction (Eq. (4-3)) to the direction of H<sub>2</sub> and CO<sub>2</sub> generations and greatly affect the H<sub>2</sub>/CO molar ratio in the syngas (Fig. 4-5). However, as shown in Fig. 4-5, the LHV of syngas decreases with the increase of S/C due to the dilution of CO<sub>2</sub> and low concentration of CO with a higher LHV. Moreover, the higher steam concentration also further promotes CH<sub>4</sub> conversion to H<sub>2</sub> and CO so that almost no CH<sub>4</sub> is found at high temperature and high S/C conditions.

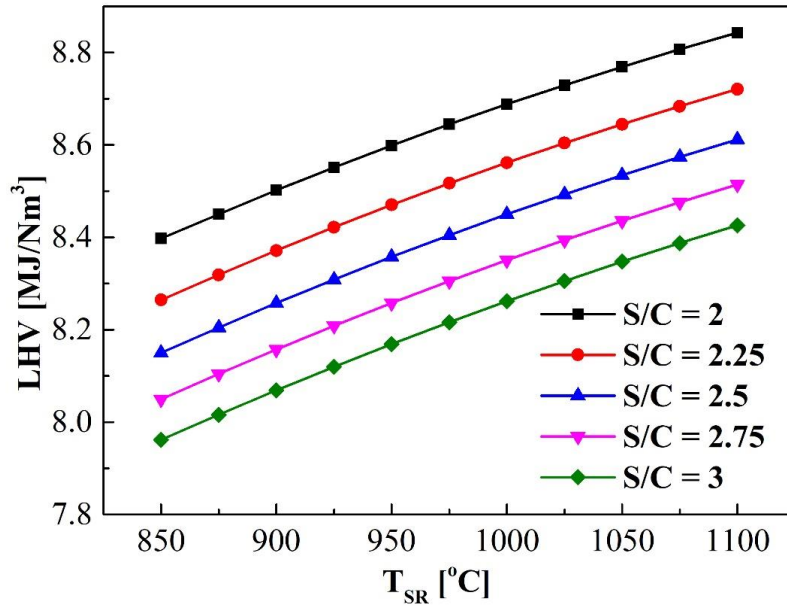


**Fig. 4-6.** Effect of operating condition on LHV of the produced syngas.

The performance of this separated-type biomass gasification process is evaluated by energy and exergy efficiencies. Fig. 4-7 presents the energy efficiencies under different operating conditions. In the studied temperatures and S/C ranges of the tar reforming, the energy efficiency is in the range of 70.6-79.5%, and the energy efficiency decreases with the increase of operation temperature in the reformer. At a higher tar reforming temperature, the equilibrium shifted to CO can absorb more heat. In addition, in this case, more energy is needed for the heating of the volatiles to the reaction temperature since the temperature of volatiles generated from the biomass pyrolyzer is only 500 °C, which is lower than that in the tar reformer. Therefore, more volatiles should be assigned to the volatiles combustor to provide more heat for the tar reformer. As such, less volatiles will be introduced to the tar reformer, which also results in less syngas produced.



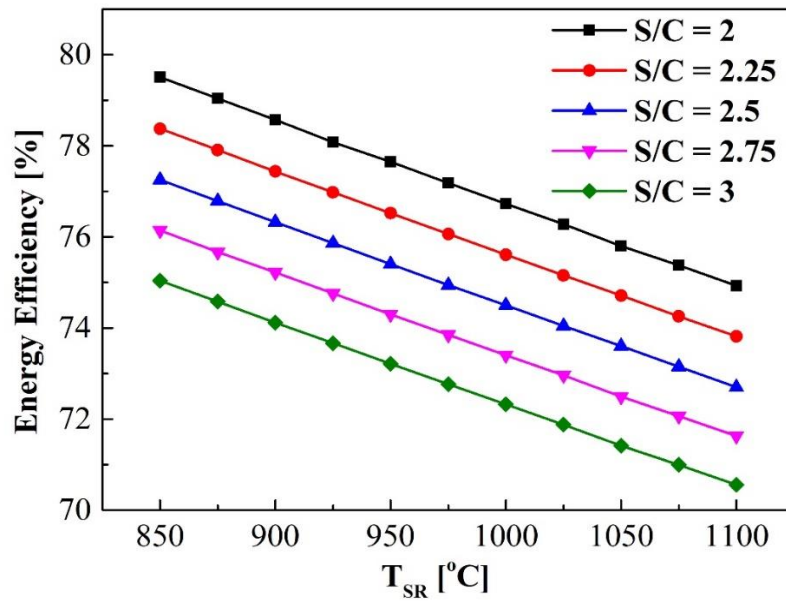


**Fig. 4-7.** Effect of operating condition on energy efficiency of the gasification process.

The energy efficiency can be not only reduced by the increase of temperature, but also decreased with the increase of S/C in the tar reformer (Fig. 4-7). At 850 °C, the energy efficiency decreases from 79.5% to 75.0% in the S/C range of 2-3. The main reason is that the steam needs more energy to be heated to the reaction temperature at a higher S/C. Moreover, in order to maintain a constant temperature in the tar reformer, more volatiles should be assigned to the volatiles combustor to provide more heat for the tar reformer, which also leads to the reduction of syngas. In addition, the decrease of energy efficiency is also attributed to the change of syngas components. According to Eq. (4-25), the chemical energy is depended on HHV. As such, the reduction of flammable components with higher HHV caused by increase of S/C also decreases the chemical energy of syngas.

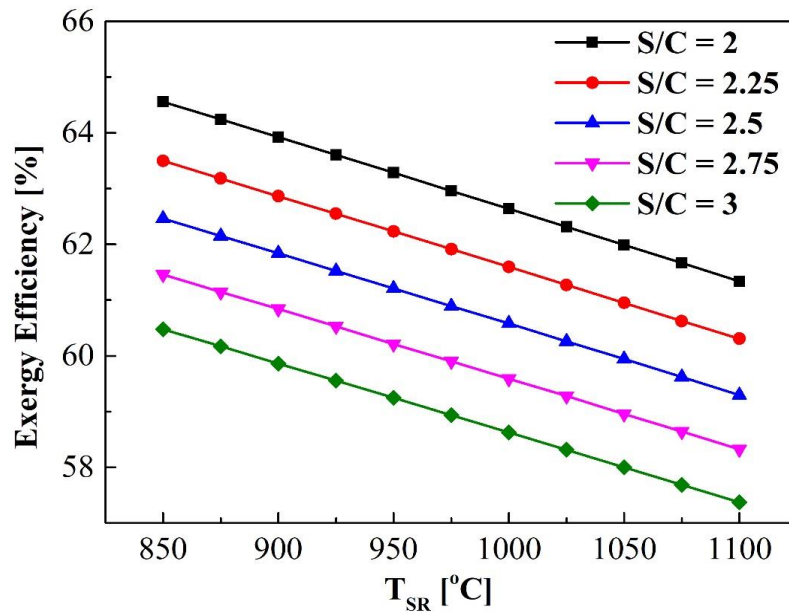


**Fig. 4-8.** Effect of operating condition on exergy efficiency of the gasification system.

Fig. 4-8 depicts the effect of operating condition on the exergy efficiency of this separated-type biomass gasification process. In the investigated temperature and S/C ranges in the tar reformer, the exergy efficiencies are in the range of 57.4-64.6%. One can see that the exergy efficiencies are lower than the energy efficiencies since the entropy changes occurred in the system are considered. As shown in Fig. 4-8, the exergy efficiency has the same trend as the energy efficiency and the highest exergy efficiency is obtained at the condition of 850 °C and S/C = 2. That is, the syngas produced at a relatively lower temperature as well as S/C condition has higher working ability.

#### 4.4.2 Energy and Exergy analyses for the total power generation system

In thermodynamics, the Sankey and Grassmann diagrams are usually used to show the results of energy and exergy analyses respectively by illustrating the enthalpy and exergy flows for the evaluation of plant performance, in which the directions of flows

are represented by the arrows, and the width expresses the amount of energy/exergy. In this study, the total power generation system is simulated at the nominal condition, in which the tar reformer operating condition of 850 °C and S/C = 2 is adopted to get the maximum power generation.

The Sankey diagram of the total power generation system is shown in Fig. 4-9 and the detail energy results, mass flow, temperature and pressure of all streams are summarized in **Tables 4-6** and **4-7**. One can see that the biomass input of 548.86 kW (HHV) can result in an electrical power output of 263.65 kW by using this system. As indicated in the Fig. 4-9, the energy of about 137.72 kW is from the hot exhaust and discharges in the gasification system. Herein, the heat exchangers are used for the energy recuperation, and it is found that half of the energy in the hot exhaust (72.14 kW) can be recuperated and reused in the gasification system. After delivering the energy for air heating, 65.58 kW of energy could be lost through the exhaust in the stack. Moreover, 81.31 kW of energy can be released during the cooling of the crude syngas, which is used to convert water into steam by the waste heat boiler. The generated steam is injected into the tar reformer for the production of syngas, achieving an energy recuperation. As such, under the actions of these recuperators (i.e., heat exchangers and waste heat boiler), only about 74% of the energy input for the gasification is needed from the biomass and the produced syngas with 468.56 kW of energy can be obtained and further used for the following electricity generation process.

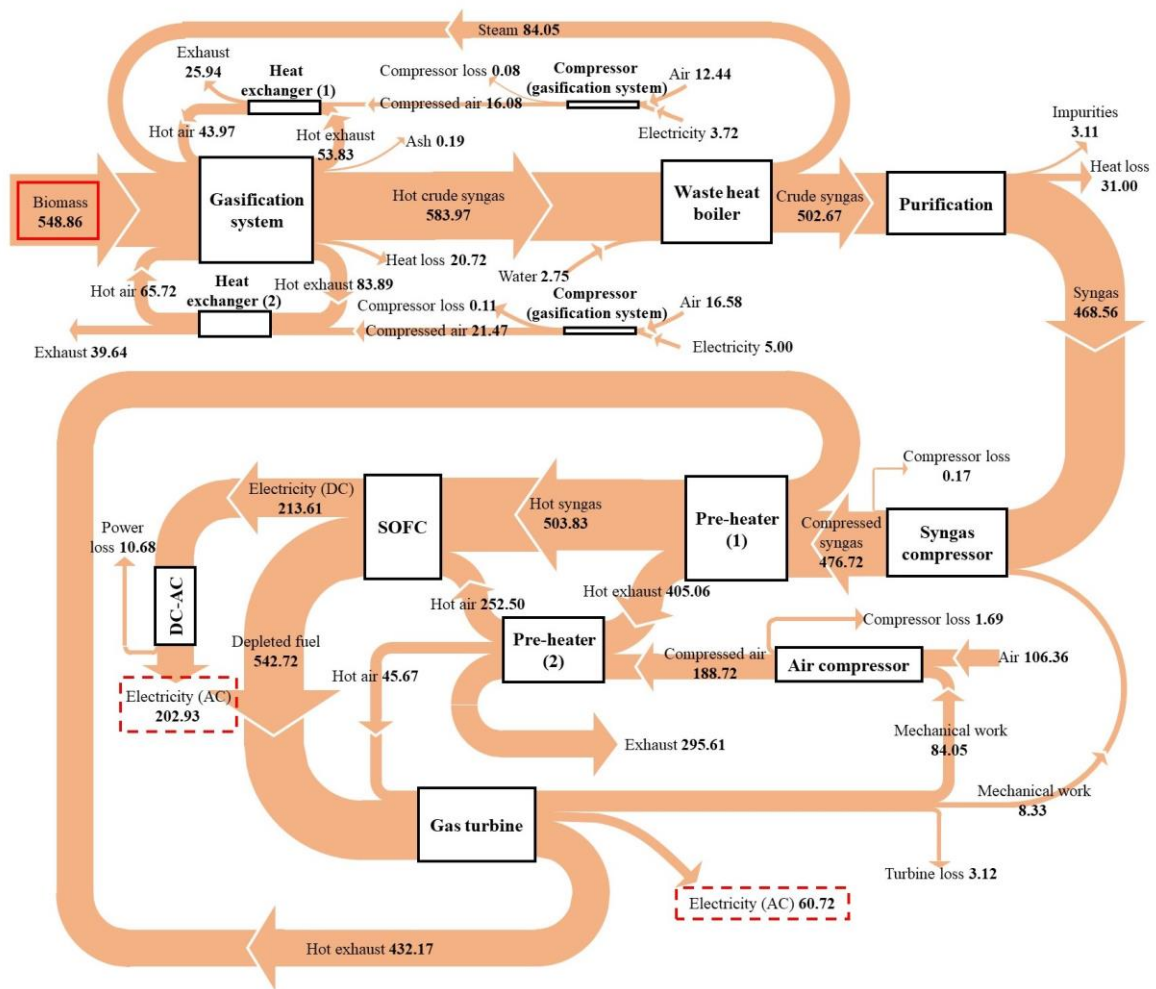


**Fig. 4-9.** Sankey diagram of the total power generation system. (Energy flows are expressed in kW.)

The possibility of energy recuperation from the electricity generation process is also analyzed. As shown in Fig. 4-9, the energy presented in the hot exhaust outflowing from the gas turbine can reach as high as 432.17 kW. In order to avoid energy waste and improve total energy efficiency, the energy in the high temperature exhaust is recuperated by the pre-heaters (heat exchanger) for syngas and air. As such, in the pre-heating process, the syngas and air can carry about 136.56 kW of energy back to the electricity generation process. The pre-heating of syngas and air can not only favor the

improvement of power production, but also prevent the formation of large temperature gradient in the SOFCs from causing the thermal stress to break the fuel cell. In the SOFCs, about 28.2% of energy is converted to electricity with a final electricity output of 202.93 kW after the DC-AC conversion. The depleted fuel from SOFC is completely burned for driving the gas turbine with an output of 60.72 kW of electricity. Furthermore, through the shaft, the gas turbine could also drive the syngas and air compressors in the electricity generation system with an energy consumption of 95.38 kW. As a result, a total plant energy efficiency of 37.9% can be achieved.

#### **4.4.3 Exergy analysis of total power generation system**

The Grassmann diagram (exergy flow) (Fig. 4-10), which can illustrate the quality of energy stream, is used to further assess the performance of the total power generation system, which could also show the exergy destruction in the system. Herein, the detail exergy results of all streams are summarized in **Table 4-8**. **Table 4-9** summarizes the exergy efficiencies and exergy destructions of the units calculated in this power generation system with the defined inputs and outputs. As a result, the exergy efficiency of total power generation system reaches as high as 43.2%. Herein, in the gasification system, the exergies of 40.39 kW and 32.63 kW are recuperated by air and steam, respectively, which accounts for about 10.9% of the exergy input of gasification system. After the purification of crude syngas, the purified syngas with 387.25 kW of exergy is introduced into the electrical power generation system. In addition, by using the pre-heaters, 74.36 kW of exergy in the exhaust is delivered to syngas and air, further enhancing electrical power output.

In the total power generation system, total exergy loss is approximately 347.35 kW,

of which only 19.8% is lost to environment through the exhaust. It should be noted that most of exergy loss is caused by exergy destruction during the energy conversion. As summarized in **Table 4-9**, the biomass gasification process contributes the largest exergy destruction, which accounts for about 48.9% of the total exergy loss. It is mainly resulted from the irreversible exothermic combustion process [26]. Herein, the decrease in exergy efficiency should be also caused by more volatiles assigned to the volatiles combustor in the case of tar reforming at high temperature as well as high S/C. These results indicate that the exergy efficiency of the gasification system could be further optimized by the ways such as enhancing the thermal insulation and applying more excellent catalysts so that the biomass can be completely converted at lower temperature, lower S/C, and higher space velocity conditions.

**Table 4-10** summarizes and compares the total exergy efficiency of the present CHP system with those reported typical ones. One can see that this proposed CHP system has higher exergy efficiency than those conventional ones. Since the CHP system with only a single SOFC cannot fully utilize fuel, the SOFC is often integrated with GT in the recent studies. In these systems, except [43], most of them using the steam as the gasifying agent show better performances since the diluting of syngas by the nitrogen in air can be avoided. Compared with other reported ones, the proposed CHP system in this work can obtain a relatively high exergy efficiency (43.2%) by combining the steam tar reforming with the SOFC-GT power generators. Moreover, the present unique gasification system design could not only eliminate the negative effect from reaction time differences of pyrolysis, combustion and reforming, but also realize the heat recuperation and catalyst regeneration effectively.

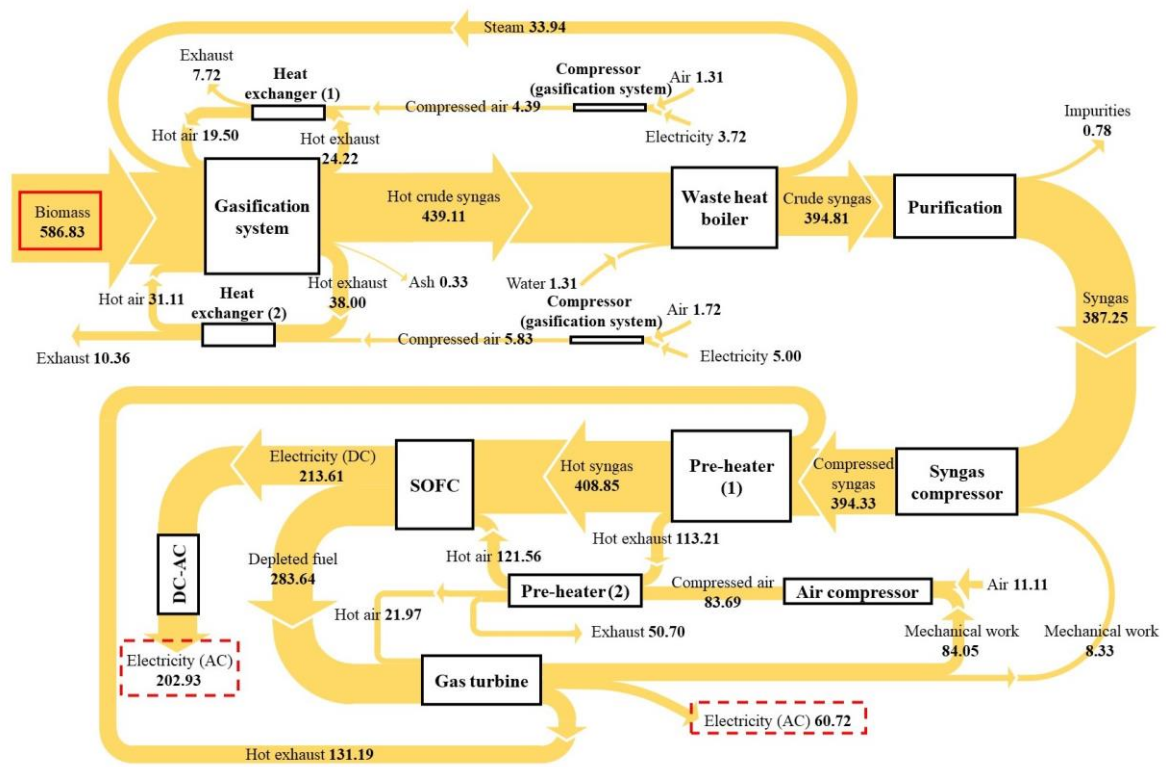


**Fig. 4-10.** Grassmann diagram of the total power generation system. (Exergy flows are expressed in kW.)

**Table 4-6** Detail energy results of every stream

<b>Unit</b>	<b>Inlet stream</b>	<b>Energy (kW)</b>	<b>Outlet stream</b>	<b>Energy (kW)</b>
Gasification system	Biomass	548.86	Hot crude syngas	583.97
	Steam	84.05	Ash	0.19
	Hot air (from heat exchanger (1))	43.97	Hot exhaust (to heat exchanger (1))	53.83
	Hot air (from heat exchanger (2))	65.72	Hot exhaust (to heat exchanger (2))	83.89
			Heat loss (from compressor (gasification system))	20.72
Heat exchanger (1)	Compressed air (to heat exchanger (1))	16.08	Exhaust (from heat exchanger (1))	25.94



---

	Hot exhaust (to heat exchanger (1))	53.83	Hot air (from heat exchanger (1))	43.97
Heat exchanger (2)	Compressed air (to heat exchanger (2))	21.47	Exhaust (from heat exchanger (2))	39.64
	Hot exhaust (to heat exchanger (2))	83.89	Hot air (from heat exchanger (2))	65.72
Compressor (gasification system)	Air (to compressor (gasification system))	29.02	Compressed air (to heat exchanger (1))	16.08
	Electricity	8.72	Compressed air (to heat exchanger (2))	21.47
			Compressor loss (from compressor (gasification system))	0.19

---

---

Waste heat boiler	Hot crude syngas	583.97	Steam	84.05
	Water	2.75	Crude syngas	502.67
Purification	Crude syngas	502.67	Syngas	468.56
			Impurities	3.11
			Heat loss (from purification)	31.00
Syngas compressor	Syngas	468.56	Compressed syngas	476.72
	Mechanical work (to syngas compressor)	8.33	Compressor loss (from syngas compressor)	0.17
Pre-heater (1)	Compressed syngas	476.72	Hot syngas	503.83
	Hot exhaust (from gas	432.17	Hot exhaust (from pre-	405.06

---

---

	turbine)		heater (1))	
Pre-heater (2)	Hot exhaust (from pre-heater (1))	405.06	Hot air (to SOFC)	252.50
	Compressed air (from air compressor)	188.72	Hot air (to gas turbine)	45.67
			Exhaust (from pre-heater (2))	295.61
SOFC	Hot syngas	503.83	Electricity (DC)	213.61
	Hot air (to SOFC)	252.50	Depleted fuel	542.72
DC-AC	Electricity (DC)	213.61	Electricity (AC) (from DC-AC)	202.93
			Power loss	10.68

---

---

Gas turbine	Depleted fuel	542.72	Electricity (AC) (from gas turbine)	60.72
	Hot air (to gas turbine)	45.67	Mechanical work (to syngas compressor)	8.33
			Mechanical work (to air compressor)	84.05
			Turbine loss	3.12
			Hot exhaust (from gas turbine)	432.17
Air compressor	Air (to air compressor)	106.36	Compressor loss (from air compressor)	1.69
	Mechanical work (to air compressor)	84.05	Compressed air (from air compressor)	188.72

---

**Table 4-7** Mass flows, temperatures and pressures of every stream

<b>Stream</b>	<b>Mass flow (kg/h)</b>	<b>Temperature (°C)</b>	<b>Pressure (kPa)</b>
Biomass	100.00	25.00	101.50
Hot crude syngas	158.26	850.00	101.50
Crude syngas	158.26	84.49	85.91
Syngas	106.88	50.00	85.91
Compressed syngas	106.88	181.98	441.66
Hot syngas	106.88	595.35	441.66
Depleted fuel	1193.36	850.00	441.66
Hot exhaust (from gas turbine)	1389.88	605.35	17.73
Hot exhaust (from pre-heater (1))	1389.88	546.27	16.31
Exhaust (from pre-heater (2))	1389.88	298.93	15.00
Air (to compressor (gasification system))	350.00	25.00	0.00
Compressed air (to heat exchanger (1))	150.00	111.61	110.00

Hot air (from heat exchanger (1))	150.00	730.00	110.00
Hot exhaust (to heat exchanger (1))	165.47	740.00	101.50
Exhaust (from heat exchanger (1))	165.47	207.55	93.38
Compressed air (to heat exchanger (2))	200.00	111.61	110.00
Hot air (from heat exchanger (2))	200.00	840.00	110.00
Hot exhaust (to heat exchanger (2))	219.73	850.66	101.50
Exhaust (from heat exchanger (2))	219.73	236.42	93.38
Ash	0.92	740.00	101.50
Water	94.38	25.00	0
Steam	94.38	318.78	101.50
Impurities	51.38	50.00	85.91
Air (to air compressor)	1283.00	25.00	0.00
Compressed air (from air compressor)	1283.00	250.81	441.66
Hot air (to SOFC)	1086.48	536.27	441.66
Hot air (to gas turbine)	196.52	536.27	441.66

**Table 4-8** Detail exergy results of every stream

<b>Unit</b>	<b>Inlet stream</b>	<b>Exergy (kW)</b>	<b>Outlet stream</b>	<b>Exergy (kW)</b>
Gasification system	Biomass	586.83	Hot crude syngas	439.11
	Steam	33.94	Ash	0.33
	Hot air (from heat exchanger (1))	19.5	Hot exhaust (to heat exchanger (1))	24.22
	Hot air (from heat exchanger (2))	31.11	Hot exhaust (to heat exchanger (2))	38.00
Heat exchanger (1)	Compressed air (to heat exchanger (1))	4.39	Exhaust (from heat exchanger (1))	7.72
	Hot exhaust (to heat exchanger (1))	24.22	Hot air (from heat exchanger (1))	19.50

Heat exchanger (2)	Compressed air (to heat exchanger (2))	5.83	Exhaust (from heat exchanger (2))	10.36
	Hot exhaust (to heat exchanger (2))	38.00	Hot air (from heat exchanger (2))	31.11
Compressor (gasification system)	Air (to compressor (gasification system))	3.03	Compressed air (to heat exchanger (1))	4.39
	Electricity	8.72	Compressed air (to heat exchanger (2))	5.83
Waste heat boiler	Hot crude syngas	439.11	Steam	33.94
	water	1.31	Crude syngas	394.81
Purification	Crude syngas	394.81	Syngas	387.25
			Impurities	0.78



---

Syngas compressor	Syngas	387.25	Compressed syngas	394.33
	Mechanical work (to syngas compressor)	8.33		
Pre-heater (1)	Compressed syngas	394.33	Hot syngas	408.85
	Hot exhaust (from gas turbine)	131.19	Hot exhaust (from pre-heater (1))	113.21
Pre-heater (2)	Hot exhaust (from pre-heater (1))	113.21	Hot air (to SOFC)	121.56
	Compressed air (from air compressor)	83.69	Hot air (to gas turbine)	21.97
			Exhaust (from pre-heater (2))	50.70

---

---

SOFC	Hot syngas	408.85	Electricity (DC)	213.61
	Hot air (to SOFC)	121.56	Depleted fuel	283.64
DC-AC	Electricity (DC)	213.61	Electricity (AC) (from DC-AC)	202.93
Gas turbine	Depleted fuel	283.64	Electricity (AC) (from gas turbine)	60.72
	Hot air (to gas turbine)	21.97	Mechanical work (to syngas compressor)	84.05
			Mechanical work (to air compressor)	8.33
			Hot exhaust (from gas turbine)	131.19

---

Air compressor	Air (to air compressor)	11.11	Compressed air (from air compressor)	83.69
	Mechanical work (to air compressor)	84.05		

**Table 4-9** The calculated exergy efficiencies and exergy destructions of different units.

Unit	Exergy efficiency equation	Exergy efficiency (%)	Input	Output	Exergy destruction (kW)
Gasification process	$\frac{Ex_{biomass} + Ex_{hot\ air} + Ex_{steam}}{Ex_{hot\ crude\ syngas} + Ex_{hot\ exhaust} + Ex_{ash}}$	74.7	Biomass, hot air, steam	Hot crude syngas, hot exhaust, ash	169.72
Heat exchanger (1)	$\frac{Ex_{hot\ air} - Ex_{compressed\ air}}{Ex_{hot\ exhaust} - Ex_{exhaust}}$	91.6	Exergy decrease of exhaust	Exergy increase of air	1.39
Heat exchanger (2)	$\frac{Ex_{hot\ air} - Ex_{compressed\ air}}{Ex_{hot\ exhaust} - Ex_{exhaust}}$	91.5	Exergy decrease of exhaust	Exergy increase of air	2.36

Compressor (gasification system)	$\frac{Ex_{compressed\ air} - Ex_{air}}{Ex_{electricity}}$	82.5	Electricity	Exergy increase of air	1.53
Waste heat boiler	$\frac{Ex_{steam} - Ex_{water}}{Ex_{hot\ crude\ syngas} - Ex_{crude\ syngas}}$	73.7	Exergy decrease of crude syngas	Exergy increase of steam	11.67
Purification	$\frac{Ex_{syngas} + Ex_{impurities}}{Ex_{crude\ syngas}}$	98.3	Crude syngas	Syngas, impurities	6.78
Syngas compressor	$\frac{Ex_{compressed\ syngas} - Ex_{syngas}}{Ex_{mechanical\ work}}$	85.0	Mechanical work from gas turbine	Exergy increase of syngas	1.25
Air compressor	$\frac{Ex_{compressed\ air} - Ex_{air}}{Ex_{mechanical\ work}}$	86.4	Mechanical work from gas turbine	Exergy increase of air	11.47
Pre-heater (1)	$\frac{Ex_{hot\ syngas} - Ex_{compressed\ syngas}}{\Delta Ex_{hot\ exhaust}}$	80.8	Exergy decrease of exhaust	Exergy increase of syngas	3.46
Pre-heater (2)	$\frac{Ex_{hot\ air} - Ex_{compressed\ air}}{Ex_{hot\ exhaust} - Ex_{exhaust}}$	95.7	Exergy decrease of exhaust	Exergy increase of air	2.67
SOFC	$\frac{Ex_{DC\ power} + Ex_{depleted\ fuel}}{Ex_{hot\ syngas} + Ex_{hot\ air}}$	93.7	Hot syngas, hot air	DC power, depleted fuel	33.16

DC-AC inverter	$\frac{Ex_{AC\ power}}{Ex_{DC\ power}}$	95.0	DC power	AC power	10.68
Gas turbine	$\frac{Ex_{AC\ power} + Ex_{mechanical\ work} + Ex_{hot\ exhaust}}{Ex_{depleted\ fuel} + Ex_{hot\ air}}$	93.0	Depleted fuel, hot air	AC power, mechanical work, hot exhaust	21.32

**Table 4-10** Comparison of the performance of the present novel small-scale CHP system with other reported biomass gasification CHP systems.

No.	Feed fuel	Gasifying agent	System features	Main units	Exergy efficiency (%)	Ref.
1	Wood	Steam	Conventional CHP system	Gasifier; SOFC	36	[44]
2	Wood	Air	Conventional CHP system	Gasifier; SOFC	28	[44]
3	Wood	Steam	Micro CHP system combined with a compression heat pump	Gasifier; SOFC; Compression heat pump	42.3	[45]
4	Wood	Steam	CHP system with hot gas cleanup	Gasifier; SOFC; Hot gas filter	39.1	[46]
5	Wood	Air	CHP system coupled with	Gasifier; SOFC; CO <sub>2</sub> turbine	40.1	[47]

			supercritical CO <sub>2</sub> cycle			
6	Rice straw	Air	Micro multi-stage CHP system integrated with ORC (organic Rankine cycle)	Gasifier; SOFC; GT; ORC turbine	35.1	[48]
7	Rice husk	Steam	CHP system combined with high-temperature sodium heat pipes	Gasifier; SOFC; Heat pipes	44.22	[49]
8	Wood	CO <sub>2</sub>	CHP system using CO <sub>2</sub> gasifying agent	Gasifier; SOFC; GT; SOEC (solid oxide electrolysis cell)	45.25	[50]
9	Wood	Air	CHP system using novel externally fired gas turbine (EFGT)	Gasifier; SOFC; EFGT; ORC turbine	44.2	[43]
10	Wood	Steam	Small-scale high-efficient power generation system with a separated-type biomass gasification process and energy/exergy recuperation	Gasifier; SOFC; GT	43.2	This work

## 4.5 Conclusions

In summary, a small-scale high-efficient power generation system with a separated-type biomass gasification system based on energy/exergy recuperation is proposed and simulated based on the reported results, in which the fast pyrolysis of biomass combined with the catalytic steam tar reforming is considered in this new system for the first time. In order to obtain the optimal operating conditions, the influences of temperature and S/C on the performance of catalytic steam tar reformer as well as the gasification system are investigated in details. Meanwhile, the energy and exergy analyses of the total power generation system is also performed and the Sankey and Grassmann diagrams are drawn to illustrate the enthalpy and exergy flows, respectively.

The main results are summarized as follows:

- (1) The condition of relatively lower temperature as well as S/C for the reforming is in favor of the performance of the total gasification system to produce more syngas with higher energy/exergy. It is found that the energy and exergy efficiencies of the total gasification system are 79.5% and 64.6%, respectively, in the optimum case of  $T_{SR} = 850\text{ }^{\circ}\text{C}$  and  $S/C = 2$ .
- (2) In the gasification system, 72.14 kW and 81.30 kW of energies could be recuperated from the exhausts and the crude syngas cooling process, respectively. Meanwhile, 136.56 kW of energy carried by air from the gas turbine exhaust could be recuperated in the electricity generation system. As a result, this power generation system could produce an electrical power output of 263.65 kW and achieve a total energy efficiency of 37.9%.
- (3) By the evaluation based on the law of thermodynamics with the corresponding

Grassmann diagram, the total exergy efficiency could reach as high as 43.2%. Although 73.02 kW of exergy can be recuperated by air (for gasification) and steam, the gasification system is found to contribute the largest exergy destruction, which accounts for almost half of the total exergy loss. Moreover, 74.36 kW of exergy could be recuperated from the gas turbine exhaust in the electricity generation system, further enhancing the power output.

## Nomenclature

### Notations

$a, b, c, d$	empirical coefficients (-)
$ASR$	area specific resistance ( $\Omega \cdot \text{cm}^2$ )
$C_p$	constant pressure specific heat capacity ( $\text{kJ}/\text{kmol} \cdot \text{K}$ )
$C$	carbon content in biomass (w%)
$ex$	standard exergy ( $\text{kJ}/\text{kmol}$ )
$En$	energy ( $\text{kJ}/\text{kg}$ )
$Ex$	exergy ( $\text{kJ}/\text{kg}$ )
$F$	Faraday constant ( $\text{C}/\text{mol}$ )
$G$	Gibbs free energy ( $\text{kJ}$ )
$h$	specific enthalpy ( $\text{kJ}/\text{kmol}$ )
$H$	hydrogen content in biomass (w%)
$I$	total electric current ( $\text{A}$ )
$j$	current density ( $\text{A}/\text{cm}^2$ )
$\dot{m}$	mass flow rate ( $\text{kg}/\text{s}$ )



$\dot{n}$	component molar flow rate (kmol/s)
$n_H$	number of moles of hydrogen content (mol/kg)
$N$	nitrogen content in biomass (w%)
$O$	oxygen content in biomass (w%)
$P$	pressure (Pa)
$R$	universal gas constant (kJ/kmol·K)
$s$	specific entropy (kJ/kmol·K)
$T$	temperature (K)
$U_f$	fuel utilization factor (-)
$V$	voltage (V)
$W_{DC}$	direct current power output of solid oxide fuel cells
$X$	molar fraction (-)

*Greek letters*

$\beta$	correlation factor (-)
$\eta$	efficiency (%)

*Subscripts*

$ch$	chemical
$D$	destruction
$ep$	potential
$En$	energy
$Ex$	exergy
$i$	component
$ki$	kinetic

<i>ph</i>	physical
<i>SR</i>	steam reforming
<i>0</i>	standard condition (dead state)
<i>Acronym</i>	
<i>AC</i>	alternate current
<i>CHP</i>	Combined heat and power
<i>CFB</i>	Circulating fluidized bed
<i>DC</i>	direct current
<i>HHV</i>	higher heating value (kJ/kmol or kJ/kg)
<i>LHV</i>	lower heating value (kJ/kmol or kJ/kg)
<i>PR-BM</i>	Peng-Robinson equation of state with Boston-Mathias modifications
<i>S/C</i>	ratio of steam to carbon
<i>SOFC</i>	solid oxide fuel cell
<i>WGSR</i>	water-gas shift reaction

## References

- [1] Bai Z, Liu Q, Gong L, Lei J. Investigation of a solar-biomass gasification system with the production of methanol and electricity: Thermodynamic, economic and off-design operation. *Appl Energy* 2019;243:91-101.
- [2] Karanfil F, Li Y. Electricity consumption and economic growth: Exploring panel-specific differences. *Energy Policy* 2015;82:264-77.
- [3] Liddle B, Sadorsky P. How much does increasing non-fossil fuels in electricity generation reduce carbon dioxide emissions? *Appl Energy* 2017;197:212-21.

- [4] Shafiee S, Topal E. When will fossil fuel reserves be diminished? *Energy Policy* 2009;37:181-9.
- [5] Wang H, Lei Z, Zhang X, Zhou B, Peng J. A review of deep learning for renewable energy forecasting. *Energy Convers Manage* 2019;198:111799.
- [6] Detchusananard T, Sharma S, Maréchal F, Arpornwichanop A. Multi-objective optimization of sorption enhanced steam biomass gasification with solid oxide fuel cell. *Energy Convers Manage* 2019;182:412-29.
- [7] Sher F, Iqbal SZ, Liu H, Imran M, Snape CE. Thermal and kinetic analysis of diverse biomass fuels under different reaction environment: A way forward to renewable energy sources. *Energy Convers Manage* 2020;203:112266.
- [8] Situmorang YA, Zhao Z, Yoshida A, Kasai Y, Abudula A, Guan G. Potential power generation on a small-scale separated-type biomass gasification system. *Energy* 2019;179:19-29.
- [9] Caputo AC, Palumbo M, Pelagagge PM, Scacchia F. Economics of biomass energy utilization in combustion and gasification plants: effects of logistic variables. *Biomass Bioenergy* 2005;28:35-51.
- [10] Guan G, Fushimi C, Tsutsumi A, Ishizuka M, Matsuda S, Hatano H, et al. High-density circulating fluidized bed gasifier for advanced IGCC/IGFC—Advantages and challenges. *Particuology* 2010;8:602-6.
- [11] Mertzis D, Koufodimos G, Kavvadas I, Samaras Z. Applying modern automotive technology on small scale gasification systems for CHP production: A compact hot gas filtration system. *Biomass Bioenergy* 2017;101:9-20.
- [12] Perna A, Minutillo M, Jannelli E, Cigolotti V, Nam SW, Yoon KJ. Performance assessment of a hybrid SOFC/MGT cogeneration power plant fed by syngas from a

biomass down-draft gasifier. *Appl Energy* 2018;227:80-91.

[13] de Lasa H, Salaices E, Mazumder J, Lucky R. Catalytic steam gasification of biomass: catalysts, thermodynamics and kinetics. *Chem Rev* 2011;111:5404-33.

[14] Wang L, Weller CL, Jones DD, Hanna MA. Contemporary issues in thermal gasification of biomass and its application to electricity and fuel production. *Biomass Bioenergy* 2008;32:573-81.

[15] Guan G, Kaewpanha M, Hao X, Abudula A. Catalytic steam reforming of biomass tar: Prospects and challenges. *Renew Sustain Energy Rev* 2016;58:450-61.

[16] Ge H, Zhang H, Guo W, Song T, Shen L. System simulation and experimental verification: Biomass-based integrated gasification combined cycle (BIGCC) coupling with chemical looping gasification (CLG) for power generation. *Fuel* 2019;241:118-28.

[17] Dupont C, Boissonnet G, Seiler J-M, Gauthier P, Schweich D. Study about the kinetic processes of biomass steam gasification. *Fuel* 2007;86:32-40.

[18] Situmorang YA, Zhao Z, Yoshida A, Abudula A, Guan G. Small-scale biomass gasification systems for power generation (<200 kW class): A review. *Renew Sustain Energy Rev* 2020;117.

[19] Karl J, Pröll T. Steam gasification of biomass in dual fluidized bed gasifiers: A review. *Renew Sustain Energy Rev* 2018;98:64-78.

[20] Kan T, Strezov V, Evans TJ. Lignocellulosic biomass pyrolysis: A review of product properties and effects of pyrolysis parameters. *Renew Sustain Energy Rev* 2016;57:1126-40.

[21] Zhao Z, Situmorang YA, An P, Chaihad N, Wang J, Hao X, et al. Hydrogen production from catalytic steam reforming of bio-oils: a critical review. *Chemical Engineering Technology* 2020;43:625-40.

- [22] Wang J-J, Yang K, Xu Z-L, Fu C. Energy and exergy analyses of an integrated CCHP system with biomass air gasification. *Appl Energy* 2015;142:317-27.
- [23] Omosun AO, Bauen A, Brandon NP, Adjiman CS, Hart D. Modelling system efficiencies and costs of two biomass-fuelled SOFC systems. *J Power Sources* 2004;131:96-106.
- [24] Giuffrida A, Romano MC, Lozza G. Thermodynamic analysis of air-blown gasification for IGCC applications. *Appl Energy* 2011;88:3949-58.
- [25] Ringer M, Putsche V, Seahill J. Large-Scale Pyrolysis Oil Production: A Technology Assessment and Economic Analysis. Colorado (USA): National Renewable Energy Laboratory; 2006.
- [26] Chen S, Lior N, Xiang W. Coal gasification integration with solid oxide fuel cell and chemical looping combustion for high-efficiency power generation with inherent CO<sub>2</sub> capture. *Appl Energy* 2015;146:298-312.
- [27] De Lorenzo G, Fragiaco P. Energy analysis of an SOFC system fed by syngas. *Energy Convers Manage* 2015;93:175-86.
- [28] Tjaden B, Gandiglio M, Lanzini A, Santarelli M, Järvinen M. Small-scale biogas-SOFC plant: technical analysis and assessment of different fuel reforming options. *Energy Fuels* 2014;28:4216-32.
- [29] Hauck M, Herrmann S, Spliethoff H. Simulation of a reversible SOFC with Aspen Plus. *Int J Hydrogen Energy* 2017;42:10329-40.
- [30] Görling M, Larsson M, Alvfors P. Bio-methane via fast pyrolysis of biomass. *Appl Energy* 2013;112:440-7.
- [31] Kuchonthara P, Bhattacharya S, Tsutsumi A. Energy recuperation in solid oxide fuel cell (SOFC) and gas turbine (GT) combined system. *J Power Sources* 2003;117:7-

13.

[32] George RA. Status of tubular SOFC field unit demonstrations. *J Power Sources* 2000;86:134-9.

[33] Nakyai T, Authayanun S, Patcharavorachot Y, Arpornwichanop A, Assabumrungrat S, Saebea D. Exergoeconomics of hydrogen production from biomass air-steam gasification with methane co-feeding. *Energy Convers Manage* 2017;140:228-39.

[34] Zhang Y, Li B, Li H, Liu H. Thermodynamic evaluation of biomass gasification with air in autothermal gasifiers. *Thermochim Acta* 2011;519:65-71.

[35] Zhang Y, Li B, Li H, Zhang B. Exergy analysis of biomass utilization via steam gasification and partial oxidation. *Thermochim Acta* 2012;538:21-8.

[36] Zhang Y, Zhao Y, Gao X, Li B, Huang J. Energy and exergy analyses of syngas produced from rice husk gasification in an entrained flow reactor. *J Cleaner Prod* 2015;95:273-80.

[37] Shayan E, Zare V, Mirzaee I. Hydrogen production from biomass gasification; a theoretical comparison of using different gasification agents. *Energy Convers Manage* 2018;159:30-41.

[38] Abuadala A, Dincer I, Naterer GF. Exergy analysis of hydrogen production from biomass gasification. *Int J Hydrogen Energy* 2010;35:4981-90.

[39] Bilgen S, Kaygusuz K, Sari A. Second Law Analysis of Various Types of Coal and Woody Biomass in Turkey. *Energy Sources* 2004;26:1083-94.

[40] Ojeda K, Sánchez E, El-Halwagi M, Kafarov V. Exergy analysis and process integration of bioethanol production from acid pre-treated biomass: Comparison of SHF, SSF and SSCF pathways. *Chem Eng J* 2011;176-177:195-201.

[41] Li H, Zhang X, Liu L, Zeng R, Zhang G. Exergy and environmental assessments of

a novel trigeneration system taking biomass and solar energy as co-feeds. *Appl Therm Eng* 2016;104:697-706.

[42] Bridgwater AV. Review of fast pyrolysis of biomass and product upgrading. *Biomass Bioenergy* 2012;38:68-94.

[43] Roy D, Samanta S, Ghosh S. Techno-economic and environmental analyses of a biomass based system employing solid oxide fuel cell, externally fired gas turbine and organic Rankine cycle. *J Cleaner Prod* 2019;225:36-57.

[44] Jia J, Abudula A, Wei L, Sun B, Shi Y. Thermodynamic modeling of an integrated biomass gasification and solid oxide fuel cell system. *Renewable Energy* 2015;81:400-10.

[45] Toonssen R, Woudstra N, Verkooijen AHM. Decentralized generation of electricity with solid oxide fuel cells from centrally converted biomass. *Int J Hydrogen Energy* 2010;35:7594-607.

[46] Colpan CO, Hamdullahpur F, Dincer I, Yoo Y. Effect of gasification agent on the performance of solid oxide fuel cell and biomass gasification systems. *Int J Hydrogen Energy* 2010;35:5001-9.

[47] Gholamian E, Mahmoudi SMS, Zare V. Proposal, exergy analysis and optimization of a new biomass-based cogeneration system. *Appl Therm Eng* 2016;93:223-35.

[48] Karimi MH, Chitgar N, Emadi MA, Ahmadi P, Rosen MA. Performance assessment and optimization of a biomass-based solid oxide fuel cell and micro gas turbine system integrated with an organic Rankine cycle. *Int J Hydrogen Energy* 2020;45:6262-77.

[49] Mojaver P, Khalilarya S, Chitsaz A. Multi-objective optimization using response surface methodology and exergy analysis of a novel integrated biomass gasification,

solid oxide fuel cell and high-temperature sodium heat pipe system. *Appl Therm Eng* 2019;156:627-39.

[50] Habibollahzade A, Gholamian E, Behzadi A. Multi-objective optimization and comparative performance analysis of hybrid biomass-based solid oxide fuel cell/solid oxide electrolyzer cell/gas turbine using different gasification agents. *Appl Energy* 2019;233-234:985-1002.



## **CHAPTER 5: Flow Behaviors in A Small-Scale Biomass**

### **Gasifier**

#### **5.1 Introduction**

Electricity plays an important role in modern society. To date, fossil fuels, such as coal, crude oil and natural gas, still account for about 73% of energy resources for the world's electricity generation [1]. However, the declining of fossil fuels, increasing of global warming as well as environmental pollution are limiting the utilization of fossil fuel and forcing the world to find environmentally friendly alternatives for electricity generation in the future [2-4]. In recent decades, biomass energy has been attracted extensive attention from researchers and engineers and tried to be applied in electricity generation, due to its renewability and sustainability [5-7]. Especially, the utilization of biofuel is generally considered as a carbon neutral process since the carbon dioxide (CO<sub>2</sub>) released from biomass utilization can be fixed again by afforestation [8, 9].

Biomass energy shows a booming prospect in electricity generation. According to the report of IEA (International Energy Agency) [1], the world's electricity generation from biomass energy increased by about 394% from 1990 to 2018. Different from the fossil fuels, the biomass sources show a scattered geographical distribution, which results in high costs of collection and transportation [3]. In order to fully use the locally available biomass, small-scale biomass power generation system should be more suitable for the biomass energy applications [2]. To date, the small-scale biomass gasification-based power generation system has been commercialized and achieved a large market share [10]. On the other hand, the development of small-scale biomass

gasifiers is being limited by the tar, which can cause the fouling of downstream process equipment, such as engine. Generally, the syngas produced from biomass gasification is known to contain tar in the range of 0.01-160 g/Nm<sup>3</sup> [11]. In the large-scale gasification systems, the approaches of wet scrubbing with water-based or oil-based absorbents have been widely used to eliminate tar [12, 13]. However, these approaches are not suitable for the small-scale and low-cost systems, due to the difficulties of wastewater treatment or oil-based absorbents regeneration [11]. Therefore, a simple and highly efficient approach of tar removal is considered as the key issue in the design of small-scale biomass gasification power generation system. Recently, the tar removal by catalytic steam and/or CO<sub>2</sub> reforming have been concerned and tested [8, 14]. By the approach of reforming, tar can be not only removed, but also converted into syngas, improving product yields.

In addition to the tar removal, the different occurrence temperature ranges with different reaction rates of biomass pyrolysis, tar reforming and bio-char gasification processes in biomass gasification also should be considered. For example, biomass pyrolysis and tar reforming are relatively fast reaction processes whereas it has to take a long time for the complete steam gasification of bio-char at a high temperature (800-1000 °C) [15]. Moreover, some volatiles such as tar, light hydrocarbon gases and inorganic gases produced in the biomass pyrolysis process will hinder the gasification of char when the pyrolysis and gasification are carried out at the same reactor [16]. Thus, the spatial subdivision of those processes in biomass gasification can be adopted to realize the optimization of each conversion step and improve the whole performance [2].

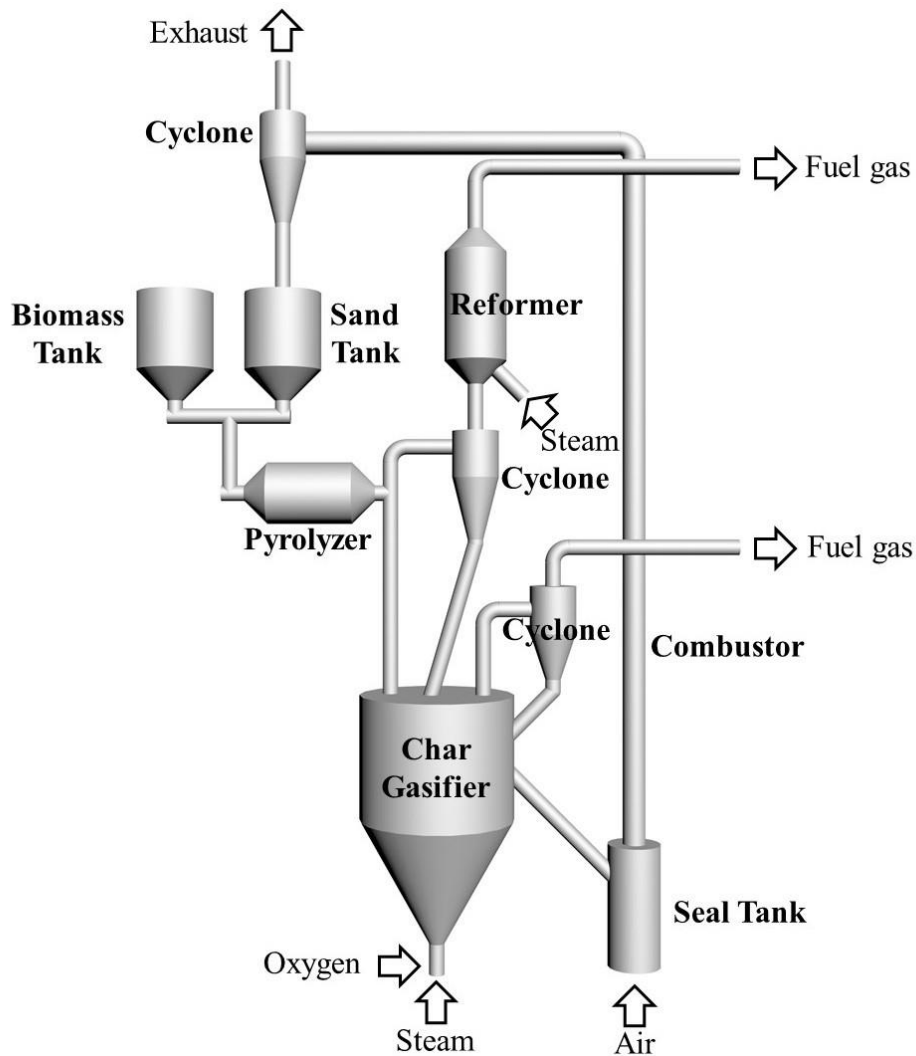


**Fig. 5-1.** Schematic diagram of apparatus.

In this study, a small-scale separated-type biomass gasification system (Fig. 5-1) for biomass power generation is proposed and assessed by numerical simulation. As shown in Fig. 5-1, this circulating fluidized bed (CFB) gasification system is composed of an auger pyrolyzer, a bubbling fluidized bed (BFB) char gasifier, a riser combustor and a fixed bed reformer. The biomass and the circulated hot silica sands are introduced into the auger pyrolyzer firstly. As the biomass is mixed with the hot silica sands along the auger reactor, it will be decomposed to volatiles and char. The volatiles go upwards to the reformer where the volatiles mix with steam and are catalytically converted to

syngas. Meanwhile, the char flows downwards to BFB and is self-heatedly gasified with oxygen and steam to syngas. The unreacted char overflows into riser combustor and is burned completely. The generated heat from the char combustion is carried by silica sands and recycled to the sand tank. And then, the hot circulated sands flow into the auger-type pyrolyzer and provide the heat for the biomass pyrolysis. The gas produced in the pyrolyzer, reformer, and char gasifier will be collected together and used as the fuel for the engine to generate electricity. About 1.25 kg/h (10 kg/day, 8 h/day) of biomass feeding rate is applied for electricity requirement of one or two families.

For a CFB system design, the seal between riser and BFB should be considered to avoid that the relatively high-pressure airflow used to transfer particles upwardly in the riser flow back into the BFB. In the present study, a configuration of siphon (Fig. 5-2a, case<sub>1</sub>) is applied to form a moving bed layer to realize the gas seal. To maintain the moving bed layer and guide particles to flow from the BFB to the riser, the  $(P_3 + P_4)$  should be slightly higher than  $(P_1 + P_2)$ . Herein,  $P_1$ ,  $P_2$ ,  $P_3$  and  $P_4$  are the pressures of outlet of BFB, moving bed layer, particle bed layer and inside BFB. However, the pressure fluctuation of particle bed layer is usually significant, resulting in a negative effect siphon-type gas seal. Thus, a two-stage gas seal design combined siphon configuration and seal tank (Fig. 5-2b, case<sub>2</sub>) also is proposed and investigated. In the design of seal tank, the air inlet of riser is located on one side of seal tank, and there is a partition which can guide the air to flow towards riser. In this study, the flow behaviors in the BFB and riser of a small-scale separated-type biomass gasification system with gas seal structures are simulated based on cold model. The objectives of this work are to characterize the hydrodynamics of the CFB-type small-scale biomass gasifier and to explore the possibilities to achieve a good gas seal between the BFB and riser.

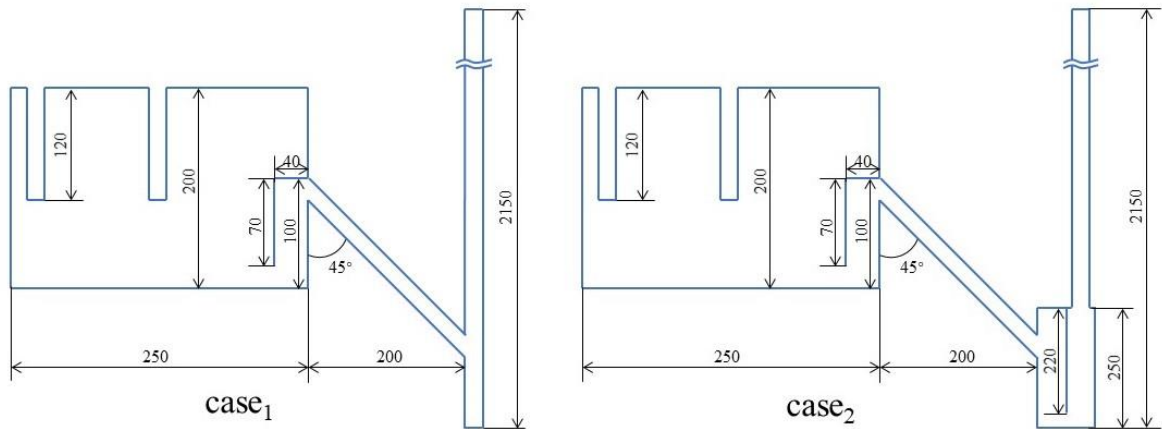


**Fig. 5-2.** Geometry and dimensions of gasification system with different gas seal types in the simulation.

## 5.2 Simulation methods

The small-scale separated-type biomass gasification system contains silica sand as the solids phase and air as the gas phase, respectively.

### 5.2.1 Mathematical model

The gas-solids flow behavior is simulated by using Eulerian-Eulerian two-fluid model incorporated with the kinetic theory of granular flow (KTGF). Herein, the k- $\epsilon$  model is used to describe the turbulence of gas, and the KTGF is used to describe the collision behavior of solid particles. The governing equations are summarized as follows (subscripts of g and s referred to gas and sand, respectively): [17-30]

The continuity equations of gas and solids phases,

$$\frac{\partial(\alpha_g \rho_g)}{\partial t} + \nabla(\alpha_g \rho_g \vec{v}_g) = 0, \quad (5-1)$$

$$\frac{\partial(\alpha_s \rho_s)}{\partial t} + \nabla \cdot (\alpha_s \rho_s \vec{v}_s) = 0, \quad (5-2)$$

Momentum conservation equations for gas and solids phases,

$$\frac{\partial}{\partial t} (\alpha_g \rho_g \vec{v}_g) + \nabla \cdot (\alpha_g \rho_g \vec{v}_g \vec{v}_g) = -\alpha_g \nabla p + \nabla \cdot \overline{\overline{\tau}}_g + K_{gs} (\vec{v}_s - \vec{v}_g) + \alpha_g \rho_g \vec{g}, \quad (5-3)$$

$$\frac{\partial}{\partial t} (\alpha_s \rho_s \vec{v}_s) + \nabla \cdot (\alpha_s \rho_s \vec{v}_s \vec{v}_s) = -\alpha_s \nabla p - \nabla p_s + \nabla \cdot \overline{\overline{\tau}}_s + K_{gs} (\vec{v}_g - \vec{v}_s) + \alpha_s \rho_s \vec{g}. \quad (5-4)$$

The turbulent kinetic energy and turbulent dissipation rate in the k-ε model are given as follows:

$$\frac{\partial}{\partial t} (\alpha_g \rho_g k_g) + \nabla \cdot (\alpha_g \rho_g k_g \vec{v}_g) = \nabla \cdot \left( \alpha_g \frac{\mu_{t,g}}{\sigma_k} \nabla k_g \right) + \alpha_g G_{k,g} - \alpha_g \rho_g \varepsilon_g + \alpha_g \rho_g \Pi_{k_g}, \quad (5-5)$$

$$\frac{\partial}{\partial t} (\alpha_g \rho_g \varepsilon_g) + \nabla \cdot (\alpha_g \rho_g \varepsilon_g \vec{v}_g) = \nabla \cdot \left( \alpha_g \frac{\mu_{t,g}}{\sigma_k} \nabla \varepsilon_g \right) + \alpha_g \frac{\varepsilon_g}{k_g} (C_{1\varepsilon} G_{k,g} - C_{2\varepsilon} \rho_g \varepsilon_g) + \alpha_g \rho_g \Pi_{\varepsilon_g}, \quad (5-6)$$

The concept of KTGF, which considers the conservation of particles velocity fluctuation energy, is used to close solids stress terms [30]. The motion of single particle in gas-solids flow is considered to be similar as the thermal motion of gas molecule. Herein, there is a random fluctuation of single particle, which is caused by collision of particles. Based on the random fluctuation of particle, the concept of “particle temperature” is proposed and adopted in the Gidaspow’s model [20].

$$\frac{3}{2} \left[ \frac{\partial}{\partial t} (\rho_s \alpha_s \Theta_s) + \nabla \cdot (\rho_s \alpha_s \vec{v}_s \Theta_s) \right] = \left( -p_s \overline{\overline{I}} + \overline{\overline{\tau}}_s \right) : \nabla \vec{v}_s + \nabla \cdot (k_{\Theta_s} \nabla \Theta_s) - \gamma_{\Theta_s} + \varphi_{gs}. \quad (5-7)$$

In order to accurately describe the interaction between gas and solids phases, Gidaspow’s drag force model is used to calculate the momentum transfer in this study [20]. The corresponding equations of drag coefficient are written as follows:

$$\text{at } \alpha_g > 0.8, K_{gs} = \frac{3}{4} C_D \frac{\alpha_s \alpha_g \rho_g |\vec{v}_s - \vec{v}_g|}{d_s} \alpha_g^{-2.65}, \quad (5-8)$$

$$\text{and at } \alpha_g \leq 0.8, K_{gs} = 150 \frac{\alpha_s (1 - \alpha_g) \mu_g}{\alpha_g d_s^2} + \frac{7}{4} \frac{\alpha_s \rho_g |\vec{v}_s - \vec{v}_g|}{d_s}. \quad (5-9)$$

$$C_D = \frac{24}{\alpha_g \text{Re}_s} \left[ 1 + 0.15 (\alpha_g \text{Re}_s)^{0.687} \right], \text{ for } \text{Re}_s > 1000, \quad (5-10)$$

$$C_D = 0.44, \text{ for } \text{Re}_s \leq 1000, \quad (5-11)$$

$$\text{and } \text{Re}_s = \frac{\rho_g d_s |\vec{v}_s - \vec{v}_g|}{\mu_g}. \quad (5-12)$$

Constitutive equations for the solids phase stress based on the kinetic theory concepts of Lun *et al.* [21] and widely applied in the CFD simulation studies. In this study, the following constitutive equations are used.

The closure for gas phase stress tensor,

$$\overline{\overline{\tau}}_g = \alpha_g \mu_g \left( \nabla \vec{v}_g + \nabla \vec{v}_g^T \right); \quad (5-13)$$

The closure for gas phase stress tensor,

$$\overline{\overline{\tau}}_s = \alpha_s \mu_s \left( \nabla \vec{v}_s + \nabla \vec{v}_s^T \right) + \alpha_s \left( \lambda_s - \frac{2}{3} \mu_s \right) \nabla \vec{v}_s \overline{\overline{I}}; \quad (5-14)$$

where, the bulk viscosity,

$$\lambda_s = \frac{4}{3} \alpha_s^2 \rho_s d_s g_0 (1 + e_s) \left( \frac{\Theta_s}{\pi} \right)^{1/2}; \quad (5-15)$$

in which, the radial distribution function,

$$g_0 = \left[ 1 - \left( \frac{\alpha_s}{\alpha_{s,\max}} \right)^{1/3} \right]^{-1}; \quad (5-16)$$

the solids shear viscosity,

$$\mu_s = \mu_{s,col} + \mu_{s,kin} + \mu_{s,fr}; \quad (5-17)$$

the solids collision viscosity,

$$\mu_{s,col} = \frac{4}{5} \alpha_s \rho_s d_s g_0 \cdot (1 + e_s) \cdot \left( \frac{\Theta_s}{\pi} \right)^{1/2}; \quad (5-18)$$

the kinetic viscosity (Gidasapow),

$$\mu_{s,kin} = \frac{10 \rho_s d_s (\Theta_s \pi)^{1/2}}{96 \alpha_s (1 + e_s) g_0} \left[ 1 + \frac{4}{5} g_0 \alpha_s \cdot (1 + e_s) \right]^2; \quad (5-19)$$

the solids frictional viscosity,

$$\mu_{s,fr} = \frac{p_s \sin \theta}{2 I_{2D}^{1/2}}; \quad (5-20)$$

the collision dissipation energy,

$$\gamma_{\Theta_s} = \frac{12 \cdot (1 - e_s^2) \cdot g_0}{d_s \sqrt{\pi}} \rho_s \alpha_s^2 \Theta_s^{3/2}; \quad (5-21)$$

and the solids pressure,

$$p_s = \alpha_s \rho_s \Theta_s + 2 \rho_s (1 + e_s) \alpha_s^2 g_0 \Theta_s. \quad (5-22)$$

## 5.2.2 Simulation conditions

Computational Fluid Dynamics commercial software FLUENT 20.0 is used to implement the Eulerian-Eulerian model. Herein, the phase coupled SIMPLE algorithm is adopted to achieve pressure and velocity coupling, and the second-order upwind scheme is applied to discretize the governing equations. Velocity-inlet and pressure-outlet boundary condition are applied at inlet and outlet of the downer, respectively. In addition, no-slip boundary condition of wall is applied for air. The detailed simulation



conditions and geometrical dimensions are shown in **Table 5-1**.

**Table 5-1.** Simulation parameters.

<b>Description</b>	<b>Value</b>
Solids mass flux ( $G_s$ )	6.63 kg/m <sup>2</sup> s
Particles density	2560 kg/m <sup>3</sup>
Particles diameter	122 $\mu$ m
Gas density	1.225kg/m <sup>3</sup>
Gas viscosity	1.7894 $\times 10^{-5}$ kg/m $\cdot$ s
Diameter of dense downer ( $D$ )	25-35 mm
Cone angle ( $\alpha$ )	30-75 $^\circ$
Superficial gas velocity	0.05 m/s for BFB 1.24 m/s for riser
Wall boundary conditions	No-slip for air, specular coefficient 0.001 for solids
Packing limit	0.63
Granular viscosity	Gidspow [20]
Granular bulk viscosity	Lun <i>et al.</i> [21]
Frictional viscosity	Schaeffer [27]
Angle of internal friction	30 $^\circ$
Granular temperature	Algebraic
Drag force	Gidspow [20]
Coefficient of restitution for particle- particle collisions	0.95

Gravitational acceleration	9.81 m/s <sup>2</sup>
Time steps	1×10 <sup>-5</sup> s
Convergence criteria	10 <sup>-3</sup>

---

### 5.2.3 Grid independence analysis

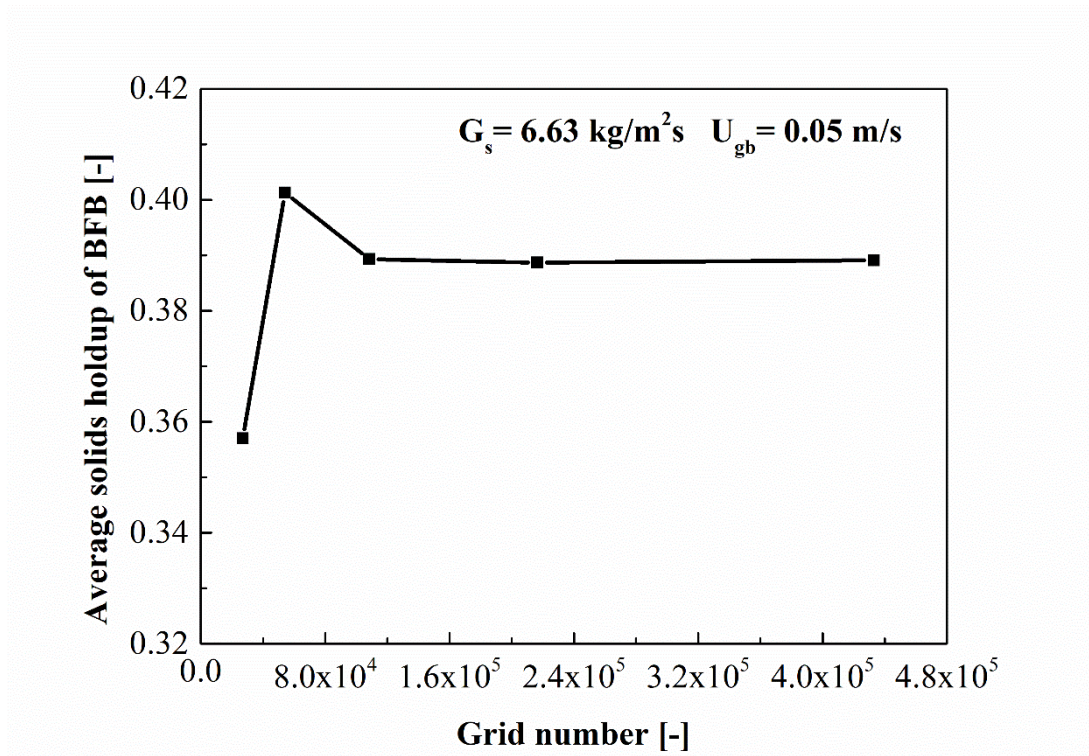


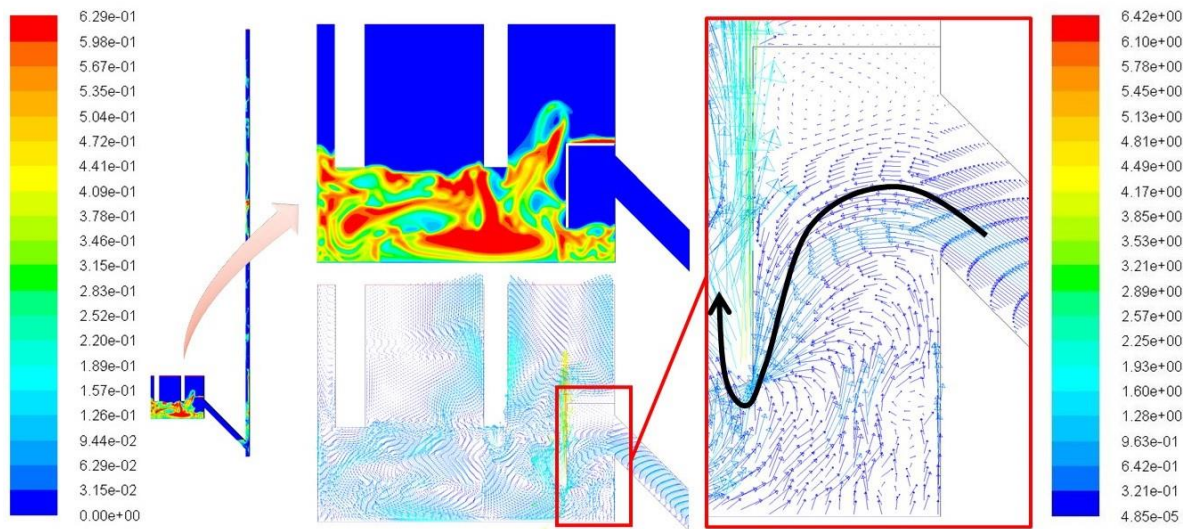
**Fig. 5-3.** Grid independence analysis.

The geometries with detail dimension of riser, BFB and gas seal structure showed in Fig. 5-2 are used to simulate gas-solids flow behavior. An unstructured grid is applied in the numerical simulations. It is well known that the dense grid can improve the simulation accuracy, but the workload of computers also increases substantially. Considering the balance of accuracy and the workload, the analysis of grid

independence is carried out firstly to obtain an appropriate grid scale for the flow behavior simulation. To avoid the negative impacts of grid number and size on accuracy, five grid dimensions (grid numbers: 27062, 54125, 108249, 216498, 432996) are tested. As shown in Fig. 5-3, with the increase of grids, simulated average solids holdups of BFB are close to 0.389. It should be noticed that the results are almost identical when the grids are over  $1 \times 10^5$ , indicating that these results of simulations are independent on the grid size.

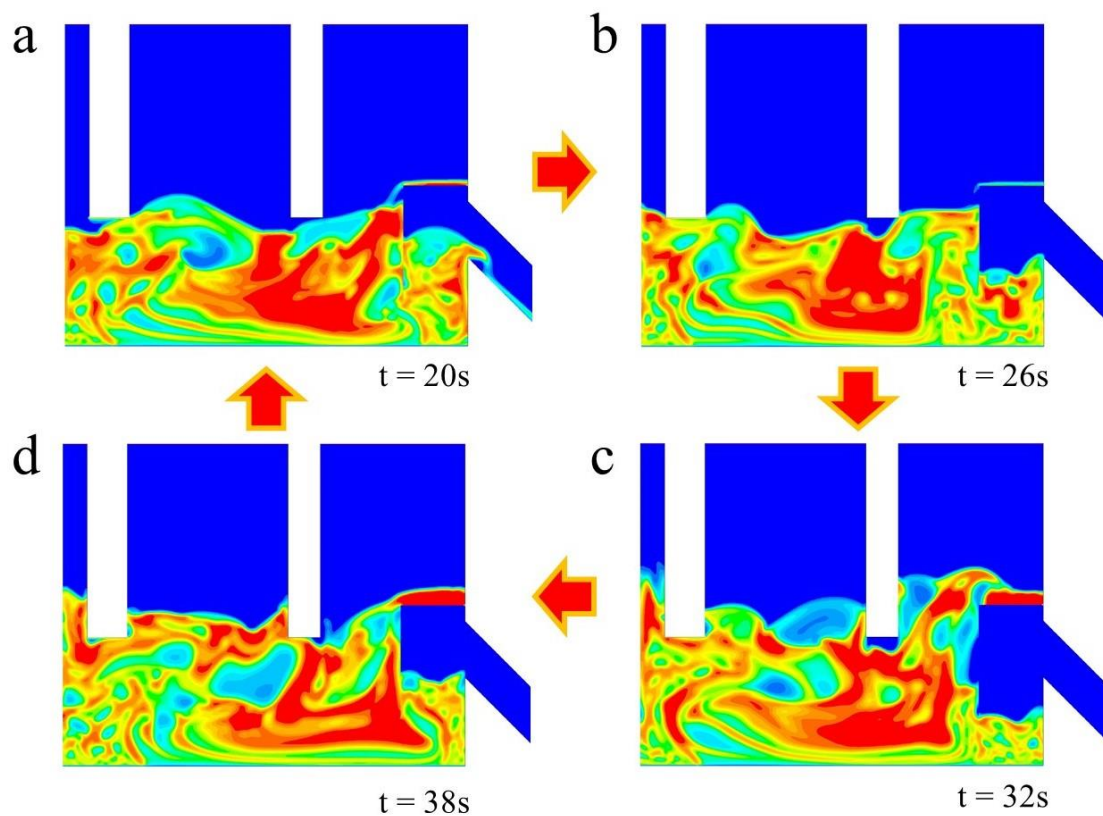
### **5.3 Results and discussion**

Fig. 5-4 shows the solids holdup distribution and airflow velocity vector of BFB with only siphon structure (case<sub>1</sub>), in which the values of solids holdup and velocity are represented by the colors and the arrows express the directions of airflows. As shown in Fig. 5-4, it is difficult to achieve the seal in the small-scale circulating fluidized bed with low solids flux. The air from riser rushes into BFB and mixes with solid particles. Same as steam, the air is also a common gasifying agent. The introduction of air can enhance oxidation in char gasification, causing a composition change of gasification products. Moreover, it should be noticed that the gas velocity can reach 3-5 m/s. According to the continuous medium hypothesis, the gas velocity should be increased with the decrease of the flow area. Due to most of flow areas occupied by particles, the air will accelerate after flowing into the BFB, resulting in some entrained particles by high-velocity air flow out from the gas outlet of BFB.



**Fig. 5-4.** Solids holdup distribution and airflow velocity vector of BFB with only siphon structure (case<sub>1</sub>).

As stated above, the formation of moving bed layer by the siphon is the key to block the airflow from riser to BFB. However, the low solids flux cannot maintain the intended pressure balance between BFB and riser. As shown in Fig. 5-5, the pressure of BFB is higher than that of relatively empty riser at first, making much particles enter to the riser smoothly. While, the pressure of particle bed layer in BFB decreases, since the mass flow of BFB outlet is higher than that of BFB inlet at the condition of low solids flux. Meanwhile, the pressure of riser increases rapidly due to the arrival of particles. The pressure change stops the particles flow from the BFB to riser, making particles flow show intermittent. Herein, the high pressure of riser promotes air to break through the moving bed layer and flows into BFB, until the pressure of riser decreases when the particles in the riser reach the top and outflow. The flow behaviors of BFB and riser present a special periodicity.



**Fig. 5-5.** The visual representations of periodic flow behaviors of BFB

Fig. 5-6 shows the solids holdup distribution and airflow velocity vector of BFB in case<sub>2</sub>. Under the action of the combination of siphon and seal tank, the moving bed layer can be maintained to realize gas seal. In the seal tank, the flow path allowing air flow from riser to BFB is very narrow due to the configuration of partition. Moreover, as shown in Fig. 5-6, some sand particles accumulate at the left side of seal tank, forming a resistance to airflow. Most of air is directed to the riser since a fluid usually tends to flow in the direction of less resistance. Although a small amount of air still flows into the outlet of BFB along the connection tube, the air velocity is too low to destroy the moving bed layer. And then, this part of air has to flow back to the riser.

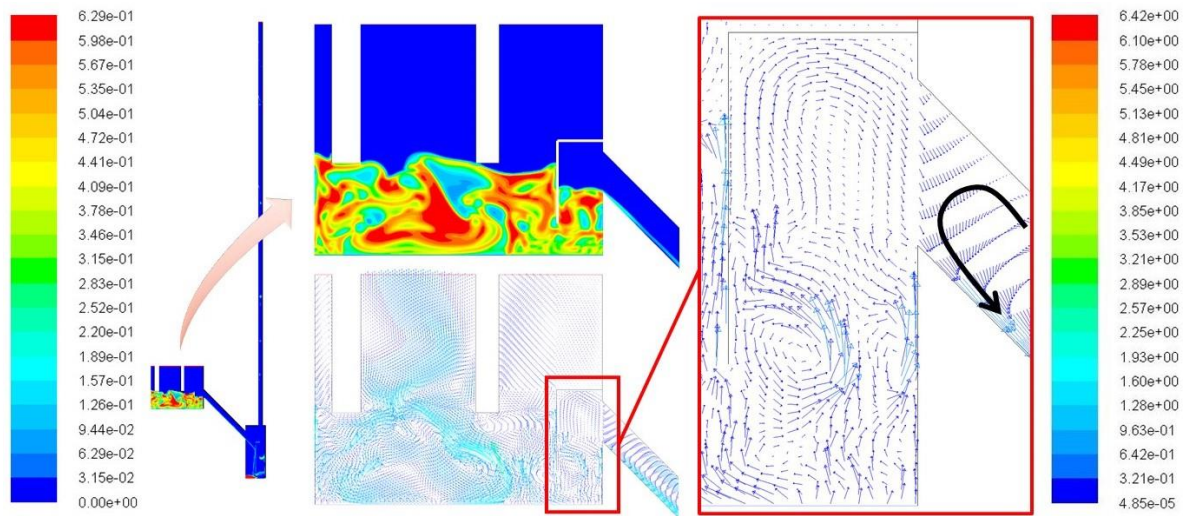


**Fig. 5-6.** Solids holdup distribution and airflow velocity vector of BFB with only siphon structure (case<sub>2</sub>).

## 5.4 Conclusions

In this study, the gas-solids flow behaviors of a small-scale separated-type biomass gasification system are studied and gas seal structures are assessed based on the cold model by using ANSYS Fluent 20.0 software. The direct feeding of biomass to the small-scale separated-type CFB gasifier for the power generation opens a door for the effective conversion of biomass to energy and avoidance of tar problem. In the case of only siphon structure, due to the low solids mass flux, the intended pressure balance between BFB and riser cannot be maintained, causing that air of riser breaks through the moving bed layer and flows into the BFB sometimes. The flow behaviors of BFB and riser present a special periodicity. Compared with only siphon structure, the combination of siphon configuration and seal tank shows better gas seal performance. Because of the resistance of configuration of partition and sand particles accumulated at left side of seal tank, the injected air is directed to the riser. In the future, the modeling

of both heat transfer and reaction processes to further evaluate gasifier performance.

This proposed system should be promising for the biomass-based power generation.

## Nomenclature

### Notations

$c_v$	coefficient of variation
$C_D$	drag coefficient, dimensionless
$C_\mu, C_{1\varepsilon}, C_{2\varepsilon}$	coefficients in turbulence model, dimensionless
$e_s$	particle-particle restitution coefficient, dimensionless
$e_w$	particle-wall restitution coefficient, dimensionless
$g$	gravitational acceleration, $\text{m/s}^2$
$g_0$	radial distribution coefficient, dimensionless
$G_{k, m}$	production of turbulent kinetic energy, dimensionless
$G_s$	circulating flux of solid particles, $\text{kg/m}^2\text{s}$
$\bar{I}$	stress tensor, dimensionless
$I_{2D}$	second invariant of the deviatoric stress tensor, dimensionless
$k$	turbulence kinetic energy tensor, dimensionless
$k_{\Theta_s}$	diffusion coefficient for granular energy, $\text{kg/s}\cdot\text{m}$
$K_{gs}$	interphase exchange coefficient, $\text{kg}\cdot\text{m}^2/\text{s}$
$n$	sample size of radial distribution of solids holdup
$p$	pressure, Pa
$p_s$	particulate phase pressure, Pa

$P_1$	pressure of outlet of BFB, Pa
$P_2$	pressure of moving bed layer, Pa
$P_3$	pressure of particle bed layer, Pa
$P_4$	pressure of inside BFB, Pa
$p_f$	pressure for wall friction, Pa
$Re$	relative Reynolds number, dimensionless
$Re_s$	particle Reynolds number, dimensionless
$t$	time, s
$v_g$	gas velocity, m/s
$v_s$	solids velocity, m/s

### ***Greek letters***

$\alpha_g$	volume fraction of gas phase, dimensionless
$\alpha_s$	volume fraction of solids phase, dimensionless
$\alpha_{s,ave}$	average volume fraction of solids phase, dimensionless
$\varepsilon$	turbulence dissipation rate, $m^2/s^3$
$\varphi_{gs}$	dissipation of granular energy resulting from the fluctuating forcer, $m^2/s^2$
$\mu_g$	viscosity of gas phase, Pa·s
$\mu_s$	solids shear viscosity, Pa·s
$\mu_{s,col}$	solids collisional viscosity, Pa·s
$\mu_{s,kin}$	solids kinetic viscosity, Pa·s
$\mu_{s,fr}$	solids frictional viscosity, Pa·s
$\mu_{t,m}$	frictional viscosity of system m, Pa·s
$\Pi_{kg}$	source term caused by influence of solids phase on turbulent kinetic



	energy, $\text{m}^2/\text{s}^3$
$\Pi_{eg}$	source term caused by influence of solids phase on turbulence energy dissipation rate, $\text{m}^2/\text{s}^4$
$\sigma_\varepsilon$	granular kinetic theory parameter (kinetic viscosity), $\text{Pa}\cdot\text{s}$
$\sigma(\alpha_s)$	standard deviation of volume fraction of solids phase, dimensionless
$\theta$	angle of internal friction, degrees
$\Theta_s$	granular temperature, $\text{m}^2/\text{s}^2$
$\gamma_{\Theta_s}$	collisional dissipation of energy, $\text{m}^2/\text{s}^2$
$\overline{\tau}_g$	shear stress of gas phase, $\text{N}/\text{m}^2$
$\overline{\tau}_s$	shear stress of solids phase, $\text{N}/\text{m}^2$
$\lambda_s$	solids bulk viscosity, $\text{Pa}\cdot\text{s}$
$\rho_g$	gas density, $\text{kg}/\text{m}^3$
$\rho_s$	solids density, $\text{kg}/\text{m}^3$

## References

- [1] IEA, World Energy Outlook 2020, <https://www.iea.org/reports/world-energy-outlook-2020#>; 2020 [accessed in 12 Jun 2020]
- [2] Zhao Z, Situmorang YA, An P, Yang J, Hao X, Rizkiana J, et al. A biomass-based small-scale power generation system with energy/exergy recuperation. *Energy Convers Manage* 2021;227:113623.
- [3] Situmorang YA, Zhao Z, Yoshida A, Abudula A, Guan G. Small-scale biomass gasification systems for power generation (<200 kW class): A review. *Renew Sustain*

Energy Rev 2020;117.

[4] Wang H, Lei Z, Zhang X, Zhou B, Peng J. A review of deep learning for renewable energy forecasting. *Energy Convers Manage* 2019;198:111799.

[5] Detchusananard T, Sharma S, Maréchal F, Arpornwichanop A. Multi-objective optimization of sorption enhanced steam biomass gasification with solid oxide fuel cell. *Energy Convers Manage* 2019;182:412-29.

[6] Knutsson P, Maric J, Knutsson J, Larsson A, Breitholtz C, Seemann M. Potassium speciation and distribution for the K<sub>2</sub>CO<sub>3</sub> additive-induced activation/deactivation of olivine during gasification of woody biomass. *Appl Energy* 2019;248:538-44.

[7] Li T, Niu Y, Wang L, Shaddix C, Løvås T. High temperature gasification of high heating-rate chars using a flat-flame reactor. *Appl Energy* 2018;227:100-7.

[8] Guan G, Kaewpanha M, Hao X, Abudula A. Catalytic steam reforming of biomass tar: Prospects and challenges. *Renew Sustain Energy Rev* 2016;58:450-61.

[9] Zhao Z, Situmorang YA, An P, Chaihad N, Wang J, Hao X, et al. Hydrogen production from catalytic steam reforming of bio-oils: a critical review. *Chemical Engineering Technology* 2020;43:625-40.

[10] Dong L, Liu H, Riffat S. Development of small-scale and micro-scale biomass-fuelled CHP systems – A literature review. *Appl Therm Eng* 2009;29:2119-26.

[11] Madav V, Das D, Kumar M, Surwade M, Parikh PP, Sethi V. Studies for removal of tar from producer gas in small scale biomass gasifiers using biodiesel. *Biomass Bioenergy* 2019;123:123-33.

[12] Jansen JC, Jönsson K, Hagman M. Biological detoxification of tar-water. *Water Sci Technol* 2002;46:59-65.

[13] Zwart R, Van der Drift A, Bos A, Visser H, Cieplik M, Könemann H. Oil-based gas

washing—Flexible tar removal for high-efficient production of clean heat and power as well as sustainable fuels and chemicals. *Environ Prog Sustain Energy* 2009;28:324-35.

[14] Liu L, Zhang Z, Das S, Kawi S. Reforming of tar from biomass gasification in a hybrid catalysis-plasma system: A review. *Appl Catal, B* 2019;250:250-72.

[15] Dupont C, Boissonnet G, Seiler J-M, Gauthier P, Schweich D. Study about the kinetic processes of biomass steam gasification. *Fuel* 2007;86:32-40.

[16] Guan G, Fushimi C, Tsutsumi A, Ishizuka M, Matsuda S, Hatano H, et al. High-density circulating fluidized bed gasifier for advanced IGCC/IGFC—Advantages and challenges. *Particuology* 2010;8:602-6.

[17] Shu Z, Fan C, Li S, Wang J. Multifluid modeling of coal pyrolysis in a downer reactor. *Ind Eng Chem Res* 2016;55:2634-45.

[18] Chen X-Z, Shi D-P, Gao X, Luo Z-H. A fundamental CFD study of the gas–solid flow field in fluidized bed polymerization reactors. *Powder Technol* 2011;205:276-88.

[19] Peng G, Dong P, Li Z, Wang J, Lin W. Eulerian simulation of gas–solid flow in a countercurrent downer. *Chem Eng J* 2013;230:406-14.

[20] Ding J, Gidaspow D. A bubbling fluidization model using kinetic theory of granular flow. *AIChE J* 1990;36:523-38.

[21] Lun C, Savage SB, Jeffrey D, Chepuriniy N. Kinetic theories for granular flow: inelastic particles in Couette flow and slightly inelastic particles in a general flowfield. *J Fluid Mech* 1984;140:223-56.

[22] Syamlal M, Rogers W, OBrien TJ. MFIx documentation theory guide. USDOE Morgantown Energy Technology Center, WV (United States); 1993.

[23] Chapman S, Cowling TG, Burnett D. The mathematical theory of non-uniform gases: an account of the kinetic theory of viscosity, thermal conduction and diffusion in

gases. Cambridge: Cambridge university press; 1990.

[24] Geldart D. Gas fluidization technology. United States 1986.

[25] Shi D-P, Luo Z-H, Zheng Z-W. Numerical simulation of liquid–solid two-phase flow in a tubular loop polymerization reactor. Powder Technol 2010;198:135-43.

[26] Gidaspow D. Multiphase flow and fluidization: continuum and kinetic theory descriptions. San Diego: Academic press; 1994.

[27] Schaeffer DG. Instability in the evolution equations describing incompressible granular flow. J Differ Equations 1987;66:19-50.

[28] Bradshaw P, Cebeci T, Whitelaw JH. Engineering calculation methods for turbulent flow. London: Academic Press; 1981.

[29] Chen CJ. Fundamentals of turbulence modelling. Florida: CRC Press; 1997.

[30] Taghipour F, Ellis N, Wong C. Experimental and computational study of gas–solid fluidized bed hydrodynamics. Chem Eng Sci 2005;60:6857-67.

## CHAPTER 6: A Separated-Type Autothermal CH<sub>4</sub> Dry

### Reforming System with Exergy Recuperation

#### 6.1 Introduction

The climate is deteriorating due to the global warming caused by greenhouse gases such as carbon dioxide (CO<sub>2</sub>), water vapor (H<sub>2</sub>O), methane (CH<sub>4</sub>), ozone (O<sub>3</sub>), nitrous oxide (N<sub>2</sub>O) and so on. According to the report of Intergovernmental Panel on Climate Change (IPCC), the average temperature of earth has already reached 1°C above the pre-industrial level, resulting in warmer ocean, more acidic and less productive [1]. CO<sub>2</sub> is the second greenhouse gas after water vapor and contributes to about 26% of greenhouse effect [2]. International Energy Agency (IEA) reports that the total global CO<sub>2</sub> emission from energy source is approximately 33.5 Gt per year [3]. Due to the unstable and uneven temporal and spatial distributions of water vapor, water vapor is generally not taken into consideration when planning measures to refrain the greenhouse effect. Therefore, the application of CO<sub>2</sub> capture and storage (CCS) and CO<sub>2</sub> conversion and utilization have become the key to mitigate the global warming. Nowadays, about 40 Mt of CO<sub>2</sub> is captured from power and industrial facilities each year [4]. However, the conventional technology of CO<sub>2</sub> capture and storage in subsurface formations greatly increases the industrial cost, causing it to lose economic competitiveness [5]. National Energy Technology Laboratory (NETL) has reported that integrating of CO<sub>2</sub> capture unit (e.g., monoethanolamine as the solvent of absorption) into coal combustion power plant would result in cost approximately 80 US dollar per

ton CO<sub>2</sub> and decrease the total efficiency by about 10.6% [6]. In order to reduce the CCS cost, one of the ways is to develop effective CO<sub>2</sub> utilization technology.

Currently, as one of the CO<sub>2</sub> utilization technologies, dry reforming of methane (DRM) has attracted increasingly extensive attention, by which two abundant greenhouse gases can be consumed and converted to high value-added syngas with a ratio of H<sub>2</sub>/CO close to 1. This H<sub>2</sub>/CO ratio is suitable for Fischer-Tropsch (F-T) synthesis of long chain hydrocarbons or direct utilization in solid oxide fuel cells as the fuel [7-9]. Moreover, compared with other CH<sub>4</sub> reforming processes, DRM technology can decrease the operating cost by about 20% [7].

The DRM process is endothermic and will be thermodynamically impeded when the operating temperature is lower than 642 °C [10]. Although the catalysts developed in the laboratory can achieve the chemical conversion actively at relatively low temperature, they are always not well adopted in the industrial scale. The industrial-scale equipment often works in a high space velocity condition and keeps a continuous production and meanwhile, the deposited coke on the catalysts always cover the active sites on surface so that the catalysts deactivated rapidly [11-13]. Moreover, the sintering, low mechanical strength and high cost also hinder the industrial application of the man-made catalysts [13-15]. Therefore, the low-cost and abundant natural catalysts such as olivine and dolomite are widely used in various industrial DRM systems nowadays. For a DRM system with those natural catalysts, it is usually necessary to maintain high temperature condition to achieve highly-efficient conversion. While, combination of DRM with partial oxidation of methane (POM) can realize an autothermal dry reforming of methane (ATDRM) process with less energy supply from outside [16-20]. In the conventional ATDRM system, the mixture of CH<sub>4</sub>, CO<sub>2</sub> and O<sub>2</sub> is injected into a

same reactor directly, in which the thermal energy produced by the POM can promote the endothermic DRM reaction. However, the introduction of O<sub>2</sub> to the DRM reactor will cause lower CO<sub>2</sub> conversion since the CO<sub>2</sub> can be also generated from CH<sub>4</sub> oxidation inevitably [21, 22]. In addition, the produced H<sub>2</sub>O from CH<sub>4</sub> oxidation will shift the equilibrium of water-gas shift reaction (WGSR) towards the direction of CO<sub>2</sub> production.

In order to eliminate the negative effect of the products of POM on the DRM reaction and further improve the CO<sub>2</sub> conversion efficiency, a separated-type ATDRM (S-ATDRM) system with the spatial subdivision of reforming and partial oxidation processes is proposed as a solution. To date, the conventional S-ATDRM used a tube-and-shell fixed bed reactor system, in which heat generated from the POM or burner is transferred into the DRM reactor through the wall of DRM reactor [23, 24]. Some researchers also tried to separate DRM and POM processes using the membrane-type reactors [25, 26]. However, since the catalysts are fixedly packed in the two reactors, the heat transfer efficiency is always reduced and the temperature distribution is also uneven, leading to a low conversion efficiency in the center region of reactor while the catalysts located near the wall are easy to be sintered. Moreover, difficulties in catalysts regeneration and exchange also limit the application of the conventional S-ATDRM for continuous industrial production. Thus, considering stable and efficient heat transfer and maximizing the catalyst performance and regeneration, herein, a circulating fluidized bed (CFB) is proposed to realize the optimization of each conversion step and eliminate the negative interaction between the DRM and POM processes.

Although various researches on the S-ATDRM system have been performed, a S-ATDRM system which separates DRM and POM processes by a circulating fluidized

bed has not yet been reported. Moreover, a thorough analysis of energy and energy consumptions and especially the exergy flow among the components of the S-ATDRM system has not been described in details. Such analysis is important to understand the thermodynamic mechanism, helping to increase the CO<sub>2</sub> conversion in a condition with a high energy efficiency. In this work, a novel S-ATDRM system is proposed and simulated for the first time, in which the DRM combined with POM is performed in a circulating fluidized bed with exergy recuperation to eliminate the negative effect of the products of CH<sub>4</sub> partial oxidation on the DRM reaction and further improve the CO<sub>2</sub> conversion efficiency.

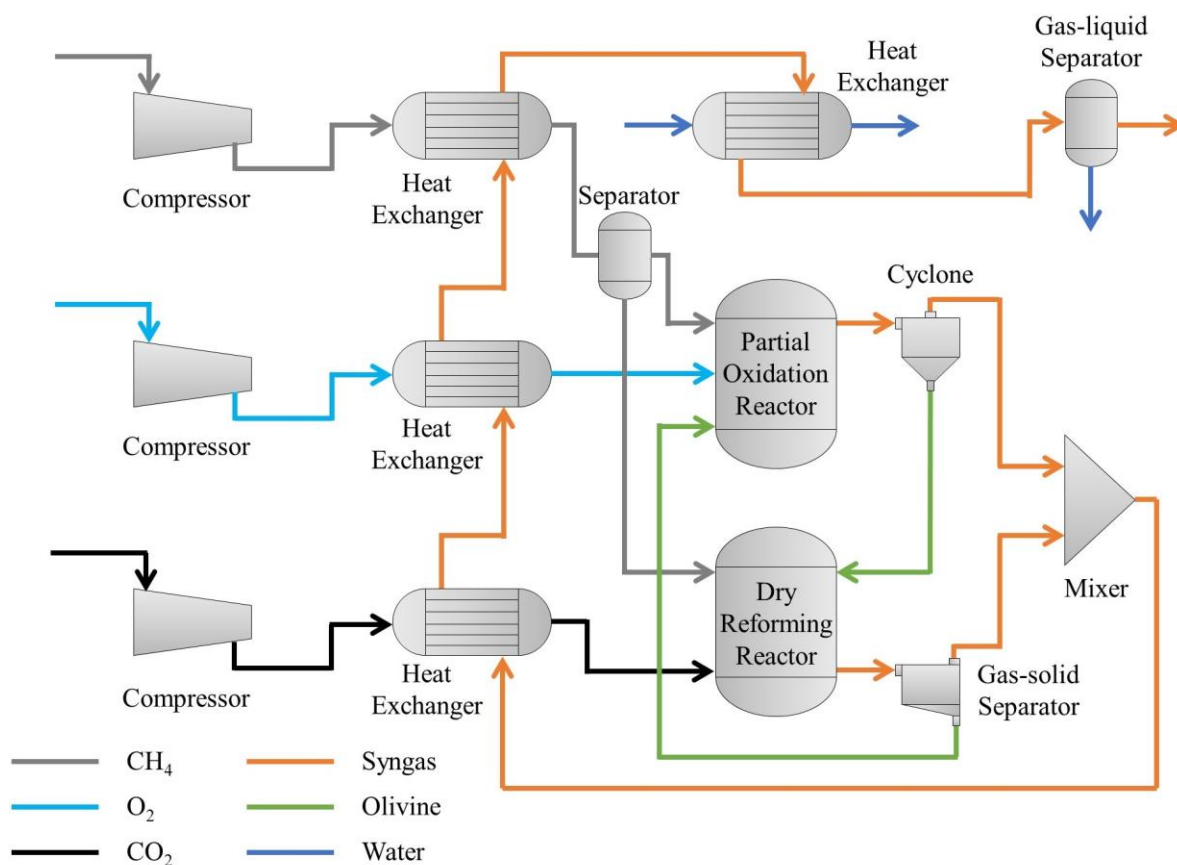
## 6.2 System description and simulation method

Fig. 6-1 presents flowsheet of this novel S-ATDRM system with a circulating fluidized bed and exergy recuperation, which mainly includes a DRM reactor, a POM reactor, several compressors and heat exchangers, and a gas-liquid separator. **Table 6-1** summarizes the possible reactions in this S-ATDRM system, which is mainly operated as follows:

- (1) CH<sub>4</sub> is assigned to two parts and fed into the DRM reactor and POM reactor respectively after pre-heating;
- (2) In the POM reactor, CH<sub>4</sub> mixes with O<sub>2</sub> and olivine catalysts and is partial oxidized to syngas;
- (3) The hot olivine catalysts flow into DRM reactor to provide heat and catalysis for the DRM process;
- (4) In the DRM reactor, CO<sub>2</sub> and CH<sub>4</sub> are converted to high value-added syngas;



(5) The syngas from the DRM and POM reactors are cooled down to 25 °C by heat exchangers and separated from water. While, the heat released from syngas cooling process is used to pre-heat CO<sub>2</sub>, CH<sub>4</sub> and O<sub>2</sub> gases.



**Fig. 6-1.** Schematic of the proposed S-ATDRM system with a circulating fluidized bed and exergy recuperation.

Fig. 6-2 illustrates the flowsheet of the conventional ATDRM system, in which the DRM and POM reactions are carried out in the same reactor. To compare the performances of the proposed S-ATDRM system with the conventional ATDRM one, the same flowsheets are designed except reactors.

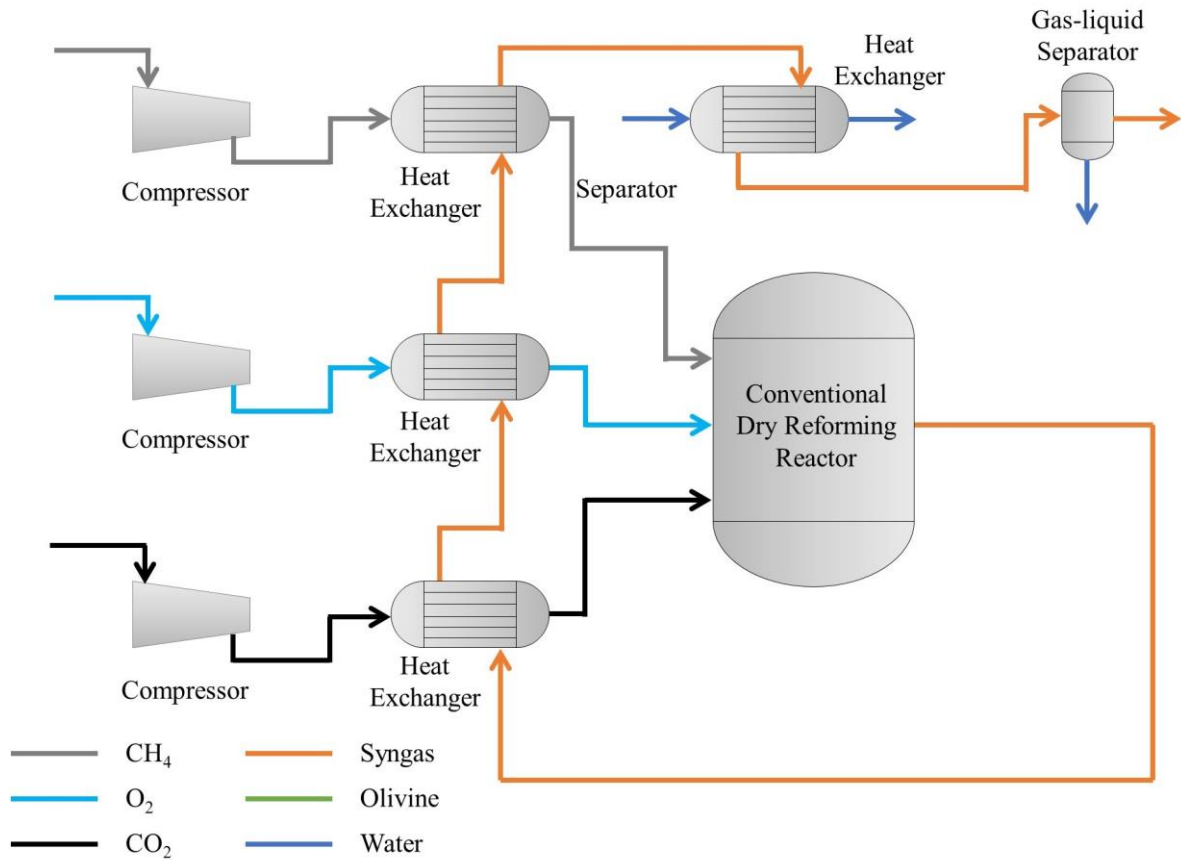


**Fig. 6-2.** Schematic of the conventional ATDRM system.

In this work, Aspen Plus software (version 10.0) is applied for the total system simulation, in which the solids processing model is applied. The selected physical property model used for the calculation of the thermodynamic and transport properties of the conventional components is Peng-Robinson equation of state with Boston-Mathias modification (PR-BM model). In addition, some essential simulation assumptions for the units and their simulation blocks in Aspen Plus are summarized in **Table 6-2**. Herein, some basic assumptions for the simulation are listed as follows:

- (1) The operating conditions of all units are steady-state.
- (2) The heat loss in the system by the wall of each unit is not considered;
- (3) The reactors can reach the equilibrium states;

- (4) All feedings are in the standard condition;
- (5) The dead state (standard condition) for standard chemical exergy, specific enthalpy, specific entropy is absolute pressure  $P_0 = 1$  atm and normal temperature  $T_0 = 25$  °C.

**Table 6-1** Reactions in the S-ATDRM system.

Reaction	Chemical reaction equation	$\Delta H_{298K}$ (kJ/mol)	Eq.
Methane reforming	$CO_2$ $CH_4 + CO_2 \leftrightarrow 2H_2 + 2CO$	247	(6-1)
Methane decomposition	$CH_4 \leftrightarrow 2H_2 + C$	74.9	(6-2)
Boudouard reaction	$2CO \leftrightarrow C + CO_2$	-172	(6-3)
Methane oxidation	partial $CH_4 + 1/2O_2 \rightarrow 2H_2 + CO$	-36	(6-4)
Methane oxidation	total $CH_4 + 2O_2 \rightarrow 2H_2O + CO_2$	-803	(6-5)
Carbon monoxide oxidation	$CO + 0.5O_2 \rightarrow CO_2$	-284	(6-6)
Methanation reaction	$CO_2 + 4H_2 \rightarrow CH_4 + 2H_2O$	-165	(6-7)
Methane reforming	steam $CH_4 + H_2O \leftrightarrow 3H_2 + CO$	206	(6-8)
Water-gas reaction	shift $CO + H_2O \leftrightarrow H_2 + CO_2$	-41	(6-9)

**Table 6-2** Essential simulation assumptions and models in the proposed S-ATDRM system.

<b>Unit</b>	<b>Simulation assumption</b>	<b>Simulation model</b>
S-ATDRM system		
Compressor	CH <sub>4</sub> feed rate: 67.5 kmol/h CO <sub>2</sub> feed rate: 21.0-80.9 kmol/h O <sub>2</sub> feed rate: 20.8-39.8 kmol/h* Discharge pressure: 2.013 bar Compressor efficiency: 80% Mechanical and electrical efficiency: 98%	Compr block (compressor model)
Dry reforming reactor	Temperature: 700-100 °C Pressure: 2.013 bar Circulating olivine flow rate: 18000 kg/h	RGibbs block
Partial oxidation reactor	Pressure: 2.013 bar Heat duty: 0	RGibbs block
Heat-exchanger	Approach point: 10 °C Pinch point: 10 °C	HeatX blocks
Condenser	Approach point: 10 °C Pinch point: 10 °C Cold water feed rate: 1000 kmol/h	Heater blocks
Conventional ATDRM system		

Compressor	CH <sub>4</sub> feed rate: 67.5 kmol/h CO <sub>2</sub> feed rate: 21.0-80.9 kmol/h O <sub>2</sub> feed rate: 20.8-39.8 kmol/h Discharge pressure: 2.013 bar Compressor efficiency: 80% Mechanical and electrical efficiency: 98%	Compr block (compressor model)
Conventional dry reforming reactor	Pressure: 2.013 bar Heat duty: 0	RGibbs block
Heat-exchanger	Approach point: 10 °C Pinch point: 10 °C	HeatX blocks
Condenser	Cold water feed rate: 1000 kmol/h Approach point: 10 °C Pinch point: 10 °C	Heater blocks

---

\*The ratio of O<sub>2</sub> to CH<sub>4</sub> fed into partial oxidation reactor is 1.

### 6.3 Exergy analysis

In thermodynamics, energy analysis is usually used to understand energy flow, transformation and storage, which can evaluate the performance of a system. However, as we all know, not all energy can be fully utilized in a system. Therefore, it is insufficient to evaluate a system only using energy analysis. In contrast, exergy analysis based on the second law of thermodynamics can be used for the assessment of energy conversion quality since the entropy changes occurred in the system are considered [27].

Exergy is defined as the maximum useful work from a thermal system, and the total exergy of a stream can be expressed as the sum of four types of exergy: physical exergy, chemical exergy, kinetic exergy and potential exergy [28-30], which can be written as:

$$Ex = Ex_{ph} + Ex_{ch} + Ex_{ki} + Ex_{ep} \quad (10)$$

Herein, the kinetic exergy and potential exergy are usually neglected because of their very low values closing to zero [30]. Thus, the Eq. (6-10) can be simplified to:

$$Ex = Ex_{ph} + Ex_{ch} \quad (6-11)$$

The physical energy of a stream of conventional component is always calculated by the enthalpy and entropy [28, 31]:

$$Ex_{ph} = \sum_{i=1} \dot{n}_i [(h - h_0) - T_0 (s - s_0)] \quad (6-12)$$

where,

$$h = h_0 + \int_{T_0}^T C_p dT \quad (6-13)$$

$$s = s_0 + \int_{T_0}^T \frac{C_p}{T} dT - R \ln \frac{P}{P_0} \quad (6-14)$$

In the Eqs. (6-13) and (6-14), the  $C_p$  is the specific heat capacity of gas at the constant pressure, which can be written as [32]:

$$C_p = a + bT + cT^2 + dT^3 \quad (6-15)$$

where  $a$ ,  $b$ ,  $c$ , and  $d$  are empirical coefficients for the specific heat capacity at the constant pressure with a temperature range of 273-1800 K. **Table 6-3** summarizes the empirical coefficients used in this work.

The chemical exergy of a stream of conventional component can be calculated from the following equation [28, 31]:

$$Ex_{ch} = \sum_{i=1} \dot{n}_i (ex_{ch,i} + RT_0 \ln x_i) \quad (6-16)$$

where, the  $ex_{ch,i}$  is specific chemical exergy of each component at the dead state as summarized in **Table 6-4**.

**Table 6-3** Empirical coefficients of specific heat capacity at the constant pressure [33].

Component	$a$	$b (\times 10^{-2})$	$c (\times 10^{-5})$	$d (\times 10^{-9})$	Temperature range (K)
H <sub>2</sub>	29.11	-0.1916	0.4003	-0.8704	273-1800
CO	28.16	0.1675	0.5327	-2.222	273-1800
CO <sub>2</sub>	22.26	5.981	-3.501	7.469	273-1800
CH <sub>4</sub>	19.89	5.024	1.269	-11.01	273-1800
O <sub>2</sub>	25.48	1.520	-0.7155	1.312	273-1800
H <sub>2</sub> O	32.24	0.1923	1.055	-3.595	273-1800

**Table 6-4** Specific chemical exergies of the components at the dead state [30, 34].

Component	Exergy (kJ/kmol)
H <sub>2</sub>	236100
CO	275100
CO <sub>2</sub>	19870
CH <sub>4</sub>	831650
O <sub>2</sub>	3970
H <sub>2</sub> O (gas)	9500
H <sub>2</sub> O (liquid)	900

The exergy is always destroyed and converted to energy during an irreversible process according to the second law of thermodynamics. For a unit or the total system, the exergy destruction can be expressed as [27]:

$$Ex_D = Ex_{input} - Ex_{output} \quad (6-17)$$

As such, the exergy efficiency of total system can be calculated by the following equation:

$$\eta_{Ex} = \frac{Ex_{syngas}}{Ex_{CO_2} + Ex_{CH_4} + Ex_{O_2} + Ex_{electricity,input}} \times 100\% \quad (6-18)$$

## 6.4 Results and discussion

### 6.4.1 Sensitivity analysis of S-ATDRM system.

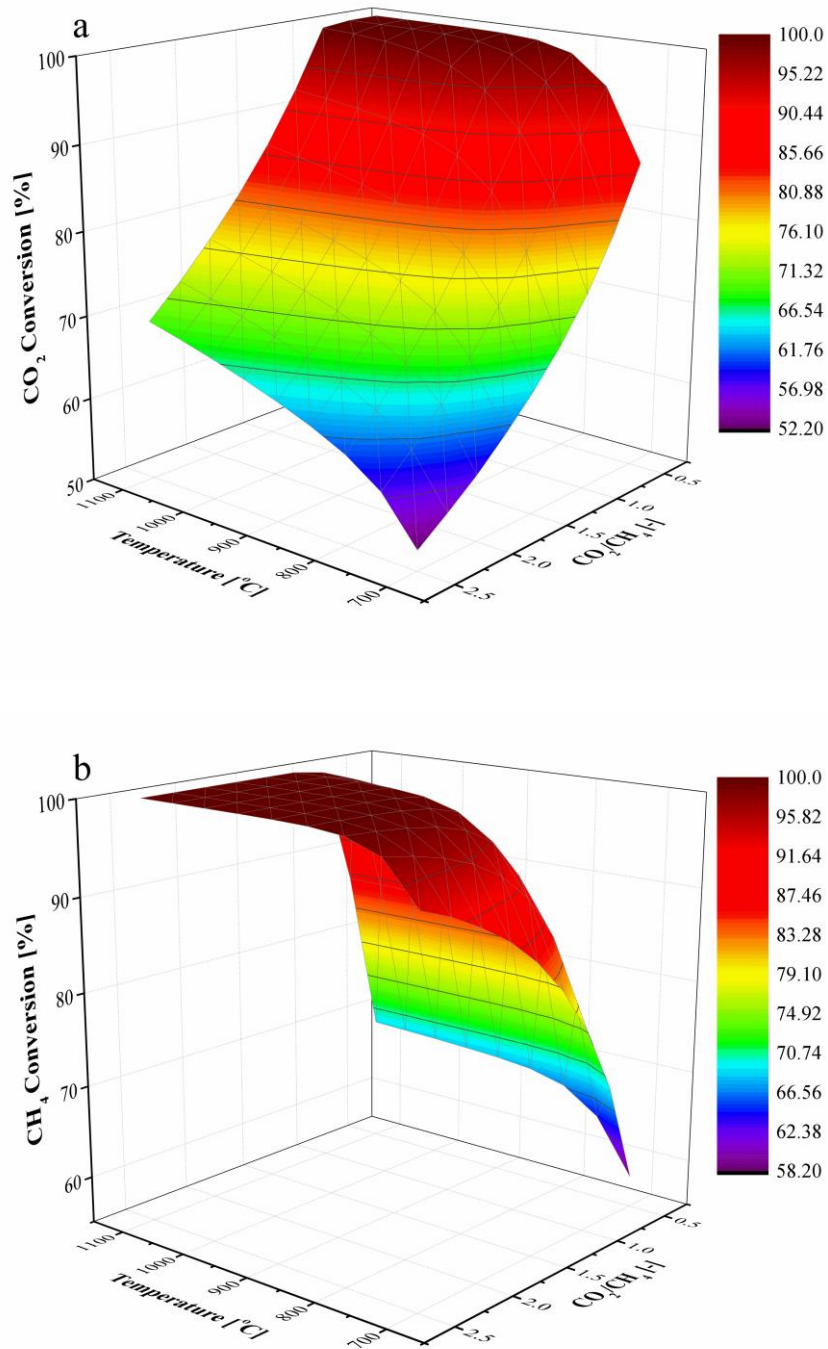
In this S-ATDRM system, the DRM can be considered as the main part for the conversion of CO<sub>2</sub> into syngas. To investigate the effects of operating conditions on the S-ATDRM process and achieve higher CO<sub>2</sub> and CH<sub>4</sub> conversion rates, the detailed sensitivity analyses are implemented by the Aspen Plus simulation. In this study, the DRM temperature is varied in the range of 850-1100 °C while the ratio of carbon dioxide to methane (CO<sub>2</sub>/CH<sub>4</sub>) is set in the range of 0.5-2.5. As shown in Fig. 6-1, since the heat needed in the DRM is provided from the POM reactor by the olivine catalyst particles as the heat carrier, the DRM temperature can be adjusted by the assignment of methane.

Fig. 6-3(a) shows the effects of the operating temperature and CO<sub>2</sub>/CH<sub>4</sub> ratio on the conversion of CO<sub>2</sub> in the DRM reactor. As seen, the high temperature significantly favors the conversion of CO<sub>2</sub> and the equilibrium conversion of CO<sub>2</sub> reaches the



maximum values at the temperature between 1000 and 1100 °C for all CO<sub>2</sub>/CH<sub>4</sub> ratios. Herein, the increase of temperature can enhance the endothermic DRM reaction (Eq. (6-1)) to increase the CO<sub>2</sub> conversion within the considered temperature range. Moreover, the higher temperature and the H<sub>2</sub> produced from the DRM reaction can shift the equilibrium of endothermic WGS reaction (Eq. (6-9)) to the direction of CO and H<sub>2</sub>O, also resulting in a positive effect on CO<sub>2</sub> conversion. In addition to high temperature, high CH<sub>4</sub> input also can increase the equilibrium conversion of CO<sub>2</sub>. At the condition of low CO<sub>2</sub>/CH<sub>4</sub> ratio, it is observed that the CO<sub>2</sub> is a limiting reactant from Eq. (6-1). When the DRM temperature is higher than 950 °C and the CO<sub>2</sub>/CH<sub>4</sub> ratio is less than 1, the CO<sub>2</sub> can be converted almost completely. Conversely, with the increase of CO<sub>2</sub>/CH<sub>4</sub> ratio, CH<sub>4</sub> intensively plays a role as the limiting reactant, leading to a dramatical decrease of CO<sub>2</sub> conversion.

The effects of operating temperature and CO<sub>2</sub>/CH<sub>4</sub> ratios on the conversion of CH<sub>4</sub> in the DRM reactor are shown in Fig. 6-3(b). It can be seen that the conversion of CH<sub>4</sub> increases dramatically with the increase of DRM temperature for all CO<sub>2</sub>/CH<sub>4</sub> ratios. However, when the temperature goes up over 800 °C, the conversion of CH<sub>4</sub> increases slowly up to the complete conversion. The increase of CO<sub>2</sub>/CH<sub>4</sub> ratio results in a CH<sub>4</sub> conversion trend similar to temperature increase trend. The conversion of CH<sub>4</sub> increases dramatically with the increasing of CO<sub>2</sub>/CH<sub>4</sub> ratio up to 1, beyond which the conversion of CH<sub>4</sub> increases smoothly. When the CO<sub>2</sub>/CH<sub>4</sub> ratio is less than 1, the CO<sub>2</sub> becomes to the limiting reactant, leading to an incomplete CH<sub>4</sub> conversion. In addition, compared with CO<sub>2</sub> conversion, the CH<sub>4</sub> can be converted more easily.



**Fig. 6-3.** Effects of operating condition on DRM: a) CO<sub>2</sub> conversion, b) CH<sub>4</sub> conversion.

The performance of this S-ATDRM process is also evaluated by exergy efficiency.

Fig. 6-4 depicts the effects of different operating conditions on the exergy efficiency of

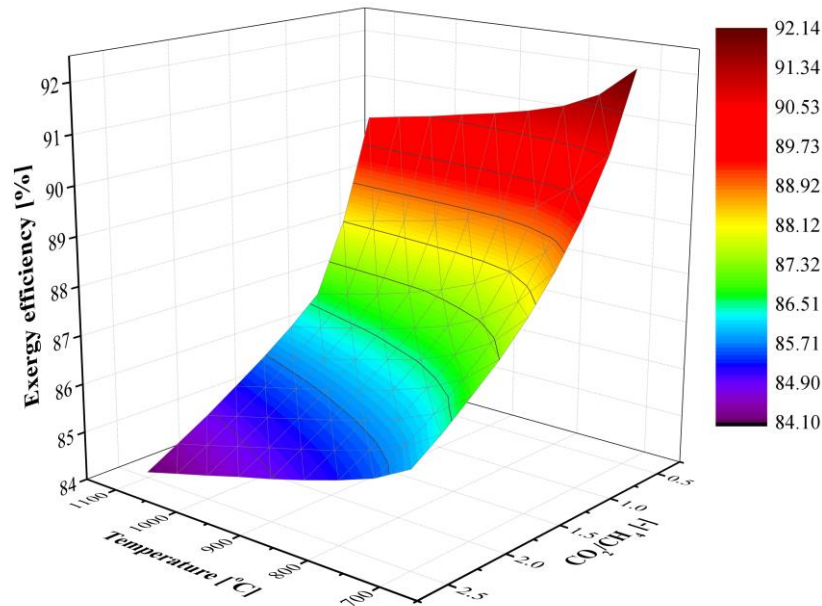


**Fig. 6-4.** Effect of operating condition in DRM on the exergy efficiency of total system.

total system. Within the considered operating temperatures and CO<sub>2</sub>/CH<sub>4</sub> ratios of the DRM, the exergy efficiencies are in the range of 84.1-92.1%. The exergy efficiency decreases with the increase of operating temperature as well as CO<sub>2</sub>/CH<sub>4</sub> ratio in the DRM reactor, indicating that a relatively lower temperature as well as a low CO<sub>2</sub>/CH<sub>4</sub> ratio condition could result in higher working ability for syngas production. On the other hand, in order to achieve a higher temperature condition for the DRM reactor, more heat is necessary to be provided. While, at a condition of high operating temperature with a high CO<sub>2</sub>/CH<sub>4</sub> ratio, the equilibrium of WGSR is shifted to CO and H<sub>2</sub>O, needing to absorb more heat. As such, more CH<sub>4</sub> has to be assigned to the POM reactor, which results in a lower exergy efficiency since the irreversible exothermic oxidation process can cause a large amount of exergy destruction [29]. Moreover, more physical exergy cannot be recuperated by heat exchangers and released in the condenser

at higher reaction temperature, also leading to the decrease of exergy efficiency. As a result, considering the almost complete conversion of  $\text{CO}_2$  and  $\text{CH}_4$  and the maximization of exergy efficiency, the DRM reactor of proposed S-ATDRM system should work at the operating condition of  $950\text{ }^\circ\text{C}$  with a  $\text{CO}_2/\text{CH}_4$  ratio of 1.

#### **6.4.2 Comparison of this S-ATDRM system with the conventional ATDRM system**

In order to assess the advantages of this novel S-ATDRM system in  $\text{CO}_2$  conversion, a detailed comparison of it with the conventional ATDRM system is implemented by simulation. Fig. 6-5 illustrates the detailed model built in Aspen Plus software and working states of these two systems at the operating condition of  $950\text{ }^\circ\text{C}$  and  $\text{CO}_2/\text{CH}_4 = 1$ . In this case, the feeding rates of  $\text{CO}_2$ ,  $\text{O}_2$  and  $\text{CH}_4$  are 31.74, 35.76 and 67.5 kmol/h, respectively.

A comparison of the syngas produced from the S-ATDRM and conventional ATDRM systems is illustrated in Fig. 6-6. One can see that the conversions of  $\text{CO}_2$  are 24.31 and 20.73 kmol/h for this novel S-ATDRM and the conventional ATDRM systems, respectively. That is, this novel separated-type design achieves an increase of about 11.3% in  $\text{CO}_2$  conversion. While, as shown in Figs. 6-5 and 6-6, this novel S-ATDRM system results in more  $\text{H}_2\text{O}$  production mainly from  $\text{CH}_4$  oxidation, but less  $\text{H}_2$ . In addition, the temperature of POM reactor is higher than that of conventional DRM reactor, indicating that the generation of  $\text{CO}_2$  from WGSR (Eq. (6-9)) is more difficult in this novel S-ATDRM system. Moreover, the  $\text{CO}_2$  partial pressure in the conventional DRM reactor is lower than that of this S-ATDRM system, also resulting in the lower  $\text{CO}_2$  conversion in the conventional ATDRM system.

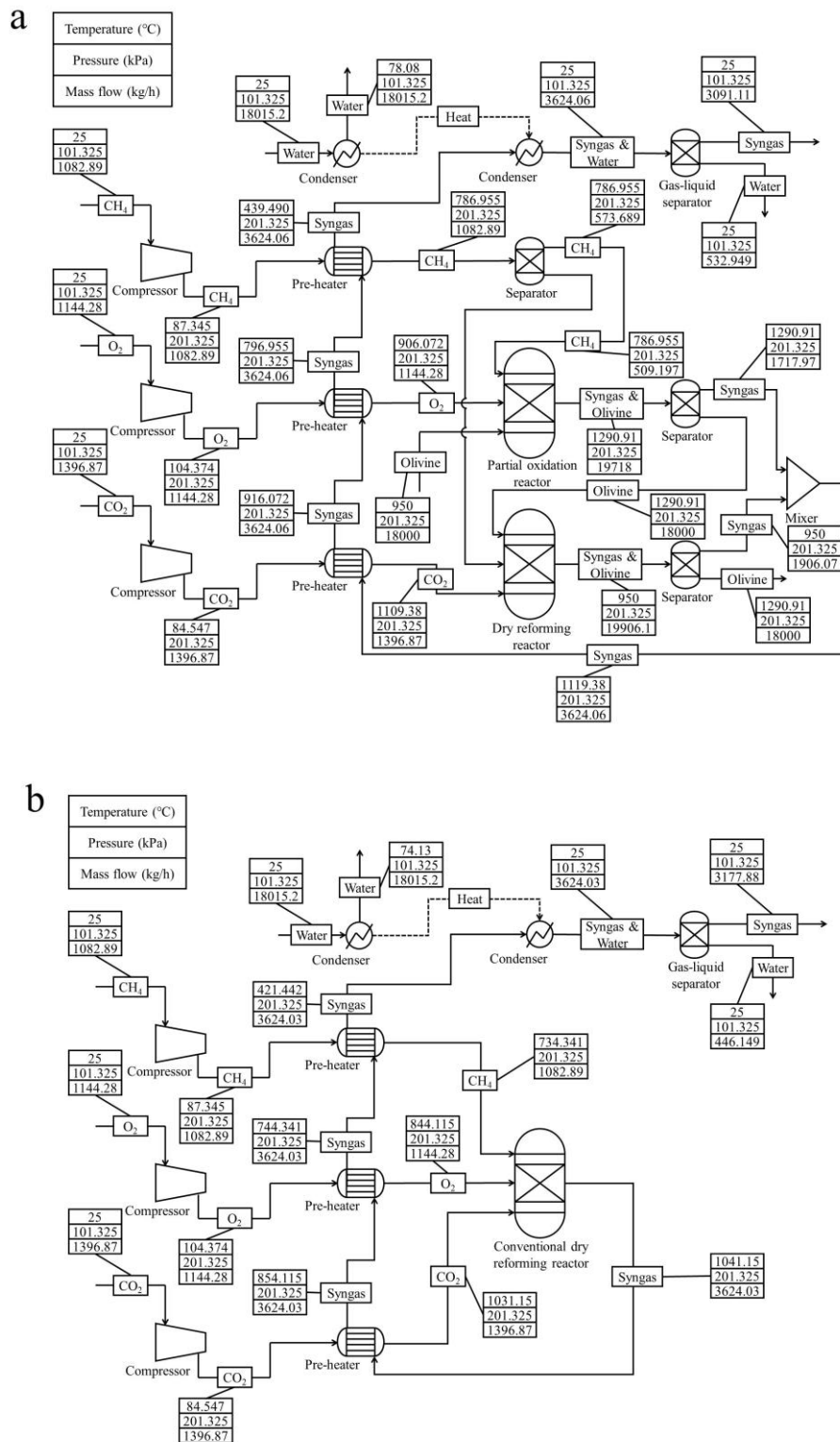


**Fig. 6-5.** Detailed flowsheets of the system in Aspen Plus software: a) S-ATDRM system, b) conventional ATDRM system.

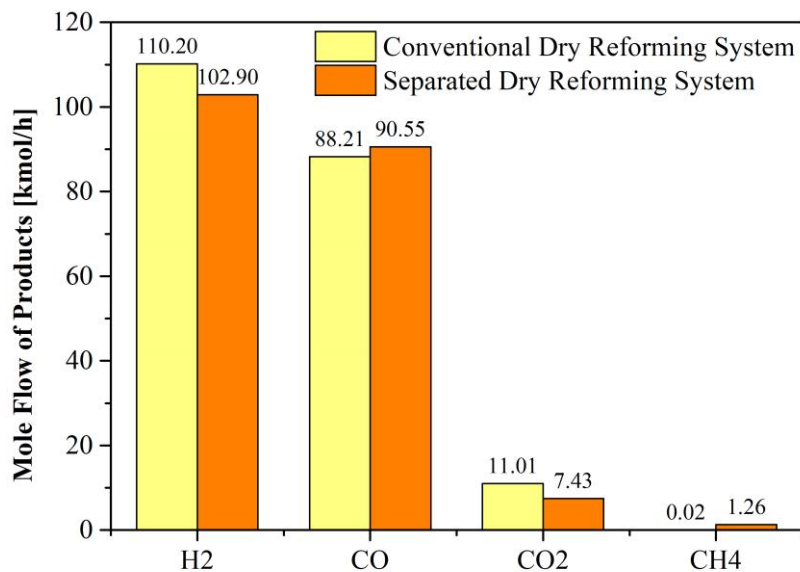


**Fig. 6-6.** Products of this novel S-ATDRM and the conventional ATDRM systems.

In thermodynamics, the Grassmann diagram is generally used to show the results of exergy analysis by depicting the exergy flows for the evaluation of system performance, in which the directions of flows are represented by the arrows, and the width expresses the relative amount of exergy. Fig. 6-7 illustrates the Grassmann diagrams of the novel S-ATDRM and conventional ATDRM systems at the condition shown in Fig. 6-5. As shown in Fig. 6-7(a), the input of 15593.4 kW exergy from CH<sub>4</sub> can result in a syngas output of 13880.1 kW exergy by using this S-ATDRM system. The total exergy destruction is approximately 1713.3 kW, of which approximately 1343.7 kW is caused by ATDRM reactions. The exergy destruction of the DRM process is only about 262.2 kW. However, due to the irreversible exothermic oxidation process, the POM reactor contributes the largest exergy destruction (1081.5 kW), which accounts for about 63.1% of the total exergy loss. In the exergy output of POM reactor, about

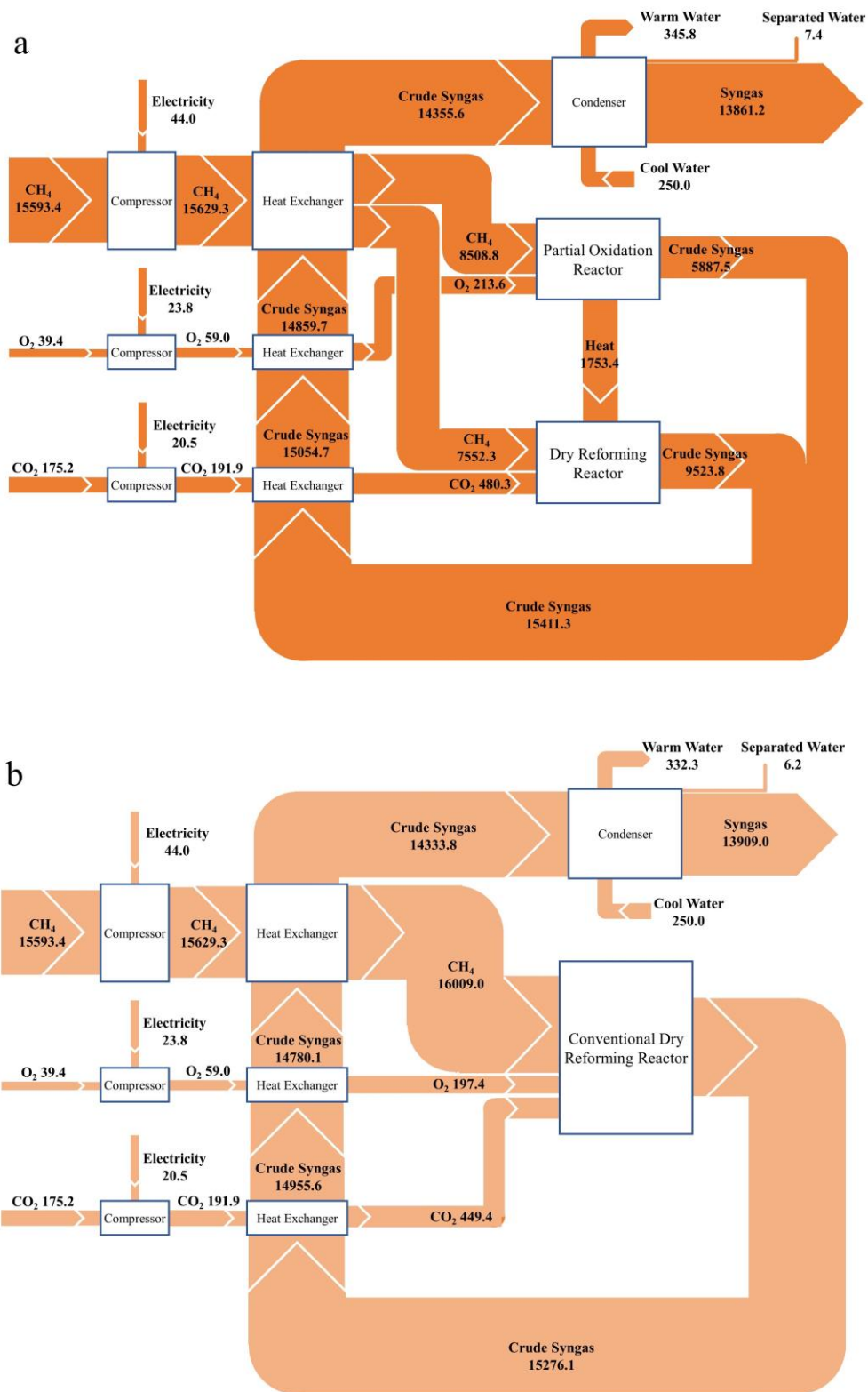


**Fig. 6-7.** Grassmann diagram: a) the separated-type ATDRM system, b) the conventional ATDRM system. (Exergy flows are expressed in kW.)

1753.4 kW is provided for the DRM reactor by olivine catalyst particles to support the CO<sub>2</sub> conversion. The total exergy of crude syngas generated from DRM and POM reactors is approximately 15411.3 kW, of which about 1055.7 kW of physical exergy is recuperated by those heat exchangers and reused in the S-ATDRM system to avoid exergy loss and improve the exergy efficiency. After delivering the physical exergy for the pre-heating of CO<sub>2</sub>, O<sub>2</sub> and CH<sub>4</sub>, 468.1 kW of exergy is lost during the condensation process. Due to the relatively low temperature, the latent heat released during the condensation process cannot be recuperated and reused. Under the actions of these heat exchangers, the exergy efficiency of total S-ATDRM system reaches as high as 87.2%.

As shown in Fig. 6-7(b), the conventional ATDRM system can achieve a syngas output of 13909.0 kW exergy at the same feeding condition as the S-ATDRM system. The exergy efficiency of the conventional ATDRM system can reach 87.3%, which is slightly higher than that of the S-ATDRM system. In the conventional DRM reactor, a crude syngas stream with 15276.1 kW of exergy can be obtained with a destroy of about 1379.7 kW exergy in the ATDRM reactions. From the crude syngas stream, about 942.3 kW of physical exergy can be recuperated by the heat exchangers, and reused. As shown in Fig. 6-5, the temperature of produced syngas of the conventional ATDRM system is lower than that of the S-ATDRM system, leading to the lower physical exergy recuperation. After exergy recuperation, about 418.6 kW of exergy is lost during the condensation process. Notably, compared with the conventional ATDRM system, the proposed S-ATDRM system shows almost the same performance in aspect of exergy efficiency, however, the research objective of CO<sub>2</sub> conversion can be substantially increased by about 11.3%.



## 6.5 Conclusions

In summary, a novel S-ATDRM system with a circulating fluidized bed and exergy recuperation is proposed and simulated, in which the DRM combining with POM was realized by a circulating fluidized bed. In order to obtain the optimal operating conditions, the effects of operating temperature and  $\text{CO}_2/\text{CH}_4$  ratio of DRM reactor on the conversion of  $\text{CO}_2$  and  $\text{CH}_4$  as well as the total system exergy efficiency are investigated in details. Based on the second law of thermodynamics, the Grassmann diagrams used for exergy analyses are drawn to illustrate the exergy flows. The main results are achieved as follows:

- (1) With the increase of temperature in the DRM reactor of the proposed S-ATDRM system, the conversion of  $\text{CO}_2$  and  $\text{CH}_4$  increase but the exergy efficiency decreases. At the condition with a relatively lower  $\text{CO}_2/\text{CH}_4$  ratio, the high  $\text{CO}_2$  conversion and exergy efficiency can be realized easily, however, some  $\text{CH}_4$  will remain in the products. Considering the complete conversions of  $\text{CO}_2$  and  $\text{CH}_4$  simultaneously and the maximization of exergy efficiency, the DRM reactor should work at a operating condition of  $950\text{ }^\circ\text{C}$  and  $\text{CO}_2/\text{CH}_4 = 1$ .
- (2) The novel S-ATDRM system can achieve an exergy efficiency of 87.2%. To increase the exergy efficiency, about 1055.7 kW of exergy is recuperated from the crude syngas cooling process and reused for the pre-heating of  $\text{CO}_2$ ,  $\text{O}_2$  and  $\text{CH}_4$ . In this system, the largest exergy destruction occurs in the POM reactor, which accounts for about 63.1% of the total exergy loss. Compared with the conventional ATDRM system, the exergy of this S-ATDRM system is slightly lower, however, the  $\text{CO}_2$  conversion can be substantially increased by about 11.3%.

## Nomenclature

### *Notations*

$a, b, c, d$	empirical coefficients (-)
$C_p$	constant pressure specific heat capacity (kJ/kmol·K)
$ex$	standard exergy (kJ/kmol)
$Ex$	exergy (kJ/kg)
$h$	specific enthalpy (kJ/kmol)
$\dot{n}$	component molar flow rate (kmol/s)
$P$	pressure (Pa)
$R$	universal gas constant (kJ/kmol·K)
$s$	specific entropy (kJ/kmol·K)
$T$	temperature (K)
$x$	molar fraction of gas component (-)

### *Greek letters*

$\eta$	efficiency (%)
--------	----------------

### *Subscripts*

$ch$	chemical
$D$	destruction
$ep$	potential
$Ex$	exergy
$i$	component
$ki$	kinetic

<i>ph</i>	physical
<i>0</i>	standard condition (dead state)
<i>Acronym</i>	
<i>ATDRM</i>	autothermal dry reforming of methane
<i>CCS</i>	carbon dioxide capture and storage
<i>CFB</i>	Circulating fluidized bed
<i>DRM</i>	dry reforming of methane
<i>POM</i>	partial oxidation of methane
<i>PR-BM</i>	Peng-Robinson equation of state with Boston-Mathias modifications
<i>S-ATDRM</i>	separated-type autothermal dry reforming of methane
<i>WGSR</i>	water-gas shift reaction

## References

- [1] IPCC, Choices made now are critical for the future of our ocean and cryosphere, <https://www.ipcc.ch/2019/09/25/srocc-press-release/>; 2019 [accessed in 12 Jun 2020]
- [2] Kiehl JT, Trenberth KE. Earth's Annual Global Mean Energy Budget. Bull Am Meteorol Soc 1997;78:197-208.
- [3] IEA, Data and statistics: CO<sub>2</sub> emissions, <https://www.iea.org/data-and-statistics/?country=WORLD&fuel=CO2%20emissions&indicator=CO2BySource>; 2020 [accessed in 12 Jun 2020]
- [4] IEA, Carbon capture, utilisation and storage, <https://www.iea.org/fuels-and-technologies/carbon-capture-utilisation-and-storage>; 2020 [accessed in 12 Jun 2020]

- [5] Farajzadeh R, Eftekhari AA, Dafnomilis G, Lake LW, Bruining J. On the sustainability of CO<sub>2</sub> storage through CO<sub>2</sub> – Enhanced oil recovery. *Appl Energy* 2020;261:114467.
- [6] Song C, Liu Q, Ji N, Deng S, Zhao J, Li Y, et al. Alternative pathways for efficient CO<sub>2</sub> capture by hybrid processes—A review. *Renew Sustain Energy Rev* 2018;82:215-31.
- [7] Wei T, Jia L, Luo J-L, Chi B, Pu J, Li J. CO<sub>2</sub> dry reforming of CH<sub>4</sub> with Sr and Ni co-doped LaCrO<sub>3</sub> perovskite catalysts. *Appl Surf Sci* 2020;506.
- [8] Li K, Chang X, Pei C, Li X, Chen S, Zhang X, et al. Ordered mesoporous Ni/La<sub>2</sub>O<sub>3</sub> catalysts with interfacial synergism towards CO<sub>2</sub> activation in dry reforming of methane. *Appl Catal, B* 2019;259.
- [9] Lino AVP, Calderon YNC, Mastelaro VR, Assaf EM, Assaf JM. Syngas for Fischer-Tropsch synthesis by methane tri-reforming using nickel supported on MgAl<sub>2</sub>O<sub>4</sub> promoted with Zr, Ce and Ce-Zr. *Appl Surf Sci* 2019;481:747-60.
- [10] Izquierdo-Colorado A, Dębek R, Da Costa P, Gálvez ME. Excess-methane dry and oxidative reforming on Ni-containing hydrotalcite-derived catalysts for biogas upgrading into synthesis gas. *Int J Hydrogen Energy* 2018;43:11981-9.
- [11] Jang WJ, Shim JO, Kim HM, Yoo SY, Roh HS. A review on dry reforming of methane in aspect of catalytic properties. *Catal Today* 2019;324:15-26.
- [12] Abdurashheed A, Jalil AA, Gambo Y, Ibrahim M, Hambali HU, Shahul Hamid MY. A review on catalyst development for dry reforming of methane to syngas: Recent advances. *Renew Sustain Energy Rev* 2019;108:175-93.
- [13] Zhang G, Liu J, Xu Y, Sun Y. A review of CH<sub>4</sub>CO<sub>2</sub> reforming to synthesis gas over Ni-based catalysts in recent years (2010–2017). *Int J Hydrogen Energy* 2018;43:15030-

54.

[14] Aziz MAA, Setiabudi HD, Teh LP, Annuar NHR, Jalil AA. A review of heterogeneous catalysts for syngas production via dry reforming. *J Taiwan Inst Chem Eng* 2019;101:139-58.

[15] Agrafiotis C, von Storch H, Roeb M, Sattler C. Solar thermal reforming of methane feedstocks for hydrogen and syngas production—A review. *Renew Sustain Energy Rev* 2014;29:656-82.

[16] Halabi M, de Croon M, van der Schaaf J, Cobden P, Schouten J. Modeling and analysis of autothermal reforming of methane to hydrogen in a fixed bed reformer. *Chem Eng J* 2008;137:568-78.

[17] Dega FB, Chamoumi M, Braidy N, Abatzoglou N. Autothermal dry reforming of methane with a nickel spinellized catalyst prepared from a negative value metallurgical residue. *Renewable Energy* 2019;138:1239-49.

[18] Shahhosseini HR, Saeidi S, Najari S, Gallucci F. Comparison of conventional and spherical reactor for the industrial auto-thermal reforming of methane to maximize synthesis gas and minimize CO<sub>2</sub>. *Int J Hydrogen Energy* 2017;42:19798-809.

[19] Akri M, Achak O, Granger P, Wang S, Batiot-Dupeyrat C, Chafik T. Autothermal reforming of model purified biogas using an extruded honeycomb monolith: A new catalyst based on nickel incorporated illite clay promoted with MgO. *J Cleaner Prod* 2018;171:377-89.

[20] Akri M, Chafik T, Granger P, Ayrault P, Batiot-Dupeyrat C. Novel nickel promoted illite clay based catalyst for autothermal dry reforming of methane. *Fuel* 2016;178:139-47.

[21] Nikoo MK, Amin NAS. Thermodynamic analysis of carbon dioxide reforming of

methane in view of solid carbon formation. *Fuel Process Technol* 2011;92:678-91.

[22] Zhu J, Zhang D, King K. Reforming of CH<sub>4</sub> by partial oxidation: thermodynamic and kinetic analyses. *Fuel* 2001;80:899-905.

[23] Carapellucci R, Giordano L. Steam, dry and autothermal methane reforming for hydrogen production: A thermodynamic equilibrium analysis. *J Power Sources* 2020;469.

[24] Wu W, Chen S-A, Hwang J-J, Hsu F-T. Optimization and control of a stand-alone hybrid solid oxide fuel cells/gas turbine system coupled with dry reforming of methane. *Journal of Process Control* 2017;54:90-100.

[25] Fan M-S, Abdullah AZ, Bhatia S. Catalytic Technology for Carbon Dioxide Reforming of Methane to Synthesis Gas. *ChemCatChem* 2009;1:192-208.

[26] Lee B, Lee S, Lim H. Numerical modeling studies for a methane dry reforming in a membrane reactor. *Journal of Natural Gas Science and Engineering* 2016;34:1251-61.

[27] Chen S, Lior N, Xiang W. Coal gasification integration with solid oxide fuel cell and chemical looping combustion for high-efficiency power generation with inherent CO<sub>2</sub> capture. *Appl Energy* 2015;146:298-312.

[28] Nakyai T, Authayanun S, Patcharavorachot Y, Arpornwichanop A, Assabumrungrat S, Saebea D. Exergoeconomics of hydrogen production from biomass air-steam gasification with methane co-feeding. *Energy Convers Manage* 2017;140:228-39.

[29] Zhao Z, Andre Situmorang Y, An P, Yang J, Hao X, Rizkiana J, et al. A biomass-based small-scale power generation system with energy/exergy recuperation. *Energy Convers Manage* 2021;227.

[30] Zhang Y, Zhao Y, Gao X, Li B, Huang J. Energy and exergy analyses of syngas produced from rice husk gasification in an entrained flow reactor. *J Cleaner Prod*

2015;95:273-80.

[31] Yan L, Yue G, He B. Exergy analysis of a coal/biomass co-hydrogasification based chemical looping power generation system. *Energy* 2015;93:1778-87.

[32] Zhang Y, Li B, Li H, Liu H. Thermodynamic evaluation of biomass gasification with air in autothermal gasifiers. *Thermochim Acta* 2011;519:65-71.

[33] Zhang Y, Li B, Li H, Zhang B. Exergy analysis of biomass utilization via steam gasification and partial oxidation. *Thermochim Acta* 2012;538:21-8.

[34] Ojeda K, Sánchez E, El-Halwagi M, Kafarov V. Exergy analysis and process integration of bioethanol production from acid pre-treated biomass: Comparison of SHF, SSF and SSCF pathways. *Chem Eng J* 2011;176-177:195-201.

## CHAPTER 7: Conclusions and Future Perspectives

### 7.1 Conclusions

Carbon-based energies will still be the major section in the world's energy consumption for a long time in the future. High energy efficiency with lower carbon dioxide emissions is the key issue for successful utilization of carbon-based energy. As fully described in **Chapter 1**, gasification technology can bypass the conventional low-rank coals and biomass combustion process and provide a good chance of removing sulfur, nitrogen compounds and particulates. Although the present gasification technology has been mature, the gasifier can still be further improved to achieve higher energy efficiency. According to the difference in reaction time, heat requirement and reaction temperature of each step conversion in gasification as well as the consideration of catalyst deactivation and regeneration, the spatial subdivision of pyrolysis, char gasification, oxidation and tar reforming should be adopted by separated-type multi-stage gasifier to realize a great optimization. The gasification can not only realize a clean utilization of low-rank coals and biomass, but also allow to capture CO<sub>2</sub> from produced syngas to mitigate greenhouse effect. Then, the captured CO<sub>2</sub> mixes with low-cost and abundant CH<sub>4</sub> and is reformed to high value-added products. Due to the limitation of high temperature requirement and rapid catalyst deactivation, the design and development of stable DRM system with high energy efficiency is also very important. Therefore, the studies on achieving advanced and effective gasification system and solving obstacles in DRM process are the main objectives of this dissertation.



Downer is usually used as a fast pyrolyzer, whereas the heavy tar can not be decomposed in downer due to its low solids holdup. To solve this problem, a novel dense downer was proposed and its structural parameters are investigated in **Chapter 3**. The novel dense downer could increase solids holdup extremely. It is found that there is a peak solids holdup in the annular region near the wall whereas many particles concentrate at the center of the dense downer. The unique solids radial distribution is caused by the radial movement of particles. Diameter of dense downer increases solids holdup significantly, but the wall effect is caused when diameter is smaller than 25 mm. Cone structure can push solid particles towards the annular region and inhibits the agglomerates by collisions. However, there is a maximum value of carrying capacity of dense downer which limits the average solids holdup to less than 0.4.

An alternative strategy by applying a separated-type biomass gasification system to a small-scale high-efficient power generation system with energy/exergy recuperation is proposed and simulated in **Chapter 4**. In this system, the fast pyrolysis of biomass combined with the catalytic steam tar reforming is considered to improve gasification performance. It is proved that relatively lower temperature and S/C for the reforming favors more production of syngas with higher energy/exergy. In the optimum case of  $T_{SR} = 850\text{ }^{\circ}\text{C}$  and  $S/C = 2$ , the energy and exergy efficiencies of the total gasification system can reach as high as 79.5% and 64.6%, respectively. Though the integration of energy/exergy recuperation units, 153.44 kW and 136.56 kW of energies or 73.02 kW and 74.36 kW of exergies can be recuperated from gasification system and electricity generation system, respectively. Due to irreversible combustion process, the gasification system contributes the largest exergy destruction, which accounts for almost half of the total exergy loss. As a result, this power generation system could produce an electrical

power output of 263.65 kW and achieve a total energy efficiency of 37.9% or total exergy efficiency of 43.2%, respectively.

**Chapter 5** investigates the hydrodynamics of a small-scale separated-type biomass gasification system by the simulation based on cold model and assesses two kinds of gas seal structures between BFB and riser. In the case of only siphon structure, due to the low solids mass flux, the intended pressure balance between BFB and riser cannot be maintained, causing that air of riser breaks through the moving bed layer and flow into BFB sometimes. The flow behaviors of BFB and riser present a special periodicity. Compared with only siphon structure, the combination of siphon configuration and seal tank shows better gas seal performance. Because of the resistance of configuration of partition and sand particles accumulated at left side of seal tank, the injected air is directed to the riser.

In the last work as described in **Chapter 6**, a novel separated-type ATDRM system with circulating fluidized bed and exergy recuperation is proposed and simulated, in which the DRM combined with POM by circulating fluidized bed is considered. In this ATDRM system, with the increase of temperature in the dry reforming reactor, the conversions of CO<sub>2</sub> and CH<sub>4</sub> increase, while the exergy efficiency decreases significantly. At the condition of relatively lower CO<sub>2</sub>/CH<sub>4</sub> ratio, the high CO<sub>2</sub> conversion and exergy efficiency can be realized easily, but some CH<sub>4</sub> will remain in the products. When operating condition of 950 °C and CO<sub>2</sub>/CH<sub>4</sub> = 1 was set, the novel separated-type ATDRM system can achieve an exergy efficiency of 87.2%. To increase the exergy efficiency, about 1055.7 kW of exergy is recuperated from the crude syngas cooling process and reused for CO<sub>2</sub>, O<sub>2</sub> and CH<sub>4</sub> pre-heating. In this system, the largest exergy destruction occurs in the partial oxidation reactor, which accounts for about

63.1% of the total exergy loss. Compared with the conventional ATDRM system, the exergy of separated-type ATDRM system is slightly lower, however, the CO<sub>2</sub> conversion can be substantially increased about 11.3%.

## 7.2 Future perspectives

Even though the design and development of gasifiers and advanced thermochemical conversion systems in this study have been successfully achieved, further studies are still necessary. Two main future perspectives for optimization and better performance of these gasifiers and systems can be summarized as follows:

- (1) In this study, the flow behavior simulations of gasifiers are implemented under cold state. However, the cold state model does not fit the pyrolysis and reforming equipment perfectly since high temperature can cause the change of physical properties of the gas phase. Therefore, the future work will focus on the modeling of both heat transfer and reaction processes to further evaluate gasifier performance and provide a guidance in the aspects of design and optimization.
- (2) The process simulation in this study mainly focuses on the possibility of novel thermochemical conversion process for higher efficiency. The extended studies will focus on a detail economic analysis to get the further performance evaluation of total system. The economic analysis should include several assumptions and detail surveys on the equipment cost, material selection and cost, and database related to the equipment in the system, and operating cost. Meanwhile, the validation on the economic analysis is also required. In

addition, the cost of treatment of possible pollutants from the gasification of low-rank coals and biomass and dry reforming of methane will be also taken into consideration. Furthermore, how to combine the economic analysis and technical analysis to further optimize system is necessary in the future research.

## LIST of PUBLICATIONS

1. **Zhongkai Zhao**, Yohanes Andre Situmorang, Ping An, Jingxuan Yang, Xiaogang Hao, Jenny Rizkiana, Abuliti Abudula, Guoqing Guan. A biomass-based small-scale power generation system with energy/exergy recuperation. *Energy Conversion and Management*, 227 (2021) 113623.
2. **Zhongkai Zhao**, Yohanes Andre Situmorang, Chihiro Fushimi, Atsushi Tsutsumi, Jingxuan Yang, Xiaogang Hao, Akihiro Yoshida, Abuliti Abudula, Guoqing Guan. Numerical simulation of hydrodynamic behaviors in a gas-solids dense downer reactor. *Advanced Powder Technology*, 31 (7) (2020) 3028-3037.
3. **Zhongkai Zhao**, Yohanes A Situmorang, Ping An, Nichaboon Chaihad, Jing Wang, Xiaogang Hao, Guangwen Xu, Abuliti Abudula, Guoqing Guan. Hydrogen production from catalytic steam reforming of bio-oils: a critical review. *Chemical Engineering & Technology*, 43 (4) (2020) 625-640.
4. Yohanes Andre Situmorang, **Zhongkai Zhao**, Ping An, Jenny Rizkiana, Tirto Prakoso, Abuliti Abudula, Guoqing Guan. A Small-scale Power Generation System Based on Biomass Direct Chemical Looping Process with Organic Rankine Cycle. *Chemical Engineering and Processing: Process Intensification*, in press.
5. Yohanes Andre Situmorang, **Zhongkai Zhao**, Nichaboon Chaihad, Chao Wang, Aisikaer Anniwaer, Yutaka Kasai, Abuliti Abudula, Guoqing Guan. Steam gasification of co-pyrolysis chars from various types of biomass. *International Journal of Hydrogen Energy*, 46 (2021) 3640-3650.
6. Yohanes Andre Situmorang, **Zhongkai Zhao**, Ping An, Tao Yu, Jenny Rizkiana, Abuliti Abudula, Guoqing Guan. A novel system of biomass-based hydrogen

production by combining steam bio-oil reforming and chemical looping process. *Applied Energy*, 268 (2020) 115122.

7. Yohanes Andre Situmorang, **Zhongkai Zhao**, Akihiro Yoshida, Abuliti Abudula, Guoqing Guan. Small-scale biomass gasification systems for power generation (< 200 kW class): A review. *Renewable and Sustainable Energy Reviews*, 117 (2020) 109486.
8. Yohanes Andre Situmorang, **Zhongkai Zhao**, Akihiro Yoshida, Yutaka Kasai, Abuliti Abudula, Guoqing Guan. Potential power generation on a small-scale separated-type biomass gasification system. *Energy*, 179 (2019) 19-29.

### **List of papers presented in conferences**

#### *International Conferences*

1. **Zhongkai Zhao**, Yohanes Andre Situmorang, Ping An, Akihiro Yoshida, Abuliti Abudula, Guoqing Guan. An Exergy-recuperative Biomass-utilized Power Generation System. The 7th Asian Conference on Biomass Science, (*Koriyama City Central Community Center, Koriyama, Japan*), December 10, 2019 (Paper ID: P-10).
2. **Zhongkai Zhao**, Yohanes Andre Situmorang, Chihiro Fushimi, Atsushi Tsutsumi, Xiaogang Hao, Akihiro Yoshida, Abuliti Abudula, Guoqing Guan. Numerical simulation of hydrodynamic behaviours in a novel gas-solids moving bed reactor under a downer. Fluidization XVI (*Guilin Shangri-La Hotel, Guilin, China*), May 26-31, 2019.
3. Yohanes Andre Situmorang, **Zhongkai Zhao**, Nichaboon Chaihad, Aisikaer Anniwaer, Akihiro Yoshida, Yutaka Kasai, Abuliti Abudula, Guoqing Guan. Steam

- Gasification Properties of Bio-Chars Derived from Co-pyrolysis of Rice Straw with Other Biomass. The 7th Asian Conference on Biomass Science, (*Koriyama City Central Community Center, Koriyama, Japan*), December 10, 2019 (Paper ID: OB-1).
4. Aisikaer Anniwaer, Yohanes Andre Situmorang, Nichaboon Chaihad, **Zhongkai Zhao**, Tao Yu, Akihiro Yoshida, Yutaka Kasai, Abuliti Abudula, Guoqing Guan. Co-gasification of rice husk and banana peels for hydrogen-rich gas production. The 7th Asian Conference on Biomass Science, (*Koriyama City Central Community Center, Koriyama, Japan*), December 10, 2019 (Paper ID: P-12).
  5. Guoqing Guan, Wenhao Lian, **Zhongkai Zhao**, Xiaogang Hao, Abuliti Abudula, Chihiro Fushimi<sup>3</sup>, Atsushi Tsutsumi, “High-density solids holdup operations in downers: Theoretical analysis and simulation,” 18th Asian Pacific Confederation of Chemical Engineering Congress (APCChE 2019), (*Sapporo, Hokkaido, Japan*), September 23-27, 2019.

#### *Domestic Conferences*

1. Zhongkai Zhao, Yohanes Andre Situmorang, Jenny Rizkiana, Abuliti Abudula, Tao Yu, Guoqing Guan. A small-scale biomass-based combined heat and power generation system with energy/exergy recuperation. 第16回バイオマス科学会議, (*Online*), January 20-21, 2021. (Paper ID: O-03).
2. Zhongkai Zhao, Yohanes Andre Situmorang, Ping An, Akihiro Yoshida, Abuliti Abudula, Guoqing Guan. An exergy-recuperative system for highly efficient CO<sub>2</sub> conversion by combining methane dry reforming and partial oxidation of methane.

- 第 29 回日本エネルギー学会大会, (富山), August 5-7, 2020. (Paper ID: 2-02).
3. 趙 忠凱, 吉田 暁弘, 阿布 里提, 官 国清. Flow behaviors in a small scale biomass gasifier. 第 15 回バイオマス科学会議, (Koriyama City Central Community Center, Koriyama), December 11-13, 2019. (Paper ID: P-17).
  4. Zhongkai Zhao, Yohanes Andre Situmorang, Ping An, Akihiro Yoshida, Abuliti Abudula, Guoqing Guan. A novel biomass IGFC system with exergy recuperation for high efficiency power generation. 第 56 回石炭科学会議, (ウインクあいち、名古屋), October 28-31, 2019. (Paper ID: 1-2).
  5. 趙 忠凱, 伏見 千尋, 吉田 暁弘, 阿布 里提, 官 国清. CFD simulation of the flow behaviours in a novel gas-solids moving bed under a downer. 化学工学会 第 84 年会, (芝浦工業大学、東京), March 13-15, 2019.
  6. Yohanes Andre Situmorang, **Zhongkai Zhao**, Jenny Rizkiana, Tao Yu, Abuliti Abudula, Guoqing Guan. Co-production of Power and Hydrogen from Biomass by Combining Pyrolysis, Steam Tar Reforming, and Biochar Direct Chemical Looping Process. 第 16 回バイオマス科学会議, (Online), January 20-21, 2021. (Paper ID: O-17)
  7. Yohanes Andre Situmorang, **Zhongkai Zhao**, Ping An, Jenny Rizkiana, Tirta Prakoso, Abuliti Abudula, Guoqing Guan. Acetone Application for Organic Rankine Cycle in a Small-scale Power Generation System by Biomass Direct Chemical Looping Combustion. 化学系学協会東北大会, (八戸), September 26-27, 2020. (Paper ID: PD147).
  8. Yohanes Andre Situmorang, 趙 忠凱, Jenny Rizkiana, 阿布 里提, 官 国清. CO<sub>2</sub>-



- Recycling Biomass Gasification Hydrogen Production System with Water Gas Shift and Membrane CO<sub>2</sub> Captured Method. 化学工学会第 51 回秋季大会, (岩手県), September 24-26, 2020. (Paper ID: PB148).
9. Situmorang Yohanes Andre, 趙忠凱, Yu Tao, 吉田 曉弘, 葛西 裕, 阿布 里提, 官 国清. A process design for hydrogen production by combining tar reforming and a chemical looping process for char conversion. 化学工学会第 85 年会, (*Kansai University Senriyama Campus, Osaka*), March 15-17, 2020. (Paper ID: PA157).
10. Yohanes Andre Situmorang, 趙忠凱, Nichaboon Chaihad, 吉田曉弘, 葛西裕, 阿布里提, 官国清. Effect Addition of Various Biomass Char on Steam Cogasification with Rice Straw. 第 15 回バイオマス科学会議, (*Koriyama City Central Community Center, Koriyama*), December 11-13, 2019. (Paper ID: P-09).
11. Aisikaer Anniwaer, Yohanes Andre Situmorang, 趙忠凱, 于涛, 吉田曉弘, 阿布里提, 官国清. Steam gasification of rice husk in the presence of calcined seashells. 第 15 回バイオマス科学会議, (*Koriyama City Central Community Center, Koriyama*), December 11-13, 2019. (Paper ID: P-10).

#### *Honors and Awards*

1. Excellent Student Award, Hirosaki University, September 2019

# CURRICULUM VITAE

---

## Personal Information

---

Name : Zhongkai Zhao

Nationality : China

---

## Educational Background

---

- **Degree: Ph.D. (Hirosaki University, Japan)**

Major : Safety System Engineering

Period : October 2018-September 2021

- **Degree: Master (Taiyuan University of Technology, China)**

Major : Energy and Power Engineering

Period : September 2015-July 2018

- **Degree: Bachelor (Taiyuan University of Technology, China)**

Major : Process equipment and control engineering

Graduation : September 2011-July 2015

---

## Scholarship

---

- **Doctoral Degree**

China Scholarship Council (CSC) (October 2018-September 2021)

- **Master Degree**

National Scholarship for Master Students (September 2015-July 2018)

First Prize Scholarship of Taiyuan University of Technology (September 2017 and June 2018)

Second Prize Scholarship of Taiyuan University of Technology (June 2016)